J. Fluid Mech. (2018), *vol.* 844, *pp.* 357–402. © Cambridge University Press 2018
doi:10.1017/jfm.2018.184

The inertial orientation dynamics of anisotropic particles in planar linear flows

Navaneeth K. Marath[1] **and Ganesh Subramanian**[1,†]

[1]Engineering Mechanics Unit, Jawaharlal Nehru Centre for Advanced Scientific Research, Jakkur, Bangalore, 560 064, India

(Received 19 April 2017; revised 9 February 2018; accepted 20 February 2018; first published online 4 April 2018)

In the Stokes limit, the trajectories of neutrally buoyant torque-free non-Brownian spheroids in ambient planar linear flows are well known. These flows form a one-parameter family, with the velocity gradient tensor given by $\boldsymbol{\nabla u}^{\infty\dagger} = \dot{\gamma}(\mathbf{1}'_x\mathbf{1}'_y + \lambda\mathbf{1}'_y\mathbf{1}'_x)$. The parameter λ is related to the ratio of the vorticity to the extension (given by $(1-\lambda)/(1+\lambda)$), and ranges from -1 to 1, with $\lambda = 1, 0$ and -1 being planar extensional flow, simple shear flow and solid-body rotation respectively. The unit vectors $\mathbf{1}'_x$ and $\mathbf{1}'_y$ are unit vectors along the flow and gradient axes of the simple shear flow ($\lambda = 0$). The trajectories, as described by a unit vector along the spheroid symmetry axis, are closed orbits for $\lambda < \lambda_{crit}$, where $\lambda_{crit} = \kappa^2(1/\kappa^2)$ for an oblate (a prolate) spheroid of aspect ratio κ. We investigate analytically the orientation dynamics of such a spheroid in the presence of weak inertial effects. The inertial corrections to the angular velocities at $O(Re)$ and $O(St)$, where Re and St are the Reynolds ($Re = \rho_f\dot{\gamma}L^2/\mu$) and Stokes numbers ($St = \rho_p\dot{\gamma}L^2/\mu$) respectively, are derived using a reciprocal theorem formulation. Here, L is the semimajor axis of the spheroid, μ is the viscosity of the suspending fluid, $\dot{\gamma}$ is the shear rate, and ρ_p and ρ_f are the particle and fluid densities respectively. A spheroidal harmonics formalism is then used to evaluate the reciprocal theorem integrals and obtain closed-form expressions for the inertial corrections. The detailed examination of these corrections is restricted to the aforementioned Stokesian closed-orbit regime ($\lambda < \lambda_{crit}$). Here, even weak inertia, for asymptotically long times, of $O(1/(\dot{\gamma}Re))$ or $O(1/(\dot{\gamma}St))$, will affect the leading-order orientation distribution on account of the indeterminate nature of the distribution across orbits in the Stokes limit. For $\lambda < \lambda_{crit}$, inertia results in a drift across the closed orbits in Stokes flow, and this orbital drift is characterized using a multiple time scale analysis. The orbits stabilized by the inertial drift, at $O(Re)$ and $O(St)$, are identified in the λ–κ plane. For the majority of (λ, κ) combinations, the stabilized orbit is either one confined to the plane of symmetry (the flow-gradient plane) of the ambient flow (the tumbling orbit) or one where the spheroid is aligned with the ambient vorticity vector (the spinning orbit). However, for some (λ, κ) combinations, depending on the initial orientation, the orbit stabilized can be either the spinning or the tumbling orbit, since both orbits have non-trivial basins of attraction, separated by a pair of unstable (repelling) limit cycles, on the unit sphere of orientations. A stochastic orientation decorrelation mechanism in the form of rotary Brownian motion, characterized by a Péclet number, Pe_r ($Pe_r = \dot{\gamma}/D_r$, where D_r is the rotary Brownian diffusivity), is included to eliminate the aforementioned dependence on the initial orientation distribution

† Email address for correspondence: sganesh@jncasr.ac.in

https://doi.org/10.1017/jfm.2018.184 Published online by Cambridge University Press

for certain (λ, κ) combinations. The unique steady-state orientation distribution determined by the combined effect of Brownian motion and inertia is obtained by solving a closed-orbit-averaged drift–diffusion equation. The steady-state orientation dynamics of an inertial spheroid in a planar linear flow, in the presence of weak thermal orientation fluctuations, has similarities to the thermodynamic description of a one-component system. Thus, we identify a tumbling–spinning transition in a C–κ–$Re\,Pe_r$ space. Here, C is the orbital coordinate that acts as a label for the closed orbits in the Stokes limit. This transition implies hysteretic orientation dynamics in certain regions in the C–κ–$Re\,Pe_r$ space, although the hysteretic volume shrinks rapidly on either side of simple shear flow. In the hysteretic region, one requires exceedingly large times to achieve the unique steady-state distribution (underlying the thermodynamic interpretation), and for durations relevant to experiments, the system may instead attain an initial-condition-dependent metastable distribution.

Key words: low-Reynolds-number flows, multiphase and particle-laden flows, suspensions

1. Introduction

In this paper, we investigate the effect of inertia on the orientation dynamics of neutrally buoyant spheroids in planar linear flows. A spheroid is the simplest geometry used to model anisotropic particles, and is characterized by its orientation (denoted by a unit vector $\boldsymbol{p}$) and aspect ratio (κ). As the aspect ratio of the spheroid increases from 0 to ∞, its shape changes from a thin disk to a slender fibre, with a sphere corresponding to $\kappa = 1$. Planar linear flows form a one-parameter family characterized by a parameter λ. The transpose of the ambient velocity gradient tensor is given in terms of this parameter as $\boldsymbol{\nabla u}^{\infty\dagger} = \dot{\gamma}(\mathbf{1}'_x\mathbf{1}'_y + \lambda\mathbf{1}'_y\mathbf{1}'_x)$. Here, λ can take any value from -1 to 1, and $\mathbf{1}'_x$ and $\mathbf{1}'_y$ are the unit vectors along the flow and gradient axes of the simple shear flow ($\lambda = 0$). With increasing λ, the streamlines of the planar linear flow transition from being circles for solid-body rotation, to ellipses for elliptic linear flows, to straight lines for simple shear flow, and finally to open hyperbolae for hyperbolic linear flows (Bentley & Leal 1986; Subramanian & Koch 2006*c*). Planar linear flows can be readily realized in experiments, the device used being a four-roll mill, developed originally by Taylor (1934); miniature versions of this device have also been developed in recent years (Hudson *et al.* 2004; Lee *et al.* 2007*a*). They have been extensively used in earlier studies of drop deformation, breakup and coalescence, and for studies of the sensitivity of the coil–stretch transition of large macromolecules to the relative magnitudes of ambient extension and vorticity (Bentley & Leal 1986; Leal 2004; Lee, Shaqfeh & Muller 2007*b*). Further, such flows serve as a useful local approximation for any two-dimensional shearing flow. In this paper, our focus is on the singular effect of weak inertia on the Stokesian trajectory topology established in a planar linear flow by the spheroid orientation vector. Similar effects of inertia on both streamline and pathline topologies have been examined in other disperse multiphase systems, with an emphasis on the role of inertia in determining transport properties at the microscale (Subramanian & Koch 2006*a*,*c*, 2007; Krishnamurthy 2014; Krishnamurthy & Subramanian 2018*a*,*b*).

The orientation dynamics of a non-Brownian spheroid in a planar linear flow is well known in the Stokes limit, that is, when there is no inertia in either the particle or the surrounding fluid. In this limit, the spheroid rotates indefinitely in any of a one-parameter family of closed orbits, when λ is less than a critical value, say λ_{crit},

https://doi.org/10.1017/jfm.2018.184 Published online by Cambridge University Press

that is a function of the aspect ratio; $\lambda_{crit} = 1/\kappa^2(\kappa^2)$ for prolate (oblate) spheroids (Hinch & Leal 1972). The particular orbit in which the spheroid rotates is determined by the initial orientation of the spheroid. The orbits are spherical ellipses, as originally shown by Jeffery (1922), and are eponymously known as Jeffery orbits. When $\lambda > \lambda_{crit}$, the system of open trajectories is organized by a network of six fixed points on the unit sphere. The first effects of fluid and particle inertia at $O(Re)$ and O(St) on the aforementioned Stokesian trajectory topology, particularly in the closed-orbit regime, are analysed in detail in this paper. Here, $Re = \rho_f \dot{\gamma} L^2/\mu$ is the Reynolds number and $St = \rho_p \dot{\gamma} L^2/\mu$ is the Stokes number, where ρ_p and ρ_f are the particle and fluid densities, $\dot{\gamma}$ is the shear rate characterizing the ambient planar linear flow, μ is the fluid viscosity and L is the length of the semimajor axis of the spheroid.

The analysis in this paper falls in the regime $Re, St \ll 1$. Following earlier analytical efforts in this regime for limiting geometries (slender fibres in Subramanian & Koch (2005); near spheres in Subramanian & Koch (2006*b*)), the effect of inertia on the orientation dynamics of an arbitrary aspect ratio spheroid rotating in a simple shear flow was analysed in Einarsson *et al.* (2015) and Dabade, Marath & Subramanian (2016) using different approaches. It turns out that, for a prolate spheroid, the effect of inertia (both particle and fluid) is to stabilize the tumbling orbit, the limiting Jeffery orbit in the flow-gradient plane. For oblate spheroids with $\kappa > 0.14$, inertia stabilizes the spinning orbit, the limiting Jeffery orbit in which the orientation vector is (trivially) aligned with the vorticity vector of the simple shear flow. For oblate spheroids with $\kappa < 0.14$, particle inertia stabilizes the spinning orbit, while fluid inertia stabilizes either the spinning or the tumbling orbit depending on the initial spheroid orientation. The multiple steady states for this range of aspect ratios occur due to the presence of an unstable repeller, which divides the unit hemisphere of orientations into two distinct basins of attraction corresponding to the spinning and the tumbling orbits, as first shown by Einarsson *et al.* (2015) and later by Dabade *et al.* (2016), who independently arrived at the same result using an alternate approach. Dabade *et al.* (2016) also evaluated the viscosity of a dilute suspension of spheroids using the aforementioned orientation distribution. While the steady-state viscosity takes a unique value for all suspensions of spheroids with $\kappa > 0.14$, for suspensions of spheroids with $\kappa < 0.14$, the aforementioned multiple steady states result in a non-unique viscosity. Depending on the initial orientation distribution, the intrinsic viscosity can range from a lower limit of $O(nL^3\kappa)$ for a suspension of tumbling oblate spheroids to $O(nL^3)$ for a suspension of spinning oblate spheroids. To render the viscosity unique, a stochastic orientation decorrelation mechanism in the form of rotary Brownian motion, characterized by the Péclet number, Pe_r ($Pe_r = \dot{\gamma}/D_r$, where D_r is the rotary diffusivity of the spheroid), was considered in Dabade *et al.* (2016). The inclusion of the thermal orientation fluctuations leads to a unique orientation distribution whose form depends on $Re\,Pe_r$, a non-dimensional parameter proportional to the square of the shear rate, and κ (Dabade *et al.* 2016; Marath, Dwivedi & Subramanian 2017). Interestingly, the steady-state distribution is of the Boltzmann form, and lends itself to an elegant thermodynamic interpretation in a C–κ–$Re\,Pe_r$ space. Here, C is the orbital coordinate, which is defined in an orbital coordinate system and forms part of the so-called natural coordinates (C, τ) (τ being the phase along a constant-C orbit) first defined by Leal & Hinch (1971). The distribution transitions between a unimodal and a bimodal one, depending on the parameters C, κ and $Re\,Pe_r$. This transition has similarities to a phase transition, with the small- and large-C minima of the bimodal distribution being identified as the spinning and tumbling 'phases' respectively. For simple shear flow, Marath *et al.* (2017) also identified the envelope

https://doi.org/10.1017/jfm.2018.184 Published online by Cambridge University Press

of the multiphase region, which ends in a critical point similar to the thermodynamic critical point for a single-component system. Depending on the parameters, it was shown that the suspension might take exceedingly large times to settle into the unique steady-state distribution; instead, for finite times, the system might stabilize to a metastable distribution, resulting in a hysteretic behaviour of the shear viscosity. As argued by Marath *et al.* (2017), this hysteresis endows an inertial suspension with a memory that is much larger than the nominal microstructural relaxation times (either inertial or Brownian).

Candelier *et al.* (2015*a*) have investigated the effect of fluid inertia on the orientation dynamics of a nearly spherical axisymmetric particle in a steady general linear flow. The particle angular velocity to $O(Re)$ was derived. However, in the particular case of planar linear flows, a detailed characterization of the orientation dynamics of the particle with changing λ was not carried out. Instead, the authors focused on three particular cases of $\lambda = -1$ (solid-body rotation), 0 (simple shear flow) and 1 (extensional flow). For the first two cases, the authors identified the orbits stabilized by fluid inertia. For extensional flow, the authors concluded that the stabilized orientation is the same as that in the Stokes limit, with inertia only altering the transient approach to this orientation. The authors had originally not included the effect of centrifugal buoyancy while calculating the angular velocity due to fluid inertia, which led to the particle spiralling out towards a tumbling motion in solid-body rotation; this was included in a later erratum (Candelier *et al.* 2015*b*). The $O(Re)$ correction to the angular velocity of a nearly spherical axisymmetric particle in a general time-dependent linear flow (turbulent) was derived by Candelier, Einarsson & Mehlig (2016). The angular velocity of an arbitrary aspect ratio spheroid to $O(St)$, rotating in a steady general linear flow, was derived by Einarsson, Angilella & Mehlig (2014). However, the focus was on understanding the orientation dynamics in simple shear flow alone. As mentioned earlier, the trajectories of the spheroid in the Stokes limit are closed even in planar linear flows other than simple shear – those with $\lambda < \lambda_{crit}$. For all $\lambda < \lambda_{crit}$, there exists a range of aspect ratios for which even weak inertia, acting over sufficiently long times, can significantly alter the trajectory of the spheroid from the Stokesian limit. Therefore, it is important to investigate, in a comprehensive manner, the effect of inertia for all planar linear flows with $\lambda < \lambda_{crit}$.

This paper is organized as follows. In § 2, we derive the inertial correction to the spheroid angular velocity using a generalized reciprocal theorem. To evaluate the reciprocal theorem integrals to $O(Re)$, it will be seen that one only needs the Stokes disturbance velocity field around a torque-free neutrally buoyant spheroid in a planar linear flow, and that around a spheroid rotating in a quiescent ambient. In § 3, we present the expressions for these velocity fields obtained using a spheroidal harmonics formalism. The orbits of the spheroid in the Stokes regime are analysed in detail in § 4. The $O(St)$ and $O(Re)$ angular velocities for the particle and fluid inertia cases are presented in §§ 5 and 6 respectively. In these sections, we introduce an analytical approximation, in terms of an orbital drift, to characterize the inertial orientation dynamics, thereby eliminating the need to numerically integrate the set of ordinary differential equations governing the angular coordinates over all possible initial conditions. The analytical approximation is also used to investigate the inertial orientation dynamics of a neutrally buoyant spheroid in § 7. The formal derivation of the orbital drift approximation using a multiple time scale analysis is presented in § 8, where we also discuss the limitations of this approximation for extreme aspect ratio spheroids. The inertial orbital drift alone cannot set up a unique steady-state distribution for (λ, κ) combinations where both tumbling and

https://doi.org/10.1017/jfm.2018.184 Published online by Cambridge University Press

spinning orbits are stabilized. For these combinations, we investigate the combined effect of rotary Brownian motion and inertia, in setting up a unique steady-state distribution, in § 9. Similarly to the case of simple shear flow analysed by Marath *et al.* (2017), the steady-state orientation dynamics in the presence of Brownian motion has similarities to a thermodynamic phase transition, and this interpretation, leading to what we term the 'tumbling–spinning' transition, is developed in the same section; the tumbling–spinning envelope is found to have the maximal extent for simple shear. Finally, we summarize our results in § 10.

2. Formulation for the inertial drift: the generalized reciprocal theorem

The velocity and stress fields in two different problems, the problem of interest and a test problem, corresponding to two different flow configurations past the same particle, can be related through a generalized reciprocal theorem (Leal 1979; Subramanian & Koch 2005, 2006*b*; Einarsson *et al.* 2015; Dabade *et al.* 2016). The two problems are defined based on a dynamical quantity that needs to be evaluated for the problem of interest. The test problem is usually chosen to be one in which the velocity and stress fields are known *a priori*. In the present case, the quantity of interest is the correction to the angular velocity of a neutrally buoyant spheroid suspended in a Newtonian fluid undergoing a planar linear flow, with the inertial acceleration, both that of the particle and that of the fluid, being taken into account. The disturbance velocity and stress fields in the aforementioned problem of interest are denoted by $\boldsymbol{u}'^{(1)}$ and $\boldsymbol{\sigma}'^{(1)}$. The disturbance fields are related to the total velocity and stress fields in the problem by $\boldsymbol{u}'^{(1)} = \boldsymbol{u}^{(1)} - \boldsymbol{\Gamma}\cdot\boldsymbol{x}$ and $\boldsymbol{\sigma}'^{(1)} = \boldsymbol{\sigma}^{(1)} - \boldsymbol{\sigma}^{(\infty)} = \boldsymbol{\sigma}^{(1)} + p^{\infty}\boldsymbol{I} - 2\boldsymbol{E}$. Here, $\boldsymbol{\Gamma}\cdot\boldsymbol{x}$ is the ambient planar linear flow in non-dimensional form defined with the origin at the centre of the spheroid. The transpose of the non-dimensional (ambient) velocity gradient tensor and the rate-of-strain tensor, in a space-fixed coordinate system ($X'Y'Z'$, with the unit vector triplet $\mathbf{1}'_x$, $\mathbf{1}'_y$ and $\mathbf{1}'_z$), are given by $\boldsymbol{\Gamma} = \mathbf{1}'_x\mathbf{1}'_y + \lambda\mathbf{1}'_y\mathbf{1}'_x$ and $\boldsymbol{E} = (\mathbf{1}'_x\mathbf{1}'_y + \mathbf{1}'_y\mathbf{1}'_x)(\lambda+1)/2$ respectively. As mentioned earlier, the parameter λ characterizes the family of planar linear flows, with $(1-\lambda)/(1+\lambda)$ denoting the rate of vorticity to extension in the flow. The ambient streamline patterns for these flows are shown in figure 1. As λ increases from -1 to 1, there is a transition from a closed (figure 1*a*,*b*) to an open streamline pattern (figure 1*d*,*e*), with the streamlines for $\lambda = 0$ alone (figure 1*c*) being straight lines. The axes of the space-fixed coordinate system, X', Y' and Z', are defined such that they coincide with the flow, the gradient and the vorticity directions of the simple shear flow ($\lambda = 0$) respectively (figure 1*f*). The ambient pressure (p^{∞}) required to maintain the linear flow for finite Re is obtained by equating its gradient to the inertial acceleration, whence one finds $p^{\infty} = -Re\,\boldsymbol{x}\cdot\boldsymbol{\Gamma}\cdot\boldsymbol{\Gamma}\cdot\boldsymbol{x}/2$. It should be noted that $p^{\infty} = 0$ for simple shear flow.

The test problem, with its velocity and stress fields denoted by $\boldsymbol{u}^{(2)}$ and $\boldsymbol{\sigma}^{(2)}$ respectively, corresponds to the Stokesian rotation of a spheroid in an otherwise quiescent ambient, with the same instantaneous orientation as that in the problem of interest. We also define two second-order tensors $\boldsymbol{L}_2$, $\boldsymbol{U}^{(2)}$ and a third-order tensor $\boldsymbol{\Sigma}^{(2)}$, which relate $\boldsymbol{\mathcal{L}}_2$ (the torque acting on the spheroid in the test problem), $\boldsymbol{u}^{(2)}$ and $\boldsymbol{\sigma}^{(2)}$ respectively to $\boldsymbol{\Omega}_2$ (the angular velocity in the test problem), the relations being given by $\boldsymbol{\mathcal{L}}_2 = \boldsymbol{L}_2\cdot\boldsymbol{\Omega}_2$, $\boldsymbol{u}^{(2)} = \boldsymbol{U}^{(2)}\cdot\boldsymbol{\Omega}_2$ and $\boldsymbol{\sigma}^{(2)} = \boldsymbol{\Sigma}^{(2)}\cdot\boldsymbol{\Omega}_2$. The expressions for these tensors are given in §§ 3 and 4 (alternatively, see Dabade *et al.* 2016).

The derivation of the reciprocal theorem, which gives the inertial correction to the angular velocity in the problem of interest ($\boldsymbol{\Omega}_1$), is similar to that for a spheroid in a Newtonian fluid undergoing simple shear flow given in § 2 of Dabade *et al.* (2016),

https://doi.org/10.1017/jfm.2018.184 Published online by Cambridge University Press

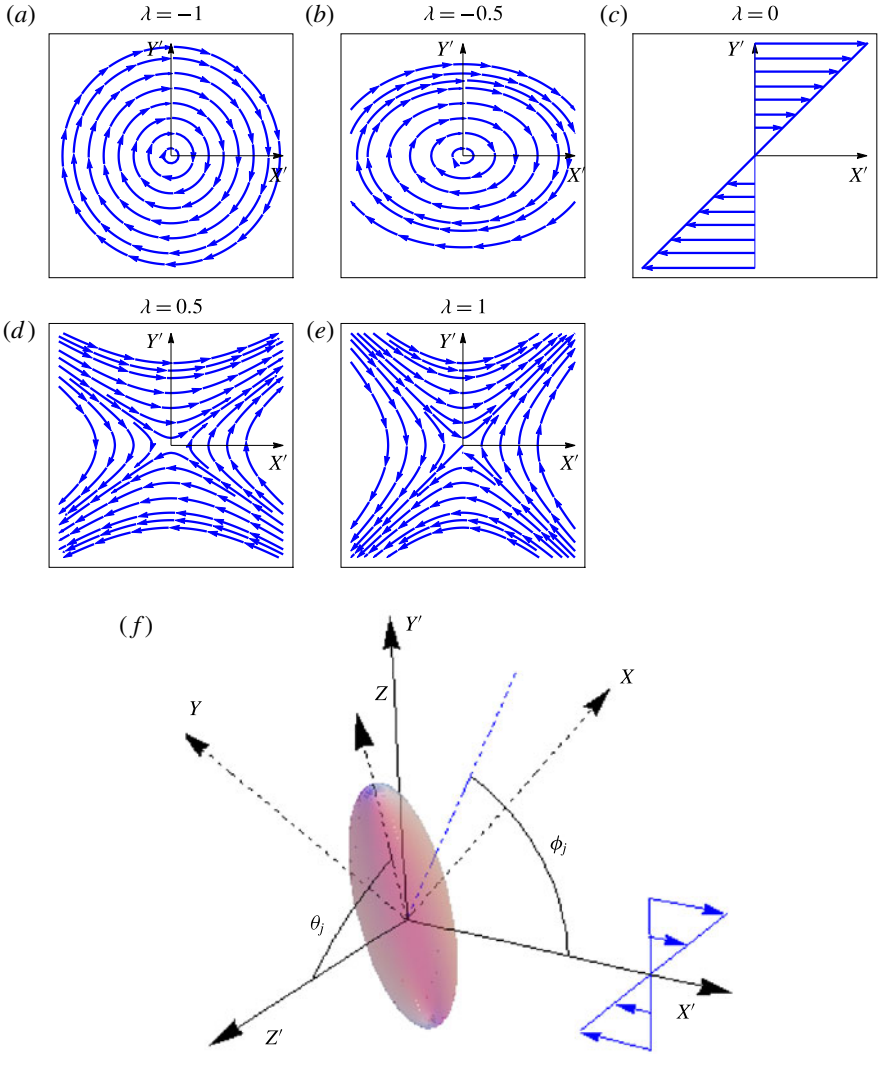


FIGURE 1. (Colour online) The ambient streamline patterns in the spaced-fixed coordinate system for (*a*) solid-body rotation, (*b*) elliptic linear flow, (*c*) simple shear flow, (*d*) hyperbolic linear flow and (*e*) planar extensional flow. In (*f*), the body-aligned and space-fixed coordinate systems are shown for a spheroid in simple shear flow.

except for an additional contribution that comes from the ambient pressure field. Here, we only present the final result and the reader is referred to Dabade *et al.* (2016) for the details,

$$\boldsymbol{\Omega}_1 \cdot \boldsymbol{L}_2 = \boldsymbol{\Gamma} : \int_{S_p} \boldsymbol{x}(\boldsymbol{\Sigma}^{(2)} \cdot \boldsymbol{n})\,\mathrm{d}S + St\,\frac{\mathrm{d}}{\mathrm{d}t}(\boldsymbol{I}_p \cdot \boldsymbol{\Omega}_1) + Re \int_V \left[\frac{\partial \boldsymbol{u}'^{(1)}}{\partial t} + (\boldsymbol{\Gamma} \cdot \boldsymbol{x}) \cdot \nabla \boldsymbol{u}'^{(1)} + \boldsymbol{\Gamma} \cdot \boldsymbol{u}'^{(1)} + \boldsymbol{u}'^{(1)} \cdot \nabla \boldsymbol{u}'^{(1)} + \boldsymbol{\Omega}_b \wedge \boldsymbol{u}'^{(1)} - (\boldsymbol{\Omega}_b \wedge \boldsymbol{x}).\nabla \boldsymbol{u}'^{(1)}\right] \cdot \boldsymbol{U}^{(2)}\,\mathrm{d}V - Re \int_{S_p} \frac{\boldsymbol{x} \cdot \boldsymbol{\Gamma} \cdot \boldsymbol{\Gamma} \cdot \boldsymbol{x}}{2}(\boldsymbol{x} \wedge \boldsymbol{n})\,\mathrm{d}A. \tag{2.1}$$

https://doi.org/10.1017/jfm.2018.184 Published online by Cambridge University Press

The reciprocal theorem above may also be seen in Candelier *et al.* (2015*a*). The authors did not evaluate the ambient pressure contribution correctly, which was rectified in a later communication (Candelier *et al.* 2015*b*). The surface integrals in (2.1) are over the spheroid (S_p) and the volume integral is over the unbounded fluid outside the spheroid (V). In (2.1), $\boldsymbol{I}_p$ is the moment of inertia tensor of the spheroid, given by $(4\pi/15)\bar{\xi}_0^2[(2\bar{\xi}_0^2/\xi_0^4)\boldsymbol{pp} + ((2\xi_0^2-1)/\xi_0^4)(\boldsymbol{I}-\boldsymbol{pp})]$ and $(4\pi/15)\bar{\xi}_0[(2/\xi_0)\boldsymbol{pp} + ((2\xi_0^2-1)/\xi_0^3)(\boldsymbol{I}-\boldsymbol{pp})]$ for prolate and oblate spheroids respectively. Here, $\boldsymbol{p}$ is the spheroid orientation vector and ξ_0 is the inverse of the spheroid eccentricity.

As shown by Dabade *et al.* (2016) and later in § 3, the disturbance velocity field around a spheroid in Stokes flow is expressed in a body-aligned spheroidal coordinate system. Therefore, while deriving (2.1), we transformed the reciprocal theorem from the original space-fixed coordinate system ($X'Y'Z'$ in figure 1*f*) to a body-aligned coordinate system (XYZ in figure 1*f*; see Dabade *et al.* 2016). The angles θ_j and ϕ_j determine the orientation of the spheroid (the Z axis) with respect to the space-fixed coordinate system. To simplify the calculation, we restrict the Y axis of the body-aligned coordinate system to the flow-gradient plane. This restriction makes the angular velocity of the body-aligned coordinate system, denoted by $\boldsymbol{\Omega}_b$ in (2.1), different from $\boldsymbol{\Omega}_1$. The unit vectors of the body-aligned coordinate system XYZ can be expressed in terms of those of the space-fixed coordinate system $X'Y'Z'$ (see figure 1) as $\mathbf{1}_x = \cos\theta_j\cos\phi_j\mathbf{1}'_x + \cos\theta_j\sin\phi_j\mathbf{1}'_y - \sin\theta_j\mathbf{1}'_z$, $\mathbf{1}_y = -\sin\phi_j\mathbf{1}'_x + \cos\phi_j\mathbf{1}'_y$ and $\mathbf{1}_z = \sin\theta_j\cos\phi_j\mathbf{1}'_x + \sin\theta_j\sin\phi_j\mathbf{1}'_y + \cos\theta_j\mathbf{1}'_z$.

Although (2.1) is valid for arbitrary Re, it is only of limited use in this general form because $\boldsymbol{u}'^{(1)}$ is not known for finite Re. We therefore analyse (2.1) in the limit of Re being small but finite, and determine $\boldsymbol{\Omega}_1$ to $O(Re)$. The leading-order angular velocity ($\boldsymbol{\Omega}_{jeff}$) corresponding to the Stokes regime can be obtained by equating the left-hand side of (2.1) to the first term on its right-hand side. The subscript '*jeff*' is used for the leading-order angular velocity since $\boldsymbol{\Omega}_{jeff}$ leads to closed orbits for a certain subset of planar linear flows (those with vorticity above an aspect-ratio-dependent threshold), which are identified in § 4. These are again spherical ellipses, as in simple shear, and are also termed as Jeffery orbits. The leading-order angular velocity is defined in the body-aligned coordinate system in terms of $\dot{\phi}_j$ and $\dot{\theta}_j$ as $\boldsymbol{\Omega}_{jeff} = -\dot{\phi}_j\sin\theta_j\,\mathbf{1}_x + \dot{\theta}_j\,\mathbf{1}_y - \cos\theta_j(1-\lambda)/2\,\mathbf{1}_z$, where $\dot{\phi}_j$ and $\dot{\theta}_j$ are given by (Hinch & Leal 1972)

$$\dot{\phi}_j = -\left(\frac{1-\lambda}{2}\right) + \left(\frac{1+\lambda}{2}\right)\frac{\kappa^2-1}{\kappa^2+1}\cos 2\phi_j, \tag{2.2}$$

$$\dot{\theta}_j = \left(\frac{1+\lambda}{4}\right)\frac{\kappa^2-1}{\kappa^2+1}\sin 2\theta_j\sin 2\phi_j, \tag{2.3}$$

with b as the minor axis of the spheroid, $\kappa = L/b$ (b/L) for a prolate (an oblate) spheroid. The inertial contributions to $\boldsymbol{\Omega}_1$ in (2.1) include that due to the particle (the term proportional to St) and the fluid inertial contributions (the terms proportional to Re) on the right-hand side of (2.1). The last term proportional to Re is due to the non-trivial ambient pressure field and may be interpreted as a centrifugal buoyancy. For simple shear flow, this contribution is zero, and (2.1) reduces to (2.21) in Dabade *et al.* (2016).

The $O(Re)$ and $O(St)$ corrections to the angular velocity can be obtained by replacing $\boldsymbol{u}'^{(1)}$ with $\boldsymbol{u}'^{(1)}_s$, the Stokes disturbance velocity field for a spheroid in a planar linear flow, $\boldsymbol{\Omega}_1$ with $\boldsymbol{\Omega}_{jeff}$ in the term proportional to St, and $\boldsymbol{\Omega}_b$ with $\boldsymbol{\Omega}^t_{jeff}$ on the right-hand side of (2.1). The leading-order angular velocity of the body-aligned coordinate system, $\boldsymbol{\Omega}^t_{jeff}$, differs from $\boldsymbol{\Omega}_{jeff}$ in the spin component, due

https://doi.org/10.1017/jfm.2018.184 Published online by Cambridge University Press

to the restriction on the Y axis of the body-aligned coordinate system discussed above; $\boldsymbol{\Omega}^t_{jeff} = -\dot{\phi}_j \sin\theta_j \mathbf{1}_x + \dot{\theta}_j \mathbf{1}_y + \dot{\phi}_j \cos\theta_j \mathbf{1}_z$. Thus, to $O(Re)$, (2.1) becomes

$$\begin{aligned}\boldsymbol{\Omega}_1 \cdot \boldsymbol{L}_2 \;=\; & \boldsymbol{\Gamma} : \int_{S_p} \boldsymbol{x}(\boldsymbol{\Sigma}^{(2)} \cdot \boldsymbol{n})\,\mathrm{d}S + St\frac{\mathrm{d}}{\mathrm{d}t}(\boldsymbol{I}_p \cdot \boldsymbol{\Omega}_1) + Re\int_V \left[\frac{\partial \boldsymbol{u}_s'^{(1)}}{\partial t} + (\boldsymbol{\Gamma}\cdot\boldsymbol{x})\cdot\nabla\boldsymbol{u}_s'^{(1)}\right. \\ & \left. + \boldsymbol{\Gamma}\cdot\boldsymbol{u}_s'^{(1)} + \boldsymbol{u}_s'^{(1)}\cdot\nabla\boldsymbol{u}_s'^{(1)} + \boldsymbol{\Omega}^t_{jeff}\wedge\boldsymbol{u}_s'^{(1)} - (\boldsymbol{\Omega}^t_{jeff}\wedge\boldsymbol{x})\cdot\nabla\boldsymbol{u}_s'^{(1)}\right]\cdot\boldsymbol{U}^{(2)}\,\mathrm{d}V \\ & - Re\int_{S_p}\frac{\boldsymbol{x}\cdot\boldsymbol{\Gamma}\cdot\boldsymbol{\Gamma}\cdot\boldsymbol{x}}{2}(\boldsymbol{x}\wedge\boldsymbol{n})\,\mathrm{d}A. \end{aligned} \tag{2.4}$$

The volume integral with $\boldsymbol{u}_s'^{(1)}$ above is a convergent one, which points to the regular nature of the $O(Re)$ correction. The convergence can be seen by noting that $\boldsymbol{u}_s'^{(1)}$ and $\boldsymbol{U}^{(2)}$ decay as $1/r^2$, where r is the distance from the centre of the spheroid; the integrand therefore decays as $1/r^4$ at large distances, making the integral convergent. In turn, this implies that the fluid inertial forces that contribute to the $O(Re)$ torque arise in a volume of $O(L^3)$ around the spheroid. The corrections to the Stokes velocity field when substituted in (2.1) will only lead to higher-order corrections in the angular velocity starting at $O(Re^2)$. The dominant correction at the next order in fact arises at $O(Re^{3/2})$ and requires an analysis of the outer region with inertial forces accounted for at leading order. The correction modifies the time period of rotation at $O(Re^{3/2})$ (Marath & Subramanian 2017). The Stokes velocity fields $\boldsymbol{u}_s'^{(1)}$ and $\boldsymbol{u}^{(2)}$ needed to evaluate (2.4) are given in § 3.

3. Solution to the Stokes equations in spheroidal coordinates

The reciprocal theorem formulation in its final form, (2.4), requires the Stokes disturbance velocity field ($\boldsymbol{u}_s'^{(1)}$) due to a torque-free spheroidal particle in a planar linear flow and that due to a rotating spheroid in a quiescent fluid ($\boldsymbol{u}^{(2)}$). The integral in the reciprocal theorem is evaluated in a body-aligned coordinate system (XYZ). The transpose of the ambient velocity gradient tensor, $\boldsymbol{\Gamma}$, when expressed in this system, becomes

$$\begin{aligned}\boldsymbol{\Gamma} \;=\; & (1+\lambda)\cos^2\theta_j \sin\phi_j\cos\phi_j \mathbf{1}_x\mathbf{1}_x + \cos\theta_j(\cos^2\phi_j - \lambda\sin^2\phi_j)\mathbf{1}_x\mathbf{1}_y \\ & + (1+\lambda)\sin\theta_j\cos\theta_j\sin\phi_j\cos\phi_j(\mathbf{1}_x\mathbf{1}_z + \mathbf{1}_z\mathbf{1}_x) + \cos\theta_j(\lambda\cos^2\phi_j - \sin^2\phi_j)\mathbf{1}_y\mathbf{1}_x \\ & - (1+\lambda)\cos\phi_j\sin\phi_j\mathbf{1}_y\mathbf{1}_y + \sin\theta_j(\lambda\cos^2\phi_j - \sin^2\phi_j)\mathbf{1}_y\mathbf{1}_z \\ & + \sin\theta_j(\cos^2\phi_j - \lambda\sin^2\phi_j)\mathbf{1}_z\mathbf{1}_y + (1+\lambda)\sin^2\theta_j\sin\phi_j\cos\phi_j\mathbf{1}_z\mathbf{1}_z. \end{aligned} \tag{3.1}$$

The velocity gradient tensor can be split into a rate-of-strain tensor and an ambient vorticity tensor. In the Stokes limit, a torque-free spheroid does not generate a disturbance velocity field in response to the ambient vorticity. The rate-of-strain tensor $\boldsymbol{E}$ may be written as

$$\begin{aligned}\boldsymbol{E} \;=\; & (1+\lambda)\left(\cos^2\theta_j\sin\phi_j\cos\phi_j\mathbf{1}_x\mathbf{1}_x + \tfrac{1}{2}\cos\theta_j(\cos^2\phi_j - \sin^2\phi_j)(\mathbf{1}_x\mathbf{1}_y + \mathbf{1}_y\mathbf{1}_x)\right. \\ & + \sin\theta_j\cos\theta_j\sin\phi_j\cos\phi_j(\mathbf{1}_x\mathbf{1}_z + \mathbf{1}_z\mathbf{1}_x) - \cos\phi_j\sin\phi_j\mathbf{1}_y\mathbf{1}_y \\ & \left. + \tfrac{1}{2}\sin\theta_j(\cos^2\phi_j - \sin^2\phi_j)\,(\mathbf{1}_y\mathbf{1}_z + \mathbf{1}_z\mathbf{1}_y) + \sin^2\theta_j\sin\phi_j\cos\phi_j\mathbf{1}_z\mathbf{1}_z\right) \end{aligned} \tag{3.2}$$

in the body-aligned coordinate system. It should be noted that $\boldsymbol{E}$ for a planar linear flow is simply $(1+\lambda)$ times $\boldsymbol{E}$ for simple shear flow ($\lambda = 0$) (see (3.2) in Dabade *et al.* 2016). Following Dabade *et al.* (2016), the rate-of-strain tensor is split into five canonical component linear flows in the body-aligned coordinate system, with the amplitude of each of these merely being $(1+\lambda)$ times that in simple shear flow.

https://doi.org/10.1017/jfm.2018.184 Published online by Cambridge University Press

The five components include an axisymmetric extensional flow, a pair of extensional flows in the plane transverse to the symmetry axis (XY plane), with one obtained from the other via a $\pi/4$ rotation of the principal axis, and a pair of extensional flows in the two orthogonal planes containing the axis of symmetry (XZ and YZ planes) and with the extensional axis at an angle of $\pi/4$ to the axis of symmetry. The corresponding Stokesian disturbance fields are denoted as $\boldsymbol{u}_{1s}$–$\boldsymbol{u}_{5s}$, with $\boldsymbol{u}_{1s}$ corresponding to the axisymmetric extension, $\boldsymbol{u}_{2s}$ and $\boldsymbol{u}_{3s}$ corresponding to the two transverse planar extensions and $\boldsymbol{u}_{4s}$ and $\boldsymbol{u}_{5s}$ corresponding to the pair of longitudinal extensions. The Stokes disturbance velocity field in a planar linear flow is then given by $\boldsymbol{u}_s'^{(1)} = \sum_{i=1}^{5} \boldsymbol{u}_{is}$. Here,

$$\boldsymbol{u}_{is}(\lambda) = (1+\lambda)\boldsymbol{u}_{is}(0) \quad (i = 1\text{–}5), \tag{3.3}$$

where $\boldsymbol{u}_{is}(0)$ is the disturbance velocity field for a spheroid of the same orientation in an ambient simple shear. The expressions for $\boldsymbol{u}_{is}(0)$ are given in equations (3.17), (3.19), (3.21), (3.23) and (3.25) of Dabade *et al.* (2016). The disturbance velocity fields for the test problem were also derived in Dabade *et al.* (2016). The fields $\boldsymbol{u}_{sx}^{(2)}$, $\boldsymbol{u}_{sy}^{(2)}$ and $\boldsymbol{u}_{sz}^{(2)}$, corresponding to the rotations about the X, Y and Z axes respectively, are given in equations (3.28), (3.30) and (3.36) of Dabade *et al.* (2016). These velocity fields are reproduced in appendix A.

Knowledge of the Stokesian velocity fields in both the test problem and the problem of interest allows one to evaluate the integral in (2.4) to $O(Re)$. While the velocity field $\boldsymbol{u}_s'^{(1)}$ appears directly, the test velocity field enters (2.4) via the tensors $\boldsymbol{L}_2$, $\boldsymbol{U}^{(2)}$ and $\boldsymbol{\Sigma}^{(2)}$ introduced earlier. The second-order tensors in (2.4) are given by $\boldsymbol{U}^{(2)} = \boldsymbol{u}_{sx}^{(2)}\mathbf{1}_x + \boldsymbol{u}_{sy}^{(2)}\mathbf{1}_y + \boldsymbol{u}_{sz}^{(2)}\mathbf{1}_z$ and $\boldsymbol{L}_2 = -8\pi(X_C\boldsymbol{pp} + Y_C(\boldsymbol{I} - \boldsymbol{pp}))$, with $\boldsymbol{p} = \mathbf{1}_z$. The constants $8\pi X_C$ and $8\pi Y_C$ are the torque magnitudes corresponding to axial and transverse rotations respectively, with unit angular velocity, with $X_C = 4(\xi_0^2 - 1)/(3\xi_0^3(2\xi_0 - 2(\xi_0^2 - 1)\coth^{-1}\xi_0))$ and $Y_C = 4(2\xi_0^2 - 1)/(3\xi_0^3(2(\xi_0^2 + 1)\coth^{-1}\xi_0 - 2\xi_0))$ (Kim & Karrila 1991). The expression for $\boldsymbol{\Sigma}^{(2)}$ is given in (4.2) of Dabade *et al.* (2016).

4. The Stokes limit and the equivalent aspect ratio

In this section, we summarize the results from earlier efforts (Prager 1957; Bretherton 1962; Hinch & Leal 1972) that analyse the trajectories traced by the spheroid orientation vector on the unit sphere in an ambient planar linear flow in the Stokes limit. The rates of change of θ_j and ϕ_j in this limit are given in (2.2) and (2.3), which can be recovered from (2.4) by evaluating the surface integral that remains in the limit of $Re = St = 0$ and noting that $\boldsymbol{\Sigma}^{(2)} \cdot \mathbf{1}_\xi = -\boldsymbol{P}^{(2)}\mathbf{1}_\xi + 2\left[(\bar{\xi}/d(\xi^2 - \eta^2)^{1/2})(\partial/\partial\xi)\boldsymbol{U}^{(2)} + (1/2)\mathbf{1}_\xi \wedge (\boldsymbol{\nabla} \wedge \boldsymbol{U}^{(2)})\right]$, where $\boldsymbol{P}^{(2)}$ is the pressure field vector corresponding to the transverse rotations given by Dabade *et al.* (2016). For a given aspect ratio, the trajectories are closed orbits until $\lambda = \lambda_{crit}$ (Hinch & Leal 1972). This is expected because the vortical component of the flow responsible for the existence of closed orbits decreases with increasing λ (figure 1*a–e*). At $\lambda = \lambda_{crit}$, it becomes sufficiently small compared with the extensional component for closed orbits to cease to exist. One finds $\lambda_{crit} = 1/\kappa^2$ and κ^2 respectively for prolate and oblate spheroids of aspect ratio κ. Since λ_{crit} is always positive, the critical flow separating open and closed trajectories on the unit sphere is always a hyperbolic linear flow. It should be noted that $\lambda_{crit} \to 0$ for infinitely thin fibres and disks, implying that the critical flow asymptotes to a simple shear for extreme aspect ratios, consistent with the fact that the orientations of an infinitely slender fibre and the normal to a flat disk evolve in an affine manner, merely following the ambient streamlines (projected onto the unit sphere) in these limits.

https://doi.org/10.1017/jfm.2018.184 Published online by Cambridge University Press

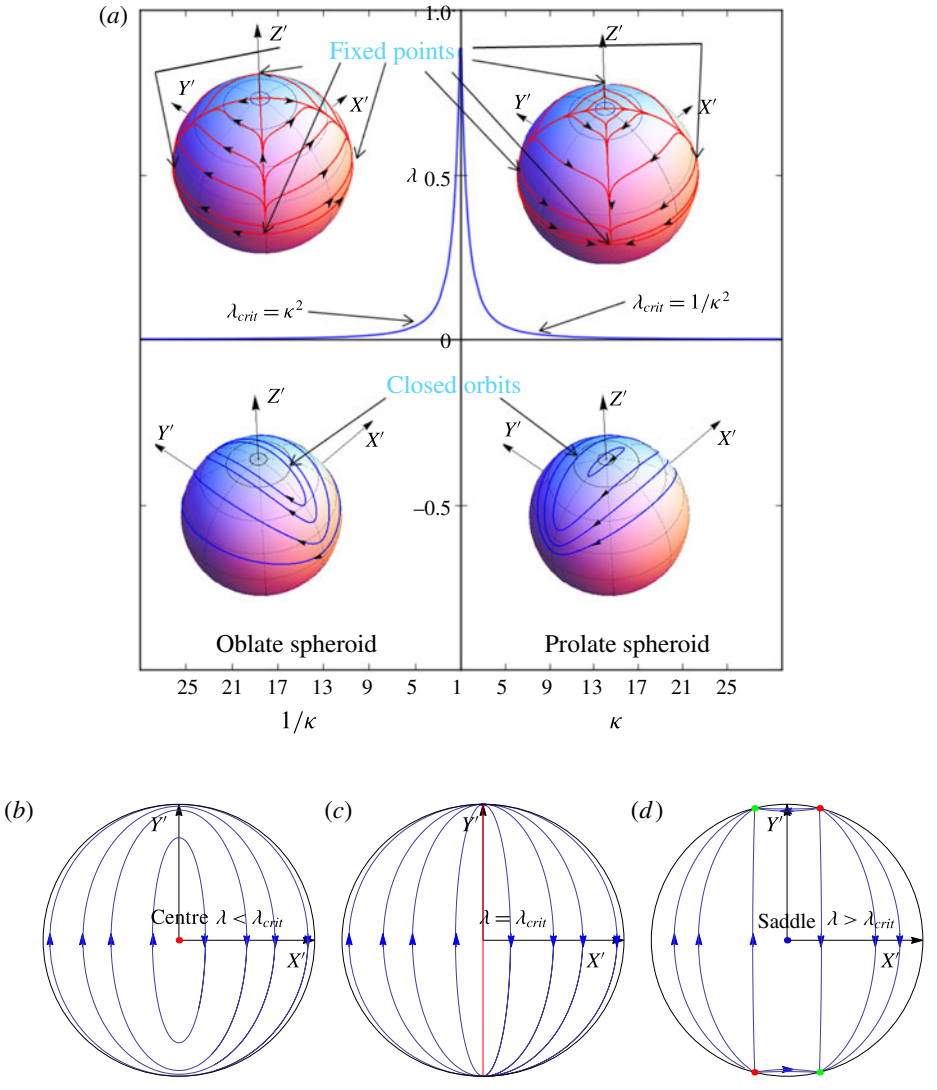


FIGURE 2. (Colour online) (*a*) The λ_{crit} curve in the λ–κ plane. The blue curve corresponds to the critical λ curve which separates the open- and closed-trajectory topologies at $Re = 0$. Typical trajectory topologies, obtained from the trace of the orientation vector on a unit sphere centred at the origin starting from various initial conditions, are shown in the inset plots as blue (closed) and red (open and moving towards a stable fixed point) curves for regions above and below the λ_{crit} curve. (*b–d*) The transition of the intersection of the vorticity axis and the unit hemisphere from a centre below $\lambda < \lambda_{crit}$ to a saddle above $\lambda > \lambda_{crit}$, as viewed from the vorticity axis, for an oblate spheroid. At $\lambda = \lambda_{crit}$, there is a degenerate great circle of fixed points (shown in red). For $\lambda > \lambda_{crit}$, there are four additional fixed points (two stable and two unstable) on the flow-gradient plane.

In figure 2(*a*), λ_{crit} is plotted as a function of κ. The trajectories for the spheroid orientation are closed below the λ_{crit} curve, with the minimal orbits corresponding to

https://doi.org/10.1017/jfm.2018.184 Published online by Cambridge University Press

a pair of centres (the points of intersection of the ambient vorticity axis with the unit sphere). There are six fixed points on the unit sphere for $\lambda > \lambda_{crit}$; pairs of unstable and stable nodes in the flow-gradient plane, and the pair of centres transforming to saddle points (the indices of these fixed points add to the Euler characteristic of 2, as must be the case). Except for trajectories connecting the saddle points and unstable nodes, all remaining trajectories end in the two stable nodes. At $\lambda = \lambda_{crit}$, a degenerate situation exists in which there is an entire curve of fixed points. The open- and closed-trajectory topologies on either side of the λ_{crit} curve, for both prolate and oblate spheroids, are shown in the relevant regions of figure 2(*a*). The aforementioned transition from a pair of centres to the six fixed points on the unit sphere is illustrated for an oblate spheroid in figure 2(*b*). As will be shown in later sections, in the region below the λ_{crit} curve in figure 2(*a*), weak inertia will result in a slow drift across the closed orbits, and the long-time orientation dynamics can be drastically different from the degenerate scenario implied by Stokesian dynamics, which predicts a continued dependence on the initial orientation. In the region above the λ_{crit} curve, weak inertia can only alter the location of the stable fixed points (corresponding to the localization of the orientation distribution for long times) by $O(Re)$ or $O(St)$. Therefore, this region in the λ–κ plane is not analysed in detail. It should be noted, however, that the corrections to the angular velocities at $O(Re)$ and $O(St)$ presented in the next two sections are valid over the entire λ–κ plane.

It has been shown that in the Stokes limit, the orbits of the spheroid orientation vector in a planar linear flow ($\lambda < \lambda_{crit}$) are the same as those of an equivalent spheroid in a simple shear flow of strength $(1 - \lambda)$ (Prager 1957; Bretherton 1962; Hinch & Leal 1972). The aspect ratio of this latter spheroid is a function of λ and κ, and is given by

$$\kappa_{eq} = \sqrt{\frac{(\kappa^2+1)(1-\lambda)+(\kappa^2-1)(1+\lambda)}{(\kappa^2+1)(1-\lambda)-(\kappa^2-1)(1+\lambda)}}. \tag{4.1}$$

For simple shear flow ($\lambda = 0$), κ_{eq} is, of course, the same as κ. From (4.1), κ_{eq} varies from 1 to $\infty(0)$ for prolate (oblate) as λ increases from -1 to λ_{crit}. The closed trajectories in a planar linear flow are again Jeffery orbits but of the aforementioned equivalent spheroid. This would also mean that spheroids of different aspect ratios can have the same trajectories for different flows. In particular, for $\lambda \to \lambda_{crit}$, a spheroid of an arbitrary aspect ratio rotates in nearly meridional trajectories similarly to a slender fibre (for prolate) or a flat disk (for oblate) in simple shear flow.

In the following sections, we interpret the weak inertial effects in terms of a drift across Stokesian trajectories in a non-orthogonal orbital coordinate system (Leal & Hinch 1971). The orbital coordinates (C, τ) are defined such that the constant-C lines coincide with the Jeffery orbits of the planar linear flow for the spheroid under consideration, while the constant-τ lines are the same as the constant-ϕ_j contours (on the unit sphere). The orbital coordinates are related to θ_j and ϕ_j in terms of the equivalent aspect ratio κ_{eq},

$$C = \tan\theta_j \frac{\sqrt{(\kappa_{eq}^2 \sin^2\phi_j + \cos^2\phi_j)}}{\kappa_{eq}}, \tag{4.2}$$

$$\tau = \tan^{-1}\left(\frac{1}{\kappa_{eq}\tan\phi_j}\right). \tag{4.3}$$

Here, C varies from 0 to ∞, with $C = 0$ and $C = \infty$ being the spinning and tumbling orbits respectively, with the finite-C orbits corresponding to three-dimensional

https://doi.org/10.1017/jfm.2018.184 Published online by Cambridge University Press

precessional motions. The angular velocity vector of the spheroid in the tumbling and spinning orbits is respectively perpendicular and parallel to $\boldsymbol{p}$. For any fixed C, the orbit phase τ varies from 0 to 2π and changes at a constant rate (despite ϕ_j changing at a variable rate). The equations for the rates of change take a simple form in the orbital coordinate system, and are given by

$$\frac{\mathrm{d}C}{\mathrm{d}t} = 0, \tag{4.4}$$

$$\frac{\mathrm{d}\tau}{\mathrm{d}t} = \frac{(1-\lambda)\kappa_{eq}}{(\kappa_{eq}^2+1)}. \tag{4.5}$$

Evidently, C does not change in the Stokes limit. It should be noted that the above equations are valid for $-1<\lambda<\lambda_{crit}$. In the limit of $\lambda\to-1$, that is, the trivial case of solid-body rotation, κ_{eq} is 1, and the orbits are merely circles transverse to the ambient vorticity. In the limit of $\lambda\to\lambda_{crit}^{-}$, $\kappa_{eq}\to\infty$ (0) for a prolate (an oblate) spheroid, and the angular velocity $\mathrm{d}\tau/\mathrm{d}t\to 0$, consistent with the transition to an open-trajectory topology across $\lambda=\lambda_{crit}$.

5. The effect of particle inertia: massive spheroids ($Re=0$ and $St\ll 1$)

In this section, we investigate the effect of particle inertia on the orientation dynamics of a spheroid in a planar linear flow. This analysis is important for finding the orientation of particles in solid–gas systems where $\rho_p\gg\rho_f$; an example in this regard is the orientation distribution of ice crystals in atmospheric turbulence, which is relevant to the determination of cirrus cloud reflectivities, a crucial component of the Earth–atmosphere radiation budget (Liou 1986). The $O(St)$ correction to the angular velocity of a spheroid in a planar linear flow was derived in an invariant form by Einarsson *et al.* (2014). However, they restricted their analysis to finding the orbit that is stabilized at long times for the particular case of simple shear flow ($\lambda=0$). Below, we present the orbits stabilized by particle inertia in the entire λ–κ plane ($\lambda<\lambda_{crit}$; see figure 2). For completeness, we present the calculation of the $O(St)$ correction to the angular velocity using (2.4) by setting $Re=0$, whence (2.4) reduces to

$$\boldsymbol{\Omega}_1\cdot\boldsymbol{L}_2 \;=\; \boldsymbol{\Gamma}:\int_{S_p}\boldsymbol{x}(\boldsymbol{\Sigma}^{(2)}\cdot\boldsymbol{n})\,\mathrm{d}S + St\,\frac{\mathrm{d}}{\mathrm{d}t}(\boldsymbol{I}_p\cdot\boldsymbol{\Omega}_1). \tag{5.1}$$

The second term on the right-hand side gives the correction due to the particle angular acceleration. As mentioned earlier, it is convenient to evaluate the correction in the body-aligned coordinate system (XYZ in figure 1*f*), which rotates with $\boldsymbol{\Omega}^t_{jeff}$. Noting that the rate of change in the space-fixed coordinate system is related to the rate of change in the body-aligned one as $\mathrm{d}/\mathrm{d}t(.)=(\mathrm{d}/\mathrm{d}t(.))_b+\boldsymbol{\Omega}^t_{jeff}\wedge(.)$, the subscript '$b$' denoting the XYZ system, and that the moment of inertia tensor is now a constant, (5.1) takes the form

$$\boldsymbol{\Omega}_1\cdot\boldsymbol{L}^{(2)} \;=\; \boldsymbol{\Gamma}:\int_{S_p}\boldsymbol{x}(\boldsymbol{\Sigma}^{(2)}\cdot\boldsymbol{n})\,\mathrm{d}S + St\left[\boldsymbol{I}_p\cdot\left(\frac{\mathrm{d}\boldsymbol{\Omega}_1}{\mathrm{d}t}\right)_b+\boldsymbol{\Omega}^t_{jeff}\wedge(\boldsymbol{I}_p\cdot\boldsymbol{\Omega}_1)\right]. \tag{5.2}$$

Using a regular expansion of the form $\boldsymbol{\Omega}_1=\boldsymbol{\Omega}_{jeff}+St\,\boldsymbol{\Omega}^{(1)}_{1St}+O(St^2)$ for the particle angular velocity, one obtains

$$\boldsymbol{\Omega}^{(1)}_{1St}\cdot\boldsymbol{L}^{(2)} \;=\; \boldsymbol{I}_p\cdot\frac{\mathrm{d}\boldsymbol{\Omega}_{jeff}}{\mathrm{d}t_{jeff}}+\boldsymbol{\Omega}^t_{jeff}\wedge(\boldsymbol{I}_p\cdot\boldsymbol{\Omega}_{jeff}), \tag{5.3}$$

https://doi.org/10.1017/jfm.2018.184 Published online by Cambridge University Press

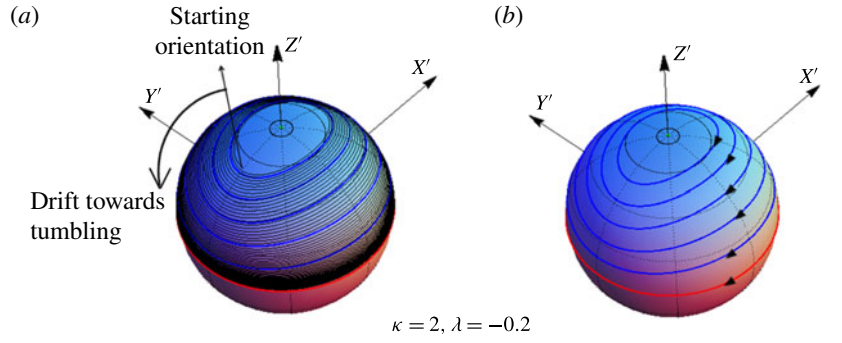


FIGURE 3. (Colour online) (*a*) The finite-*St* inertial trajectory (black) is plotted on a unit sphere for a prolate spheroid with $\kappa = 2$ in an elliptic linear flow with $\lambda = -0.2$. For purposes of illustration, the Stokes number is chosen to be unity. The tumbling orbit is the red curve. The blue curves on the unit sphere in (*a*) and (*b*) are the Jeffery orbits.

at $O(St)$. In (5.3), to leading order, $(\mathrm{d}/\mathrm{d}t)_b$ is replaced by $(\mathrm{d}/\mathrm{d}t)_{jeff}$, where the latter denotes the rate of change along the closed orbit in the Stokes limit, given by (2.2) and (2.3) in terms of θ_j and ϕ_j. The rates of change of ϕ_j and θ_j, at $O(St)$, can be obtained from (5.3), $\dot{\phi}_{jSt} = -\Omega_{1St}^{(1)x}/\sin\theta_j$ and $\dot{\theta}_{jSt} = \Omega_{1St}^{(1)y}$, and are given by

$$\left(\frac{\mathrm{d}\theta_j}{\mathrm{d}t}\right)_{St} = \sin\theta_j\cos\theta_j\left[F_1^p(\xi_0,\lambda) + F_2^p(\xi_0,\lambda)\cos 2\phi_j + F_3^p(\xi_0,\lambda)\cos 2\theta_j + F_4^p(\xi_0,\lambda)\cos 4\phi_j + F_5^p(\xi_0,\lambda)\cos(2\theta_j - 4\phi_j) + F_6^p(\xi_0,\lambda)\cos(2\theta_j + 4\phi_j)\right], \tag{5.4}$$

$$\left(\frac{\mathrm{d}\phi_j}{\mathrm{d}t}\right)_{St} = \sin\phi_j\cos\phi_j\left[G_1^p(\xi_0,\lambda) + G_2^p(\xi_0,\lambda)\cos 2\theta_j + G_3^p(\xi_0,\lambda)\cos 2\phi_j + G_4^p(\xi_0,\lambda)\cos 2\theta_j\cos 2\phi_j\right]. \tag{5.5}$$

The functions of ξ_0 and λ that appear above for a prolate spheroid are given in appendix B. The expressions in (5.4) and (5.5) are consistent with those given by Einarsson *et al.* (2014).

In the analysis that follows, we investigate the effect of the inertial corrections given in (5.4) and (5.5) on the trajectory of the orientation vector for all (λ, κ) combinations below the λ_{crit} curve in figure 2. There are two approaches to carry out this investigation. The first, brute-force, approach is to numerically integrate the differential equations governing θ_j and ϕ_j, obtained by adding the angular velocities given in (5.4) and (5.5) and the corresponding leading-order angular velocities given in (2.3) and (2.2), to obtain the inertial trajectory on the unit sphere. The trajectory obtained in the manner described above, starting from a particular initial condition ($St = 1$, $\theta_{j0} = 0.5$, $\phi_{j0} = \pi$), is shown in figure 3(*a*) for a prolate spheroid of aspect ratio 2 in an elliptic flow with $\lambda = -0.2$. The Jeffery orbits, for the same set of parameters, are plotted in figure 3(*b*) for purposes of comparison. As is evident, the spheroid drifts towards the tumbling orbit (red curve on the unit sphere in figure 3*a*). It is cumbersome to repeat this exercise for the whole (κ–λ) plane below the λ_{crit} curve in figure 2, and for all possible initial orientations, and this is not pursued further.

https://doi.org/10.1017/jfm.2018.184 Published online by Cambridge University Press

In the second approach, the orbital drift, defined as the change in orbit constant per Jeffery period, is evaluated. To do this, one first differentiates (4.2), to obtain

$$\frac{\mathrm{d}C}{\mathrm{d}t} = \frac{C}{\sin\theta_j\cos\theta_j}\frac{\mathrm{d}\theta_j}{\mathrm{d}t} + \frac{C(\kappa_{eq}^2-1)\cos\phi_j\sin\phi_j}{\kappa_{eq}^2\sin^2\phi_j+\cos^2\phi_j}\frac{\mathrm{d}\phi_j}{\mathrm{d}t}. \tag{5.6}$$

Since $\mathrm{d}C/\mathrm{d}t = 0$ at leading order, equation (5.6) takes the form

$$\frac{\mathrm{d}C}{\mathrm{d}t} = St\,C\left[\frac{1}{\sin\theta_j\cos\theta_j}\left(\frac{\mathrm{d}\theta_j}{\mathrm{d}t}\right)_{St} + \frac{(\kappa_{eq}^2-1)\cos\phi_j\sin\phi_j}{\kappa_{eq}^2\sin^2\phi_j+\cos^2\phi_j}\left(\frac{\mathrm{d}\phi_j}{\mathrm{d}t}\right)_{St}\right], \tag{5.7}$$

where $(\mathrm{d}\theta_j/\mathrm{d}t)_{St}$ and $(\mathrm{d}\phi_j/\mathrm{d}t)_{St}$ are given by (5.4) and (5.5). As expected, the change in C is at $O(St)$, and leads to an inertial trajectory where the spheroid orientation vector spirals towards either the flow-gradient plane or the spinning orbit. For $St \ll 1$, this spiralling is tight, with each turn of the spiral closely approximating a Jeffery orbit (see figure 3*a*). The orbital drift can then be conveniently characterized by the pitch of the inertial spiral measured in units of C. This pitch, ΔC, defined at leading order as the change in C during a single Jeffery period ($T_{jeff} = 2\pi(\kappa_{eq}^2+1)/((1-\lambda)\kappa_{eq})$), is given by

$$\Delta C_p = \int_0^{T_{jeff}} \frac{\mathrm{d}C}{\mathrm{d}t}\,\mathrm{d}t, \tag{5.8}$$

$$= St\frac{\kappa_{eq}^2+1}{(1-\lambda)\kappa_{eq}}\int_0^{2\pi} C\left(\frac{1}{\sin\theta_j\cos\theta_j}\left(\frac{\mathrm{d}\theta_j}{\mathrm{d}t}\right)_{St} + \frac{(\kappa_{eq}^2-1)\cos\phi_j\sin\phi_j}{\kappa_{eq}^2\sin^2\phi_j+\cos^2\phi_j}\left(\frac{\mathrm{d}\phi_j}{\mathrm{d}t}\right)_{St}\right)\mathrm{d}\tau, \tag{5.9}$$

where the subscript 'p' denotes particle inertia. The τ integrals in (5.9) are to be evaluated for fixed C, implying closeness of the inertial spiralling trajectory at a given point to a Jeffery orbit passing through the same point. Using (5.4) and (5.5), one obtains

$$\begin{aligned}\Delta C_p = St\,C\frac{\kappa_{eq}^2+1}{(1-\lambda)\kappa_{eq}}\big\{&\big[I_1F_1^p(\xi_0,\lambda)+I_2F_2^p(\xi_0,\lambda)+I_3F_3^p(\xi_0,\lambda)+I_4F_4^p(\xi_0,\lambda)\\ &+I_5F_5^p(\xi_0,\lambda)+I_6F_6^p(\xi_0,\lambda)\big]\\ &+\big[J_1G_1^p(\xi_0,\lambda)+J_2G_2^p(\xi_0,\lambda)+J_3G_3^p(\xi_0,\lambda)+J_4G_4^p(\xi_0,\lambda)\big]\big\}.\end{aligned} \tag{5.10}$$

The expressions for I_1–J_4, as functions of C and κ_{eq}, are given in appendix C. The orbital drift approximation in (5.10) has reduced the need from a consideration of all possible initial orientations in the brute-force approach mentioned earlier to a one-dimensional examination of all possible values of C. The average change, however, should be much less than C, and, therefore, the above analysis implies $((\Delta C)/C) \ll 1$. It can be seen from (5.10) that this condition breaks down when $St \sim \kappa_{eq}(1/\kappa_{eq})$, corresponding to oblate (prolate) spheroids with $\kappa_{eq} \ll 1$ ($\kappa_{eq} \gg 1$) (the F_i and G_i values remain of order unity except in the limit $\kappa_{eq} \to \infty$, that is, for slender fibres in a flow close to simple shear; in this case, the F_i and G_i values are $O(1/\log\kappa_{eq})$, and the St corresponding to the breakdown is $O(\log\kappa_{eq}/\kappa_{eq})$). This would mean that close to the

https://doi.org/10.1017/jfm.2018.184 Published online by Cambridge University Press

λ_{crit} curve in figure 2, the orbital drift approximation becomes increasingly restrictive, being valid only when $St \ll \kappa_{eq}$ or $1/\kappa_{eq}$. It is shown later, in § 8, that the orbital drift interpretation, motivated here using physical arguments, emerges naturally as the leading-order term in the framework of a multiple time scale analysis. The limitations of this interpretation in the limits of $\kappa_{eq} \to 0$ and ∞ are also discussed therein.

The orbital drift in (5.10) is a function of C and λ as well as κ (through ξ_0 which is the inverse of the spheroid eccentricity). The drift is positive for a prolate spheroid of any aspect ratio in a planar linear flow with a non-positive λ (all elliptic linear flows, including the limiting case of solid-body rotation and simple shear flow). Thus, a prolate spheroid in any flow with $\lambda \leqslant 0$ approaches the tumbling orbit for long times; this is expected for $\lambda = -1$, where one expects the particle to centrifuge outward towards the tumbling orbit (in the absence of the $O(Re)$ contribution arising from centrifugal buoyancy). This is noted in the fourth quadrant of the λ–κ plane in figure 4(*a*). In a hyperbolic flow ($0 < \lambda < \lambda_{crit}$), the tumbling orbit continues to be the long-time orientation limit for a prolate spheroid with κ greater than approximately 30. However, if the aspect ratio of the spheroid is smaller than 30, the tumbling orbit is stabilized at long times only until a particular $\lambda_1(\kappa)$ ($0 < \lambda_1 < \lambda_{crit}$), indicated by the red curve in the first quadrant of figure 4(*a*). For these aspect ratios, if λ is larger than λ_1, a repeller (a Jeffery orbit at the order of approximation considered) exists on each unit hemisphere, dividing it into two distinct basins of attraction, with the attractor being the tumbling orbit for one basin and the spinning orbit for the other. The shaded region in figure 4(*a*) corresponds to all those λ values for which two distinct basins of attraction exist on the unit hemisphere. Eventually, with increasing λ, the spinning orbit becomes the sole attractor at a particular $\lambda_2(\kappa)$ ($\lambda_1 < \lambda_2$), indicated by the magenta curve in the zoomed plot in figure 4(*b*), and remains so for the narrow range of λ in the interval $\lambda_2(\kappa) < \lambda < \lambda_{crit}$, with $\lambda_2 \to \lambda_{crit}$ for an aspect ratio approximately equal to 30.

In figure 4(*c*), the orbital drift ΔC_p is plotted against $C/(C+1)$ for a particular prolate spheroid with $\kappa = 2$ for different values of λ. The drift is positive for all λ values below $\lambda \approx 0.13$ (λ_1 for $\kappa = 2$), and the long-time orientation dynamics approaches the tumbling orbit. As λ becomes larger than 0.13, the sign of the drift changes across a critical C (Jeffery orbit with $C = C^*$, say). This Jeffery orbit, which acts as a repeller, emerges from the spinning orbit at around $\lambda = 0.13$ (λ_1), and with increasing λ, moves towards the tumbling orbit, eventually coinciding with it at $\lambda \approx 0.20$ (λ_2 for $\kappa = 2$). The repeller orbits for $\kappa = 2$ at various λ values are plotted on the unit sphere in figure 4(*d–f*).

The long-time orientation dynamics of an oblate spheroid is simpler compared with that of the prolate spheroid above. An oblate spheroid drifts towards the spinning orbit irrespective of its initial orientation and aspect ratio in any planar linear flow with $\lambda < \lambda_{crit}$. In figure 5(*b*), the orbital drift is plotted against $C/(C+1)$ for various λ values for an oblate spheroid of aspect ratio 0.1, and is negative irrespective of C and λ.

6. The effect of fluid inertia ($St = 0$ and $Re \ll 1$)

In this section, we investigate the effect of fluid inertia on the orientation dynamics of a spheroid in a planar linear flow. The effect of fluid inertia on the orientation dynamics in the particular case of simple shear flow ($\lambda = 0$) has already been analysed in earlier works (Einarsson *et al.* 2015; Dabade *et al.* 2016). It was shown that, depending on the aspect ratio as well as the ratio St/Re, the effect of fluid

https://doi.org/10.1017/jfm.2018.184 Published online by Cambridge University Press

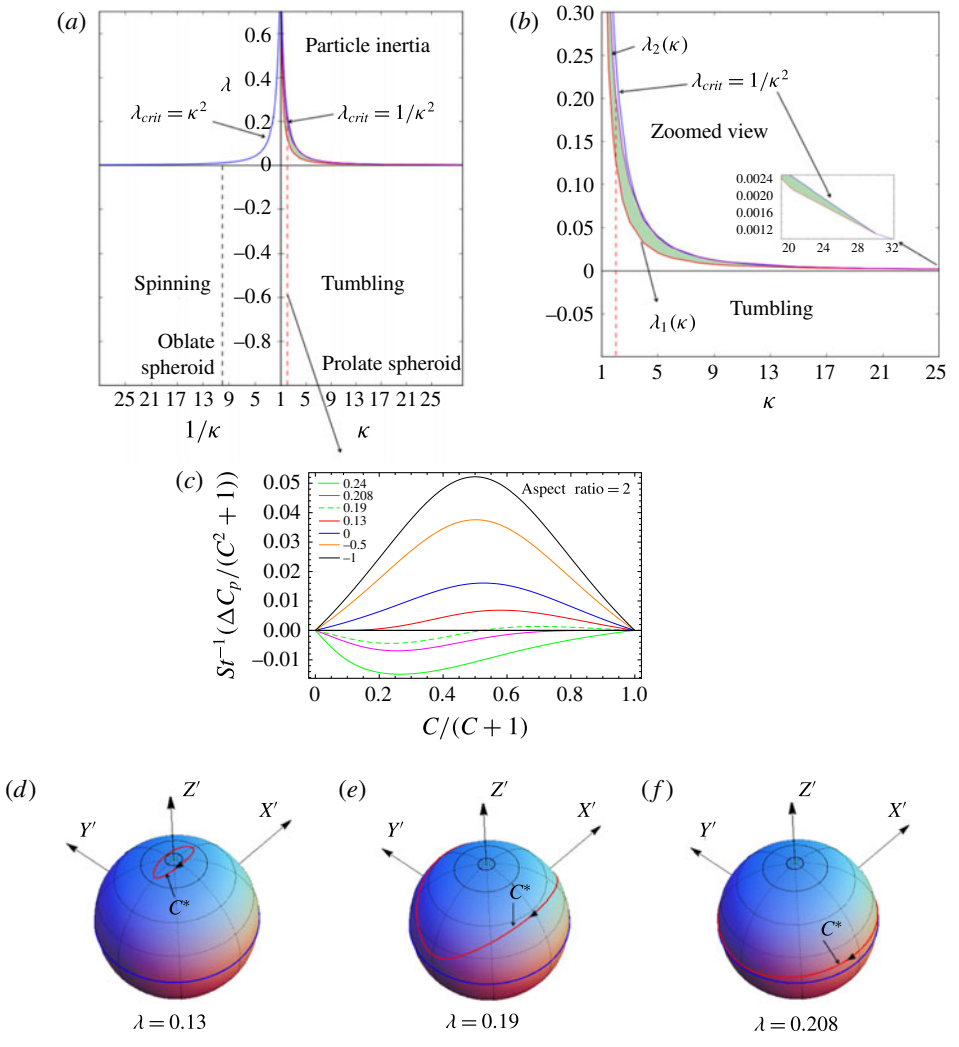


FIGURE 4. (Colour online) (*a*) The orbit(s) stabilized at long times, due to particle inertia, are identified for all combinations of λ–κ below the λ_{crit} curve (blue curve). The red curve (the zoomed view of this curve is denoted by $\lambda_1(\kappa)$ in *b*) denotes the locus of (λ, κ) values at which the repeller emerges from the spinning orbit. The shaded region denotes the (λ, κ) combinations for which there is a repeller on the unit hemisphere. (*b*) A zoomed view that shows the bounding curves $\lambda_1(\kappa)$ and $\lambda_2(\kappa)$. (*c*) The orbital drift is plotted against $C/(C+1)$ for a prolate spheroid of $\kappa=2$ for various values of λ. The C at which drift changes sign corresponds to the repeller (C^*) location, which migrates from the spinning orbit ($C/(C+1)=0$) to the tumbling orbit ($C/(C+1)=0$) with increasing λ. The repeller orbits (red) are plotted for a prolate spheroid of aspect ratio 2, and for λ values of (*d*) 0.13 (*e*) 0.19 and (*f*) 0.208 (the tumbling orbit in all cases is shown in blue).

inertia can either oppose or complement that due to particle inertia. In planar linear flow, the rates of change of ϕ_j and θ_j, at $O(Re)$, are obtained by evaluating the integrals proportional to Re on the right-hand side of (2.4), using the velocity fields

https://doi.org/10.1017/jfm.2018.184 Published online by Cambridge University Press

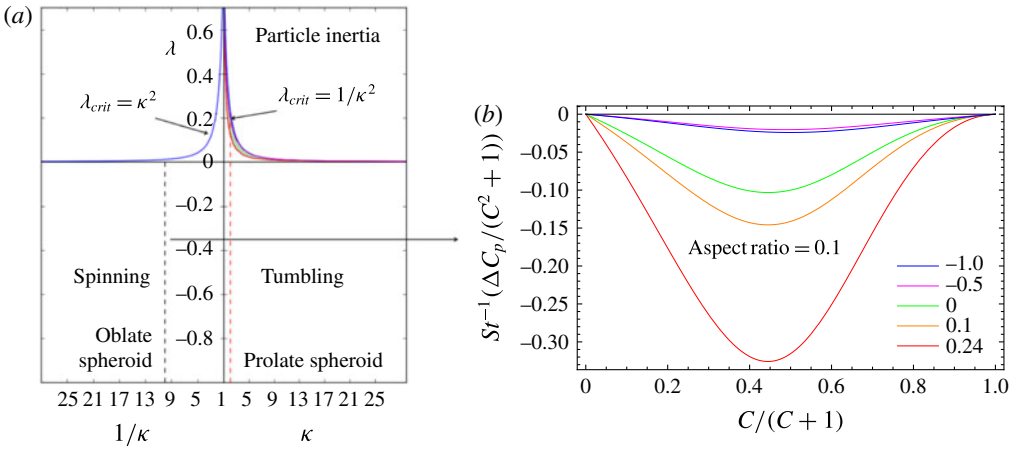


FIGURE 5. (Colour online) (*a*) The orbits stabilized at long times, due to particle inertia, are indicated. (*b*) The orbital drift is plotted against $C/(C+1)$ for an oblate spheroid of aspect ratio 0.1 for various values of λ. The drift does not change sign for an oblate spheroid.

given in § 3, and are given by

$$\left(\frac{\mathrm{d}\theta_j}{\mathrm{d}t}\right)_{Re} = \sin\theta_j\cos\theta_j\left[F_1^f(\xi_0,\lambda) + F_2^f(\xi_0,\lambda)\cos 2\phi_j + F_3^f(\xi_0,\lambda)\cos 2\theta_j + F_4^f(\xi_0,\lambda)\cos 4\phi_j + F_5^f(\xi_0,\lambda)\cos(2\theta_j - 4\phi_j) + F_6^f(\xi_0,\lambda)\cos(2\theta_j + 4\phi_j)\right], \tag{6.1}$$

$$\left(\frac{\mathrm{d}\phi_j}{\mathrm{d}t}\right)_{Re} = \sin\phi_j\cos\phi_j\left[G_1^f(\xi_0,\lambda) + G_2^f(\xi_0,\lambda)\cos 2\theta_j + G_3^f(\xi_0,\lambda)\cos 2\phi_j + G_4^f(\xi_0,\lambda)\cos(2\theta_j)\cos(2\phi_j)\right]. \tag{6.2}$$

The functions of ξ_0 and λ that appear above for a prolate spheroid are given in appendix B. The analytical approach introduced in § 5 is used to evaluate the orbital drift due to fluid inertia, which is given by

$$\Delta C_f = Re\, C\,\frac{\kappa_{eq}^2+1}{(1-\lambda)\kappa_{eq}}\left\{\left[I_1F_1^f(\xi_0,\lambda) + I_2F_2^f(\xi_0,\lambda) + I_3F_3^f(\xi_0,\lambda) + I_4F_4^f(\xi_0,\lambda) + I_5F_5^f(\xi_0,\lambda) + I_6F_6^f(\xi_0,\lambda)\right] + \left[J_1G_1^f(\xi_0,\lambda) + J_2G_2^f(\xi_0,\lambda) + J_3G_3^f(\xi_0,\lambda) + J_4G_4^f(\xi_0,\lambda)\right]\right\}, \tag{6.3}$$

where the I_i and J_i terms are the same as those in § 5.

The sign of the fluid inertial drift varies in a non-trivial manner with λ for both prolate and oblate spheroids. The orbits stabilized by fluid inertia, for long times, for all λ values below the λ_{crit} curve in figure 2, are indicated in figure 6(*a*). For a prolate spheroid of any aspect ratio in solid-body rotation ($\lambda = -1$), the orbital drift is negative for all values of C and the spheroid drifts towards the spinning

https://doi.org/10.1017/jfm.2018.184 Published online by Cambridge University Press

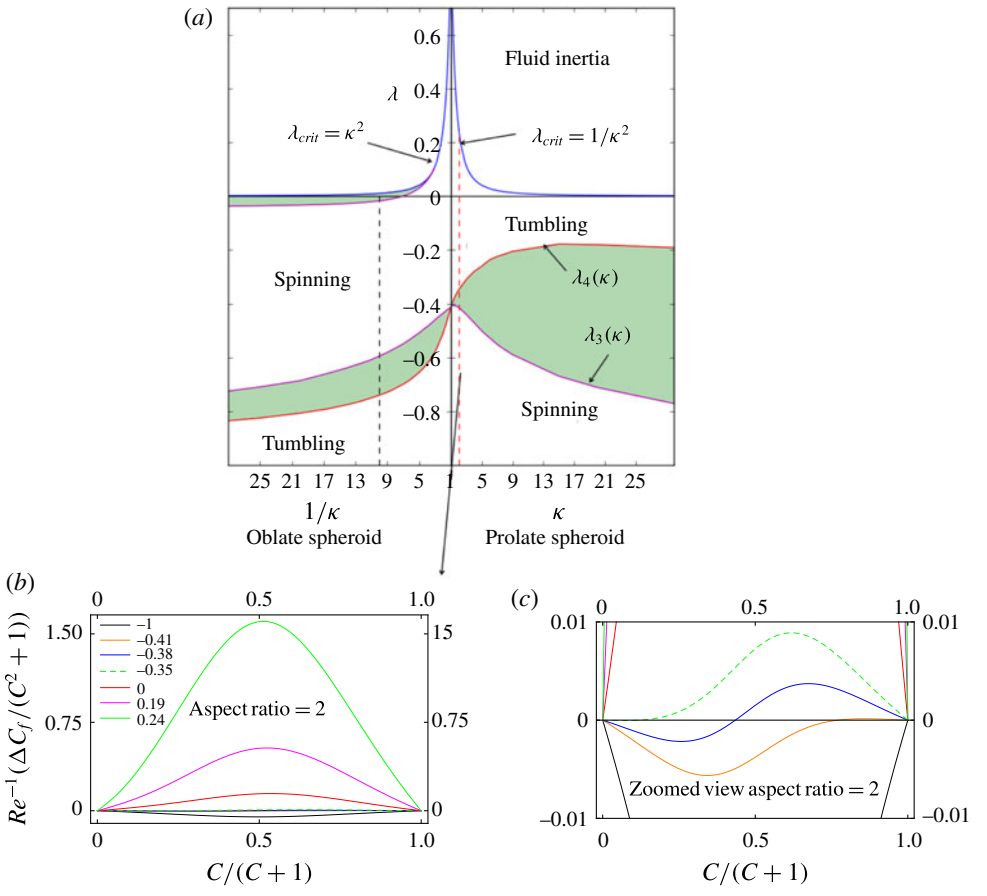


FIGURE 6. (Colour online) (*a*) The orbit(s) that are stabilized at long times, due to fluid inertia, are identified for all (λ, κ) combinations below the λ_{crit} curve (blue). The shaded regions correspond to the (λ, κ) combinations for which there are two distinct basins of attraction separated by a repeller. The red ($\lambda_4(\kappa)$) and magenta ($\lambda_3(\kappa)$) curves correspond to all combinations of (λ, κ) for which the repeller coincides with the spinning and the tumbling orbits respectively. (*b*) The drift is plotted against $C/(C+1)$ for a prolate spheroid of aspect ratio 2 for various λ values. (*c*) Zoomed view of (*b*).

orbit. This is expected because in solid-body rotation, the pressure gradient set up by the base state inertial forces results in a radially inward buoyancy force, which stabilizes the spinning orbit. The spinning orbit continues to be the stable orbit for all λ values less than a particular λ that is a function of the aspect ratio. This latter threshold is denoted by $\lambda_3(\kappa)$ (< 0) and is indicated by the magenta curve in the fourth quadrant in figure 6(*a*). At $\lambda = \lambda_3$, a repeller emerges from the tumbling orbit, splitting the orientation space on each unit hemisphere, for larger λ values, into two distinct basins of attraction, with the attractors being the tumbling and the spinning orbits. The repeller moves towards the spinning orbit with increasing λ, eventually merging with it at a second λ denoted by $\lambda_4(\kappa)$ (<0 and indicated by the red curve in the fourth quadrant in figure 6*a*). The shaded region in figure 6(*a*) indicates the (λ, κ) combinations for which the fluid inertial drift changes sign across a certain

https://doi.org/10.1017/jfm.2018.184 Published online by Cambridge University Press

Jeffery orbit (the repeller), leading to two distinct basins of attraction. On either side of this region, that is for λ values in the ranges $\lambda_4 < \lambda < \lambda_{crit}$ and $-1 < \lambda < \lambda_3$, the tumbling and spinning orbits respectively remain the sole attractors. In figure 6(*b*), the orbital drift is plotted against $C/(C+1)$ for a spheroid with $\kappa = 2$ to illustrate the abovementioned bifurcation. The shifting of the repeller location from tumbling to spinning, as one traverses the shaded bifurcation region ($\lambda_3 < \lambda < \lambda_4$) in figure 6(*a*), can be seen in the magnified view in figure 6(*c*).

An oblate spheroid drifts from any initial orientation towards the tumbling orbit for $\lambda = -1$, again driven by the buoyancy contribution associated with the ambient pressure field. However, there exist ranges of λ for which there are two distinct basins of attraction separated by a repeller on the unit hemisphere. The first range is indicated by the shaded region, bounded by the curves $\lambda_3(\kappa)$ and $\lambda_4(\kappa)$, in the third quadrant in figure 7(*a*). Unlike the prolate spheroid, the repeller in this case first emerges from the spinning orbit at $\lambda = \lambda_3(\kappa)$ (red curve in the third quadrant of figure 7*a*) and shifts towards the tumbling orbit with increasing λ, finally merging with it when $\lambda = \lambda_4(\kappa)$ (the magenta curve in the third quadrant of figure 7*a*). There arises a second bifurcation for $\lambda > \lambda_4(\kappa)$, and this is confined to the region bounded between the curves $\lambda = \lambda_5(\kappa)$ and $\lambda = \lambda_{crit}$. These two curves meet at κ of approximately 0.324 ($\lambda = 0.105$), so that this second bifurcation is restricted to oblate spheroids smaller than this aspect ratio. For this bifurcation, the repeller (at $C = C^*$, say) first emerges from the tumbling orbit at $\lambda = \lambda_5$ and flattens out into increasingly thin ellipses centred around the gradient–vorticity plane as $\lambda \to \lambda_{crit}$. Interestingly, at $\lambda = \lambda_{crit}$, the repeller does not shrink to a point, but instead reduces to an arc of the great circle in which the gradient–vorticity plane intersects the unit sphere. This is because C^* remains finite in the limit of $\kappa_{eq} \to 0$ ($\lambda \to \lambda_{crit}$), the angular extent of the arc being $\theta_j = \tan^{-1} C^*$ (see (4.2)). In figure 7(*b*), the orbital drift is plotted for an aspect ratio of 0.1 to show the abovementioned bifurcations. The shifting of the repeller location in the shaded bifurcation region ($\lambda_3 < \lambda < \lambda_4$) in the third quadrant of figure 7(*a*) is plotted in figure 7(*c*) and the shifting in the shaded region corresponding to $\lambda > \lambda_5$ is plotted in figure 7(*d*). The angular extent of the limiting repeller arc (as $\lambda \to \lambda_{crit}$) is 163° for the aspect ratio of 0.1. The angular extent of the repeller arc increases from approximately 161° for simple shear flow (Dabade *et al.* 2016) to 180° (a semicircle) for $\lambda = 0.324$.

7. The effect of fluid inertia on neutrally buoyant spheroids ($Re = St$)

The inertial drifts presented in the earlier sections apply to certain limiting scenarios. The drift in § 5 is relevant to massive spheroids that occur in gas–solid systems, whereas the drift in § 6 is relevant to hollow spheroids in an inertial ambient, both in the absence of gravity (due to the neglect of sedimentation torque; see Dabade, Marath & Subramanian 2015). In this section, we investigate the combined effect of the fluid and particle inertial drifts on the orientation of a neutrally buoyant spheroid ($\rho_p = \rho_f$, $Re = St$) in a planar linear flow.

The drifts given in (5.10) and (6.3) are summed up to obtain the drift for a neutrally buoyant spheroid. The orbits stabilized by the combined drift at long times are indicated in figure 8. For a prolate spheroid, irrespective of λ (provided that it lies in the interval $(-1, \lambda_{crit})$) and κ, this is the tumbling orbit. For an oblate spheroid of a given aspect ratio, there exists a critical λ ($\hat{\lambda}_5(\kappa)$) below which the steady state is the spinning orbit (provided that $\lambda \neq -1$), with $\hat{\lambda}_5(\kappa)$ approaching λ_{crit} as the aspect ratio increases to approximately 0.323 ($\lambda = 0.104$). It should be noted that this aspect ratio where $\hat{\lambda}_5(\kappa) = \lambda_{crit}$ is very close the aspect ratio defined

https://doi.org/10.1017/jfm.2018.184 Published online by Cambridge University Press

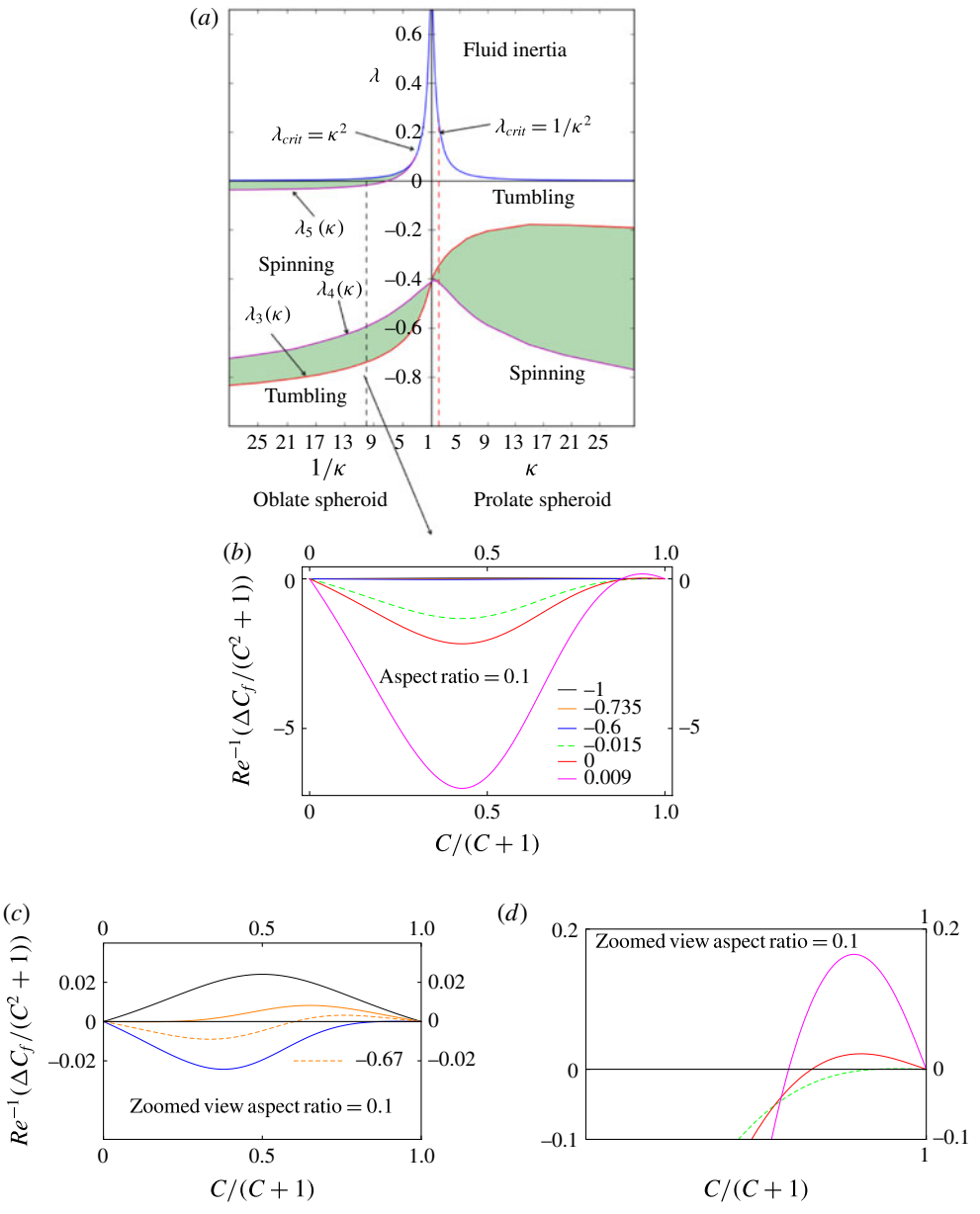


FIGURE 7. (Colour online) (*a*) The orbits that are stabilized at long times, due to fluid inertia, are identified for all (λ, κ) combinations below the λ_{crit} curve (blue). (*b*) The drift is plotted against $C/(C+1)$ for an oblate spheroid of aspect ratio 0.1 for various λ values. (*c*,*d*) Zoomed views of (*b*) to show the shifting of the repeller in the two bifurcation regions identified in (*a*).

by $\lambda_5(\kappa) = \lambda_{crit}$ in § 6, implying that the drift due to fluid inertia dominates that due to particle inertia. For $\kappa < 0.323$ and $\hat{\lambda}_5(\kappa) < \lambda < \lambda_{crit}$, there exists a repeller, as seen in the earlier sections, and the (λ, κ) combinations in this range are indicated

https://doi.org/10.1017/jfm.2018.184 Published online by Cambridge University Press

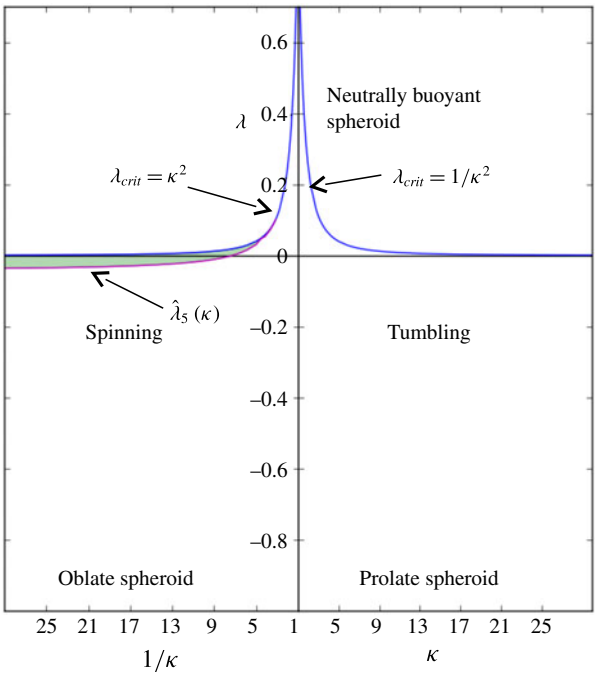


FIGURE 8. (Colour online) The orbits stabilized for a neutrally buoyant spheroid ($Re = St$) in the λ–κ plane by the combined particle and fluid inertial drifts. The shaded region for the oblate spheroid corresponds to the (λ, κ) combinations for which the final steady state can be either the tumbling or the spinning orbit depending on the initial spheroid orientation.

by the shaded region in figure 8. It should be noted that for a given positive λ, the minimum aspect ratio for which the bifurcation above exists is given by $\kappa = \sqrt{\lambda}$. For $-0.043 < \lambda < 0$, there is no lower bound, and, thus, there exist non-trivial basins of attraction corresponding to both tumbling and spinning orbits for oblate spheroids of an arbitrarily small aspect ratio. It is interesting to compare figures 5(*a*), 7(*a*) and 8. If the λ values are closer to simple shear than solid-body rotation, for instance in the range $\lambda_5(\kappa) < \lambda < \lambda_{crit}$, the drift due to fluid inertia dominates that due to particle inertia. Thus, the bifurcation region in this range, in figure 7(*a*), is altered by a very small amount, as is also evident from the change in the aforementioned upper critical aspect ratio (this is consistent with the observation by Dabade *et al.* (2016) that fluid inertia remains dominant for neutrally buoyant spheroids in simple shear). However, the bifurcation regions in the range $\lambda_3(\kappa) < \lambda < \lambda_4(\kappa)$, which exist due to the fluid inertial drift alone, vanish for neutrally buoyant spheroids, since the drift due to particle inertia tends to be stronger than the fluid inertial drift when the ambient vortical component dominates the extensional component. In the case of solid-body rotation, the drift on a neutrally buoyant spheroid is zero for both prolate and oblate spheroids, as must be the case, due to the exact compensation between the centrifugal buoyancy and the centrifugal force on the particle itself. Thus, for $\lambda = -1$, the trajectory of a neutrally buoyant spheroid is a circle with $\boldsymbol{p} \cdot \mathbf{1}_z'$ being a constant, which is determined by its initial condition.

https://doi.org/10.1017/jfm.2018.184 Published online by Cambridge University Press

8. A multiple time scale description of inertial orientation dynamics

The orbital drifts in (5.10) and (6.3) were derived from (5.6) based on an assumption that C remains constant over a given turn of the actual finite-Re (or -St) trajectory that is a tight inertial spiral (an example of such a spiralling trajectory was shown in figure 3). As mentioned in § 5, for Re, $St \ll 1$, the advantage of such an approximation is that it reduces the need to numerically integrate the differential equations governing θ_j and ϕ_j over initial orientations spanning the entire unit sphere to the determination of ΔC_f (or ΔC_p) as a function of C alone. In § 8.1, we derive the expression for the orbital drift formally using a multiple time scale analysis, and rigorously substantiate the above physically motivated characterization of inertial effects. This also allows one to discuss the limitations of the orbital drift approximation in § 8.2, and thereby derive a better approximation for extreme aspect ratio particles (slender fibres and flat disks).

8.1. *A multiple-scale-based derivation of the orbital drift approximation*

The inertial drift occurs on a slow time scale ($t_2 \sim Re^{-1}\dot{\gamma}^{-1}$ or $St^{-1}\dot{\gamma}^{-1}$) compared with the time scale of the leading-order Stokesian convection ($t_1 \sim \dot{\gamma}^{-1}$). The orbital coordinate of the spheroid can then be written as a two-time-scale series, $C = C_0(t_1, t_2) + Re$ (or St)$C_1(t_1, t_2) + O(Re^{3/2}$ (or St^2)), where C_0 will turn out to be the orbital drift at leading order discussed above and C_1 is the fluctuation about the average. The distinction between the fast and slow time scales arises from the fact that there can be no secular growth on the t_1 scale. As is the case in this formalism (Bender & Orszag 1999), this is enforced by the condition that C be a periodic function of t_1, with period $T_{jeff}(=2\pi(\kappa_{eq}^2+1)/(1-\lambda)\kappa_{eq})$, for t_2 fixed. We will restrict our analysis to the fluid inertial drift, although an analogous analysis holds good for the particle inertia. Denoting the right-hand side of (5.6) as $Re\,H(C, \tau; \xi_0)$, with $\mathrm{d}\theta_j/\mathrm{d}t$ and $\mathrm{d}\phi_j/\mathrm{d}t$ given in (6.1) and (6.2), and noting that $\tau = (1-\lambda)\kappa_{eq}t_1/(\kappa_{eq}^2+1)$, (5.6) can be rewritten as $\mathrm{d}C/\mathrm{d}t = Re\,H(C, (1-\lambda)\kappa_{eq}t_1/(\kappa_{eq}^2+1); \xi_0)$. By substituting the series for C above and using the usual splitting of the time derivative into fast and slow components, $\mathrm{d}/\mathrm{d}t = (\mathrm{d}/\mathrm{d}t_1) + Re(\mathrm{d}/\mathrm{d}t_2)$, as part of the multiple scale formalism (Bender & Orszag 1999; Subramanian & Brady 2004), one obtains

$$\frac{\mathrm{d}C_0}{\mathrm{d}t_1} = 0 \tag{8.1}$$

at leading order and

$$\frac{\mathrm{d}C_1}{\mathrm{d}t_1} + \frac{\mathrm{d}C_0}{\mathrm{d}t_2} = H(C, (1-\lambda)\kappa_{eq}t_1/(\kappa_{eq}^2+1); \xi_0) \tag{8.2}$$

at $O(Re)$. The leading-order orbital drift C_0, which is the solution to (8.1) is therefore independent of t_1, that is, $C_0(t_1, t_2) = C_0(t_2)$. To evaluate both the dependence of C_0 on t_2 and the fluctuation C_1, one first integrates (8.2) over the Jeffery time period (the fast time scale), and noting that the integral of the first term on the left-hand side of (8.2) evaluates to zero on account of the aforementioned secularity condition, one obtains

$$\begin{aligned}\frac{\mathrm{d}C_0}{\mathrm{d}t_2} &= \frac{1}{T_{jeff}}\int_0^{T_{jeff}} H(C_0, (1-\lambda)\kappa_{eq}t_1/(\kappa_{eq}^2+1); \xi_0)\,\mathrm{d}t_1 \\ &= \frac{1}{2\pi}\int_0^{2\pi} H(C_0, \tau; \xi_0)\,\mathrm{d}\tau = \frac{\Delta C_f}{Re\,T_{jeff}},\end{aligned} \tag{8.3}$$

https://doi.org/10.1017/jfm.2018.184 Published online by Cambridge University Press

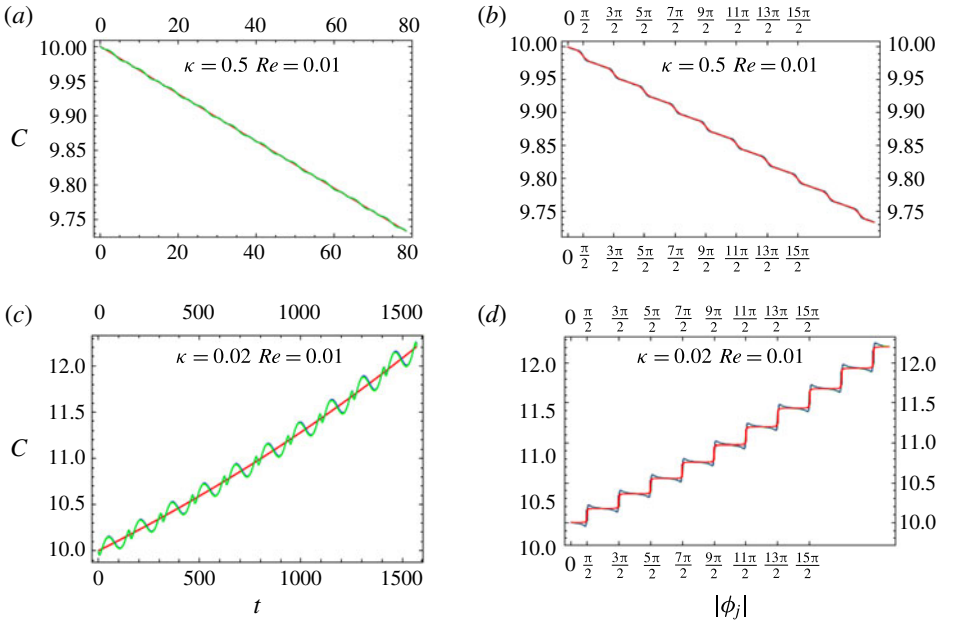


FIGURE 9. (Colour online) The orbital coordinate C as a function of time and $|\phi_j|$ starting from $C = 10$ and $\phi_j = 0$ for spheroids of aspect ratios 0.5 and 0.02 rotating in a simple shear flow. The calculation is based on (1) the orbital drift alone obtained from solving (8.3) (red), (2) the orbital drift together with the fluctuations (green) and (3) the C obtained from numerical integration of the governing equations of θ_j and ϕ_j (blue). In (*a*) and (*c*), C is plotted against time, and in (*b*) and (*d*), it is plotted against $|\phi_j|$.

where ΔC_f is the average change in C over a Jeffery time period, which was already evaluated in (6.3). Equation (8.3) is an autonomous differential equation governing C_0. Using (8.3) in (8.2), one obtains C_1 as

$$C_1 = \frac{T_{jeff}}{2\pi}\left(\int_0^{\tau} H(C_0, \tau'; \xi_0)\,\mathrm{d}\tau' - \frac{\tau\,\Delta C_f}{Re\,T_{jeff}}\right). \tag{8.4}$$

Thus, the multiple scale analysis allows one to fit ΔC_f into a differential equation for C, thereby allowing one to track the evolution of C with time.

In figure 9, we have plotted the C coordinate for neutrally buoyant spheroids ($Re = St$) of two different aspect ratios, rotating in a simple shear flow ($\kappa = \kappa_{eq}$), as a function of time as well as ϕ_j, starting from ($C = 10$, $\tau = \pi/2$ ($\phi_j = 0$)), using two methods. The first method numerically integrates the total angular velocities obtained from (5.4), (5.5), (6.1) and (6.2), and then evaluates $C(t)$ using its definition (4.2) in terms of $\theta_j(t)$ and $\phi_j(t)$. The second method uses the orbital drift obtained from the multiple-scale analysis presented above. For a neutrally buoyant spheroid, $H(C_0, \tau', \xi_0)$ would be a function of angular velocities obtained by summing that due to particle inertia given in (5.4) and (5.5) and that due to fluid inertia given in (6.1) and (6.2). The average change ΔC_f in (8.4) will be replaced by $\Delta C_f + \Delta C_p$, with ΔC_p given in (5.10). The integral on the right-hand side of (8.4) can be evaluated analytically. Since the result of the integration (a function of C_0, τ and ξ_0) is too cumbersome, we do not present it here. To evaluate C_1 in (8.4), one needs the value of C_0 at discrete instants

https://doi.org/10.1017/jfm.2018.184 Published online by Cambridge University Press

in time, which is obtained by numerically integrating (8.3) after accounting for the particle inertia contribution as mentioned above.

In figures 9(*a*) and 9(*c*), it can be seen that the results from the two methods compare well for oblate spheroids of different aspect ratios (the blue and green curves match almost exactly, and only one of them is therefore seen). It should be noted that the drift is a slowly varying function of time, although the degree of this variation depends on whether C is plotted as a function of t or ϕ_j. The latter amplifies the non-uniformity of the drift, as seen from comparing figures 9(*b*) and 9(*d*). This is due to the differing rates of change of ϕ_j with t for aligned (close to the gradient–vorticity plane) and non-aligned orientations (the inclusion of the fluctuation contribution C_1 accurately captures the non-monotonic variation of the orbit constant during the aligned phases). It can be seen that for the $O(1)$ (equivalent) aspect ratio oblate spheroid in figure 9(*b*), the drifts in the aligned ($\phi_j \approx -\pi/2, -3\pi/2$) and non-aligned phases ($\phi_j + \pi/2, \phi_j + 3\pi/2 \approx O(1)$) are of the same order. However, for the extreme aspect ratio spheroid in figure 9(*d*), the dominant drift occurs in the aligned phase. This is expected and can be seen from a simple scaling analysis. The $\mathrm{d}C/\mathrm{d}t$ in (5.6) is $O(Re\,C)$ in the extreme (equivalent) aspect ratio limit ($\kappa_{eq} \to 0$ or ∞). The rotation is, however, non-uniform, since the spheroid spends an $O(1)$ time in the non-aligned phase and an $O(1/\kappa_{eq})$ ($O(\kappa_{eq})$) time in the aligned phase if it is oblate (prolate). The total change in C during the aligned phase, $\Delta C_{aligned}$, would be $O(Re\,C/\kappa_{eq})$ ($O(Re\,C\kappa_{eq})$) for an oblate (a prolate) spheroid, and that during the non-aligned phase, $\Delta C_{non\text{-}aligned}$, would be $O(Re\,C)$. Thus, $\Delta C_{non\text{-}aligned}/\Delta C_{aligned}$ is $O(\kappa_{eq})$ ($O(1/\kappa_{eq})$) for an oblate (a prolate) spheroid, making the change in C much larger in the aligned phase for extreme equivalent aspect ratios. As explained earlier in § 5, the prediction from the multiple-scale analysis should eventually break down when Re or $St \sim \kappa_{eq}$ for an oblate spheroid. The cases plotted in figure 9 are for $Re = 0.01$, satisfying the restriction $Re < \kappa_{eq}$ ($\kappa_{eq} = \kappa$ for $\lambda = 0$) mentioned above, hence leading to the agreement of the numerics with the analytical predictions.

Relaxation of the above restriction, however, leads to a breakdown of the multiple-scale analysis, and, thence, the notion of a one-dimensional orbital drift. To illustrate the breakdown, in figure 10, we have plotted the evolution of C for a spheroid rotating in a simple shear flow ($\kappa = \kappa_{eq}$) for different values of Re, as a function of ϕ_j, starting from ($C = 10$, $\tau = \pi/2$ ($\phi_j = 0$)). Panels (*b*,*d*,*f*) in figure 10 are zoomed views of the corresponding panels (*a*,*c*,*e*) near a particular aligned phase ($\phi_j = -\pi/2$). It can be seen from the figure that the sum of the orbital drift approximation (C_0) and the fluctuation (C_1) fails to capture the actual variation in C with increasing $Re/\kappa_{eq} = \widetilde{Re}$ (it should be noted that $\kappa_{eq} = \kappa$ in this case). Although breakdown of the orbital drift is expected as soon as $\widetilde{Re}$ becomes of order unity, the actual breakdown only occurs when $\widetilde{Re}$ is substantially larger than 1 (see figure 10*e*,*f*). Therefore, it is necessary to characterize the inertial drift when $\widetilde{Re}$ is of $O(1)$ or larger, and we use a boundary layer analysis to accomplish this in the next subsection.

8.2. *Boundary layer analysis*

In this section, we characterize the inertial drift of a spheroid for $\widetilde{Re}$ of $O(1)$ or larger. We focus on oblate spheroids since it has already been shown that there is a bifurcation in the orientation dynamics for such spheroids that, based on the orbital drift approximation, occurs at increasingly extreme aspect ratios ($\kappa_{eq} \to 0$; the shaded green region in figure 8). In this region, it is important therefore to develop an improved approximation in order to accurately predict the location of the repeller for small but finite Re.

https://doi.org/10.1017/jfm.2018.184 Published online by Cambridge University Press

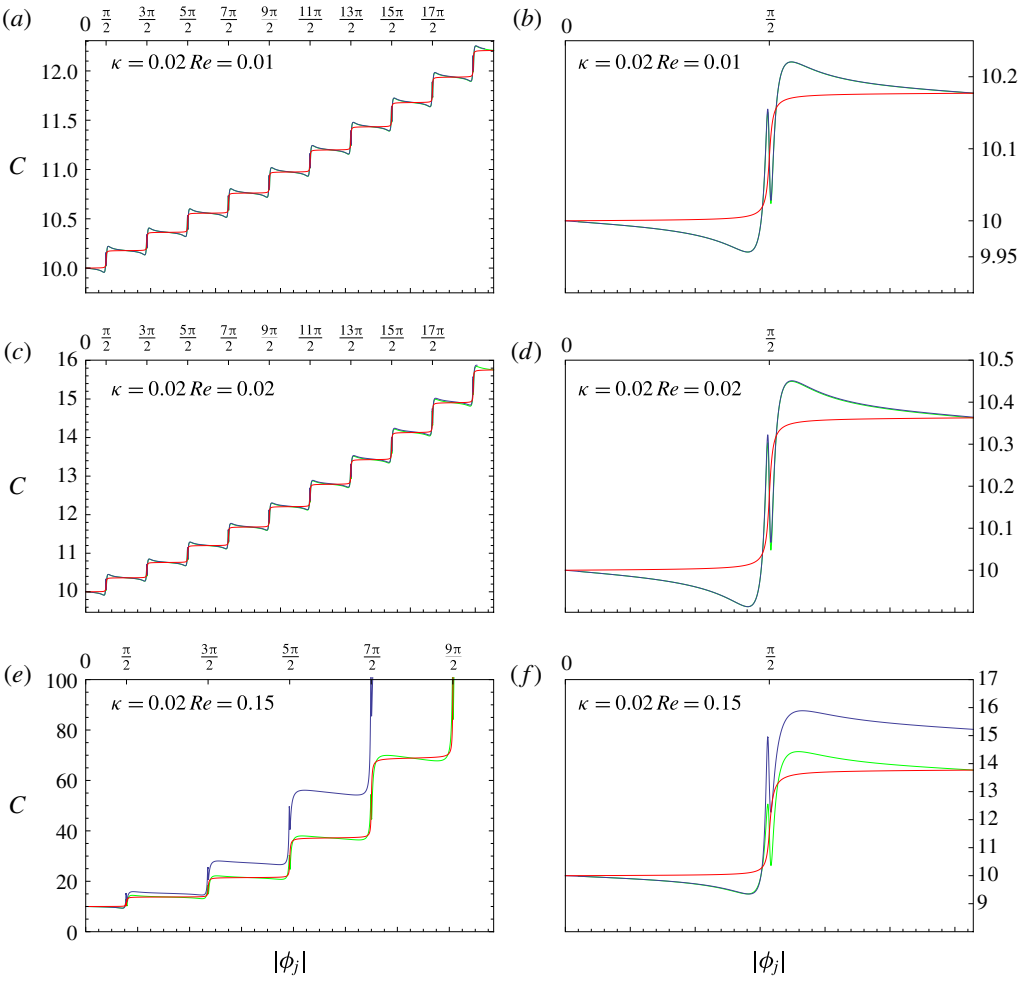


FIGURE 10. (Colour online) The orbital coordinate C as a function of $|\phi_j|$ starting from $C = 10$ and $\phi_j = 0$ for a spheroid with $\kappa = 0.02$ in simple shear flow. The calculation is based on (1) the orbital drift alone obtained by solving (8.3) (red), (2) the orbital drift together with the fluctuations (green) and (3) the C obtained from numerical integration of the governing equations of θ_j and ϕ_j (blue). The results from these three calculations are plotted for various Re values in (*a*), (*c*) and (*e*). Panels (*b*), (*d*) and (*f*) are zoomed views of (*a*), (*c*) and (*e*) respectively near $\phi_j = -\pi/2$.

For an extreme aspect ratio spheroid, the dominant change in C occurs during the aligned phase, and therefore a boundary layer analysis allows one to capture the variation in C for $O(1)$ values of $\widetilde{Re}$ even when the inertial trajectory is not a tight spiral. To see this, one first writes the net change in C as

$$\int_0^{-2\pi} \frac{\mathrm{d}C}{\mathrm{d}\phi_j}\mathrm{d}\phi_j = \int_0^{-2\pi} \frac{\dfrac{\mathrm{d}C}{\mathrm{d}t}}{\dfrac{\mathrm{d}\phi_j}{\mathrm{d}t} + Re\,\dfrac{\mathrm{d}\phi_j}{\mathrm{d}t}|_{Re}}\,\mathrm{d}\phi_j, \tag{8.5}$$

https://doi.org/10.1017/jfm.2018.184 Published online by Cambridge University Press

where $\mathrm{d}\phi_j/\mathrm{d}t$ and $\mathrm{d}C/\mathrm{d}t$ are given in (2.2) and (5.6) respectively and $\mathrm{d}\phi_j/\mathrm{d}t|_{Re}$ in (8.5) is the sum of (5.5) and (6.2). Now, (2.2) can be expressed in terms of κ_{eq} as $\dot{\phi}_j = -(1-\lambda)(\kappa_{eq}^2 \sin^2\phi_j + \cos^2\phi_j)/(\kappa_{eq}^2+1)$, and, in the limit $\kappa_{eq} \to 0$ (an oblate spheroid approaching a flat disk), is proportional to $\cos^2\phi_j$ after neglecting the contribution proportional to $O(\kappa_{eq}^2)$. In this limit, $\mathrm{d}C/\mathrm{d}t$ remains finite and $O(Re)$, so the integrand in (8.5) is proportional to $1/\cos^2\phi_j$ and, therefore, divergent as $1/(\phi_j+\pi/2)$ and $1/(\phi_j+3\pi/2)$ for $\phi_j \to -\pi/2$ and $\phi_j \to -3\pi/2$ respectively. These divergences suggest that the dominant contribution to the integral comes from the aligned phases corresponding to $\phi_j = -\pi/2$ and $-3\pi/2$, as expected from figure 10(*e*). One can therefore rewrite (8.5) as

$$\int_0^{-2\pi} \frac{\mathrm{d}C}{\mathrm{d}\phi_j} d\phi_j = \int_0^{-\pi} \left(\frac{\mathrm{d}C}{\mathrm{d}\phi_j} - \lim_{\phi_j\to-\pi/2}\frac{\mathrm{d}C}{\mathrm{d}\phi_j}\right) \mathrm{d}\phi_j + \int_{-\pi}^{-2\pi} \left(\frac{\mathrm{d}C}{\mathrm{d}\phi_j} - \lim_{\phi_j\to-3\pi/2}\frac{\mathrm{d}C}{\mathrm{d}\phi_j}\right) \mathrm{d}\phi_j + \int_0^{-\pi} \lim_{\phi_j\to-\pi/2}\frac{\mathrm{d}C}{\mathrm{d}\phi_j}\,\mathrm{d}\phi_j + \int_{-\pi}^{-2\pi} \lim_{\phi_j\to-3\pi/2}\frac{\mathrm{d}C}{\mathrm{d}\phi_j}\,\mathrm{d}\phi_j, \tag{8.6}$$

where we have isolated the divergences at $-\pi/2$ and $-3\pi/2$. Using a rescaled coordinate defined as $\hat{\phi} = (\phi_j+\pi/2)/\kappa_{eq}$ and $\hat{\phi} = (\phi_j+3\pi/2)/\kappa_{eq}$ respectively for the third and fourth integrals on the right-hand side above, one can rewrite (8.6) as

$$\int_0^{-2\pi} \frac{\mathrm{d}C}{\mathrm{d}\phi_j}\,\mathrm{d}\phi_j = \int_0^{-\pi} \left(\frac{\mathrm{d}C}{\mathrm{d}\phi_j} - \lim_{\phi_j\to-\pi/2}\frac{\mathrm{d}C}{\mathrm{d}\phi_j}\right) \mathrm{d}\phi_j + \int_{-\pi}^{-2\pi} \left(\frac{\mathrm{d}C}{\mathrm{d}\phi_j} - \lim_{\phi_j\to-3\pi/2}\frac{\mathrm{d}C}{\mathrm{d}\phi_j}\right) \mathrm{d}\phi_j + 2\int_{\pi/2\kappa_{eq}}^{-\pi/2\kappa_{eq}} \frac{\mathrm{d}C}{\mathrm{d}\hat{\phi}}\,\mathrm{d}\hat{\phi}. \tag{8.7}$$

On further rewriting the above equation, one obtains

$$\int_0^{-2\pi} \frac{\mathrm{d}C}{\mathrm{d}\phi_j}\,\mathrm{d}\phi_j = \int_0^{-\pi} \left(\frac{\mathrm{d}C}{\mathrm{d}\phi_j} - \lim_{\phi_j\to-\pi/2}\frac{\mathrm{d}C}{\mathrm{d}\phi_j}\right) \mathrm{d}\phi_j + \int_{-\pi}^{-2\pi} \left(\frac{\mathrm{d}C}{\mathrm{d}\phi_j} - \lim_{\phi_j\to-3\pi/2}\frac{\mathrm{d}C}{\mathrm{d}\phi_j}\right) \mathrm{d}\phi_j + 2\int_{\infty}^{-\infty} \frac{\mathrm{d}C}{\mathrm{d}\hat{\phi}}\,\mathrm{d}\hat{\phi} - 2\int_{\infty}^{\pi/2\kappa_{eq}} \frac{\mathrm{d}C}{\mathrm{d}\hat{\phi}}\,\mathrm{d}\hat{\phi} - 2\int_{-\pi/2\kappa_{eq}}^{-\infty} \frac{\mathrm{d}C}{\mathrm{d}\hat{\phi}}\,\mathrm{d}\hat{\phi}, \tag{8.8}$$

where we have further accounted for the identity of the two aligned-phase integrals. Now, $\mathrm{d}C/\mathrm{d}\hat{\phi}$ is given by

$$\frac{\mathrm{d}C}{\mathrm{d}\hat{\phi}} = \kappa_{eq} \left.\frac{\dfrac{\mathrm{d}C}{\mathrm{d}t}}{\dfrac{\mathrm{d}\phi_j}{\mathrm{d}t} + Re\left.\dfrac{\mathrm{d}\phi_j}{\mathrm{d}t}\right|_{Re}}\right|_{\lim_{\kappa_{eq}\to0}} = \frac{C\widetilde{Re}\,\widetilde{F} - C\widetilde{Re}\,\widetilde{G}\dfrac{\hat{\phi}^2}{1+\hat{\phi}^2}}{-(1+\hat{\phi}^2)(1-\lambda) - \widetilde{Re}\,\widetilde{G}\,\hat{\phi}}, \tag{8.9}$$

where

$$\widetilde{F} = \lim_{\lambda\to1/\kappa^2}\left(F_1^f + F_1^p - F_2^f - F_2^p + (F_3^f + F_3^p + 2(F_5^f + F_5^p))\frac{(1+\hat{\phi}^2-C^2)}{(1+\hat{\phi}^2+C^2)} + F_4^f + F_4^p\right) \tag{8.10}$$

https://doi.org/10.1017/jfm.2018.184 Published online by Cambridge University Press

and

$$\widetilde{G} = \lim_{\lambda \to 1/\kappa^2} \left(G_1^f + G_1^p + (G_2^f + G_2^p - G_4^f - G_4^p) \frac{(1 + \hat{\phi}^2 - C^2)}{(1 + \hat{\phi}^2 + C^2)} - G_3^f - G_3^p \right), \quad (8.11)$$

where the $F^{f(p)}$ and $G^{f(p)}$ terms are defined in appendix B. Noting that in the limit of $\kappa_{eq} \to 0$, $\hat{\phi}$ is large in the last two integrals on the right-hand side of (8.8), one can use (8.9) to write down the integrand of these integrals as

$$\frac{\mathrm{d}C}{\mathrm{d}\hat{\phi}} = \frac{C\widetilde{Re}\widetilde{F} - C\widetilde{Re}\widetilde{G}}{\hat{\phi}^2(\lambda - 1)}, \quad (8.12)$$

which can be solved to obtain $C = \exp(-\widetilde{Re}(\widetilde{F} - \widetilde{G})/\hat{\phi}(\lambda - 1))$. On substituting the aforementioned expression for C in the last two integrals in (8.8), one finds that the sum of these integrals (corresponding to the non-aligned phase) only contributes at $O(\kappa_{eq})$. The first two integrals on the right-hand side of (8.8) are obtained by subtracting the divergent terms associated with them and hence are smaller than the leading-order contribution coming from the third integral. Defining the total change in C at leading order over one rotation as $2\Delta C_{jump}$, one obtains ΔC_{jump},

$$\Delta C_{jump} = \int_{\infty}^{-\infty} \frac{\mathrm{d}C}{\mathrm{d}\hat{\phi}} \, \mathrm{d}\hat{\phi}. \quad (8.13)$$

The jump in C above is obtained by evaluating the integral in (8.13), which is carried out by numerically integrating (8.9) from $\hat{\phi} = \infty$ (a large positive value) to $\hat{\phi} = -\infty$ (a large negative value). This jump is plotted against the rescaled coordinate in figure 11 for a spheroid in a simple shear flow ($Re = 0.15$; $\kappa = 0.02$, $\widetilde{Re} = 7.5$). This jump (green) agrees with the total change in C (blue curve) near the aligned phase, obtained from numerically solving the differential equations for the angular coordinates; in contrast, the orbital drift approximation (red) breaks down for these parameters.

The bifurcation region in the (λ, κ) plane shown in figure 8 was estimated on the basis of the orbital drift approximation. As seen above, the orbital drift need not be a good approximation to the numerics for $O(1)\widetilde{Re}$ or larger. In such cases, one would want to check the actual repeller location with that predicted by the orbital drift approximation. In figure 12, we have shown the shift in the repeller location, as a function of κ, for two values of Re (0.1 and 0.3) in three planar linear flows. The repeller location is the critical C (C^*) at which the orbital drift changes sign. The solid lines are C^* predictions based on numerically integrating the angular velocity of the spheroid at different Re values. The green dots are C^* predictions from the orbital drift approximation. For small $\widetilde{Re}$ ($Re/\kappa_{eq} \ll 1$; note that for a given λ, κ_{eq} increases with increasing κ), it is evident from figure 8 that the C^* prediction based on the orbital drift approximation agrees well with the results of the numerical integration. For larger $\widetilde{Re}$ (for a given λ, large $\widetilde{Re}$ implies $\kappa_{eq} \to 0$ or $\kappa \to \sqrt{\lambda}$), the orbital drift approximation breaks down and the prediction from the numerical integration asymptotes to that from the boundary layer analysis mentioned above (shown as solid circles connected by dashed lines). The maximum $\widetilde{Re}$ corresponding to the smallest aspect ratio in each of the plots in figure 12 is given in the legend. It is clear from figure 12 that the orbital

https://doi.org/10.1017/jfm.2018.184 Published online by Cambridge University Press

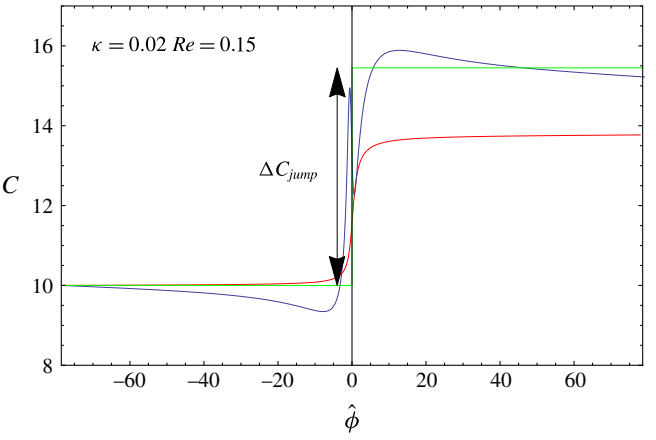


FIGURE 11. (Colour online) The orbital coordinate, during a particular aligned phase, is plotted against the rescaled boundary layer variable for a spheroid of $\kappa = 0.2$ in simple shear flow at $Re = 0.15$. The orbital drift approximation (8.3), the result of numerical integration ((5.6), including both the particle and the fluid inertial contribution) and the prediction from the boundary layer analysis (8.13) are shown in red, blue and green respectively.

drift approximation together with the boundary layer analysis allows one to predict the repeller location with reasonable accuracy down to an $O(1)$ $\widetilde{Re}$.

For a given Re and λ, with decreasing κ, the denominator of the right-hand side of (8.9) becomes zero, and $\mathrm{d}C/\mathrm{d}\hat{\phi}$ diverges at a critical $\hat{\phi}$ below a critical aspect ratio (say κ_{FG}). For oblate spheroids with $\kappa < \kappa_{FG}$, there are fixed points on the flow-gradient plane, and a spheroid starting at $C > C^*(\kappa)$ ceases to rotate and eventually aligns with one of the stable fixed points. As discussed in § 4, in the Stokes limit, the fixed points exist on the flow-gradient plane for an oblate spheroid with $\kappa < \sqrt{\lambda}$. The critical aspect ratio with inertia, κ_{FG}, is greater than $\sqrt{\lambda}$, for all positive λ values. This emergence of fixed points on the flow-gradient plane occurs for prolate spheroids as well, with κ_{FG} being less than the Stokesian value of $1/\sqrt{\lambda}$; prolate spheroids with κ greater than this value experience an arrest of rotation. It should be noted that for a slender fibre in simple shear flow, Subramanian & Koch (2005) have already pointed out that fluid inertia arrests the rotation at a critical aspect ratio. For the (λ, Re) combinations in figure 12, the values of $\kappa_{FG}(\lambda, Re)$ are given by $\kappa_{FG}(0, 0.1) = 0.01$, $\kappa_{FG}(0, 0.3) = 0.02$, $\kappa_{FG}(0.00009, 0.1) = 0.0137$, $\kappa_{FG}(0.00009, 0.3) = 0.031$, $\kappa_{FG}(0.0025, 0.1) = 0.051$ and $\kappa_{FG}(0.0025, 0.3) = 0.058$. Finally, it is worth mentioning that there is a rather complicated sequence of bifurcations within an $O(Re^2)$ neighbourhood of the critical curve (for both prolate and oblate spheroids), and the resulting transitions in orientation dynamics cannot be captured within a one-dimensional orbit-constant-based interpretation. This will be reported in detail in a future article.

9. Effect of Brownian motion: the tumbling–spinning phase diagrams

In previous sections, it was shown that the combined effect of fluid and particle inertia uniquely determines the long-time orientation dynamics of a neutrally buoyant spheroid for a majority of (λ, κ) pairs below the λ_{crit} curve (see figure 8). For (λ, κ)

https://doi.org/10.1017/jfm.2018.184 Published online by Cambridge University Press

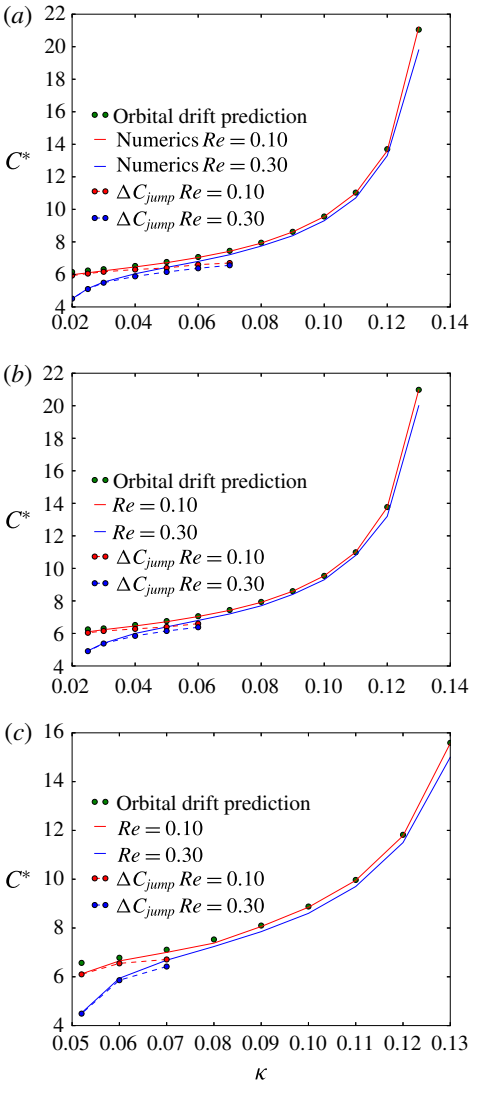


FIGURE 12. (Colour online) The repeller location C^* is plotted against the aspect ratio for two values of Re ($Re = 0.1$ and 0.3) for hyperbolic planar linear flows with (*a*) $\lambda = 0$, (*b*) $\lambda = 0.00009$ and (*c*) $\lambda = 0.0025$. The maximum $\widetilde{Re}$ in each of the cases is (*a*) 15, (*b*) 12.97 and (*c*) 21.04.

pairs corresponding to the shaded region immediately below the λ_{crit} curve, however, the final spheroid orientation is not unique. As first argued by Dabade *et al.* (2016) and Marath *et al.* (2017) in the context of simple shear, one needs a stochastic orientational decorrelation mechanism, either hydrodynamic or non-hydrodynamic, for a unique orientation distribution in this region. For simple shear flow ($\lambda = 0$), the absence of a unique steady state in the deterministic limit occurs for aspect ratios less than 0.14. In Dabade *et al.* (2016), for this case, weak rotary Brownian motion (thermal orientation fluctuations) was considered as a canonical example of such an orientation decorrelation mechanism, and the unique distribution stabilized by the

https://doi.org/10.1017/jfm.2018.184 Published online by Cambridge University Press

combined effect of inertia and Brownian motion was determined. Interestingly, as shown by Marath *et al.* (2017), the one-dimensional reduced description in terms of the orbit constant alone, which results from the orbital drift interpretation, implies that the unique steady-state distribution must be of the Boltzmann form. The potential in the Boltzmann exponential may then be used to provide a 'thermodynamic' interpretation of the spheroid orientation dynamics in the presence of both inertia and Brownian motion. Interestingly, this leads to the identification of a tumbling–spinning coexistence envelope in C–κ–$Re\,Pe_r$ space, where one expects hysteretic dynamics starting from a general initial orientation distribution; one of the signatures of this hysteresis is a multivalued viscosity at a given shear rate.

As explained by Marath *et al.* (2017), the aforementioned hysteresis associated with the tumbling–spinning transition is analogous to that associated with the well-known coil–stretch transition (De Gennes 1974; Hinch 1974) of high-molecular-weight polymers in an extensional flow. In the latter case, one expects the coexistence of polymer molecules in the coiled and stretched states over an intermediate range of Deborah numbers ($De = \dot{\gamma}\tau_v$, where τ_v is the intrinsic relaxation time scale of the underlying microstructure). The coil–stretch hysteresis has since been confirmed in single-molecule experiments (Schroeder *et al.* 2003; Shaqfeh 2005). Apart from interpreting the coil–stretch transition as a first-order transition in a reduced configuration space, involving only the mean polymer extension as the coarse-grained variable, De Gennes also predicted that the transition would progressively 'soften' with the addition of vorticity, and the sharp distinction between the coiled and stretched states would eventually vanish for simple shear flow. Following the original experiment that verified the sharp transition that occurs in planar extension (Schroeder *et al.* 2003), there have been a large number of experimental and numerical studies, primarily by Shaqfeh and coworkers, with the aim of understanding the dynamics of polymer molecules in planar linear flows with differing amounts of extension and vorticity (Babcock *et al.* 2003; Schroeder *et al.* 2005; Shaqfeh 2005; Hoffman & Shaqfeh 2007; Lee *et al.* 2007*b*); these studies have helped to confirm De Genne's original predictions. For spheroidal suspensions, as mentioned above, Dabade *et al.* (2016) and Marath *et al.* (2017) provided an interpretation of the orientation dynamics analogous to the polymeric case, and identified a first-order transition between the tumbling (large-C) and spinning (small-C) states for an inertial spheroid in simple shear flow. In this section, along lines similar to those of Shaqfeh and coworkers above, we examine the effect of an added extension or vorticity (corresponding to non-zero λ values) on the tumbling–spinning transition in simple shear flow ($\lambda = 0$). It is thereby shown that the coexistence region rapidly shrinks in extent on either side of simple shear.

With the addition of rotary Brownian motion, the spheroid orientation vector, $\boldsymbol{p}$, becomes a random variable, and the orientation distribution, $\Omega(\boldsymbol{p}, t)$, is then governed by a convection–diffusion equation, given by

$$\frac{\partial \Omega}{\partial t} + \nabla_{\boldsymbol{p}} \cdot [(\dot{\boldsymbol{p}}_{jeff} + Re\,\dot{\boldsymbol{p}}_i)\Omega] = \frac{1}{Pe_r}\nabla_{\boldsymbol{p}}^2 \Omega. \tag{9.1}$$

In (9.1), Pe_r is the rotary Péclet number, defined as $Pe_r = \dot{\gamma}/D_r$, where D_r is the rotary diffusivity. The term on the right-hand side of (9.1) captures the effect of Brownian motion on the orientation distribution. The convection term on the left-hand side is made up of two contributions. The first one is the convection due to the angular velocity at leading order, denoted by $\dot{\boldsymbol{p}}_{jeff}$ ($\boldsymbol{\Omega}_{jeff} \wedge \boldsymbol{p}$), and the second is the convection

https://doi.org/10.1017/jfm.2018.184 Published online by Cambridge University Press

due to the inertial correction for a neutrally buoyant spheroid ($Re = St$), denoted by $\dot{\boldsymbol{p}}_i$. In Einarsson *et al.* (2014), an equation similar to (9.1) was solved numerically to understand the combined effects of particle inertia and rotary Brownian motion on the orientation distribution of a spheroid in a simple shear flow. In simple shear flow, the orientation distribution set up by particle inertia alone does not change much due to weak diffusion. However, for neutrally buoyant spheroids, as shown by Dabade *et al.* (2016), even weak diffusion, acting over a long period of time, will lead to a large change in the distribution for spheroids in the range of aspect ratios ($0 < \kappa < 0.14$ for simple shear) where inertia alone leads to a bistable scenario. This large change in distribution would be manifested as an $O(1)$ change in the intrinsic viscosity of a dilute suspension of such spheroids.

In orbital coordinates, $\dot{\boldsymbol{p}}_{jeff}$ takes the form $h_\tau(1-\lambda)\kappa_{eq}/(\kappa_{eq}^2+1)\ \hat{\boldsymbol{\tau}}$, where $\hat{\boldsymbol{\tau}}$ is the unit vector tangent to a Jeffery orbit (for a given C) and h_τ is the metric factor corresponding to the τ coordinate (see appendix D). The convection due to the inertial correction $\dot{\boldsymbol{p}}_i$ takes the form $u_{iC}\hat{\boldsymbol{C}} + u_{i\tau}\hat{\boldsymbol{\tau}}$, where $\hat{\boldsymbol{C}}$ is the same as $\hat{\boldsymbol{\theta}}_j$ (see appendix D); the term proportional to $\hat{\boldsymbol{C}}$ is responsible for the drift across orbits. There are two time scales in the drift–diffusion problem as governed by (9.1). These are the fast time scale over which the distribution is convected by $\dot{\boldsymbol{p}}_{jeff}$, and the slow time scale over which the inertial drift and the Brownian motion affect the orientation distribution along a coordinate 'orthogonal' to the Stokesian convection. The convection–diffusion equation in (9.1) can be solved approximately, in the limit $Re \ll 1$, $Pe_r \gg 1$ ($Re\,Pe_r$ being arbitrary), the limit implying that the two time scales above are disparate. Defining the fast and slow time scales as $t_1 = t$ and $t_2 = Re\,t$, we use the ansatz $\Omega(C, \tau, t_1, t_2) = f(C, t_2)g(C, \tau, t_1)$ to solve (9.1), where f and g are the distributions across and along the Jeffery orbits respectively (Dabade *et al.* 2016; Marath *et al.* 2017).

It turns out that $\dot{\boldsymbol{p}}_{jeff}$ in (9.1) rapidly sets up the steady distribution along the Jeffery orbits in the presence of a tiny polydispersity in the aspect ratio on a diffusive time scale, with the diffusivity being proportional to the variance of the aspect ratio distribution (the strictly monodisperse limit leads to an indeterminacy even for the evolution along an orbit; see Okagawa, Cox & Mason (1973), Ennis, Okagawa & Mason (1978), Ivanov, Van de Ven & Mason (1982) and Marath *et al.* (2017)). The steady-state distribution of phase angles takes the form $g(C, \tau) = 1/(h_c h_\tau \sin\alpha)$, where h_C is the metric factor of the C coordinate and α is the angle between the unit vectors $\hat{\boldsymbol{C}}$ and $\hat{\boldsymbol{\tau}}$ (see appendix D); on this time scale, the distribution across orbits remains unaltered from its initial form.

Over much longer times, the inertial drift and Brownian couples set up the distribution across Jeffery orbits, and it can be shown that (Marath *et al.* 2017) the equation governing $f(C, t_2)$ is

$$\frac{\partial f}{\partial t_2} + \frac{1}{Re}\frac{\partial}{\partial C}\left[\left(Re\,\Delta C_i - \frac{\chi_2}{2Pe_r C}\right)f\right] = \frac{1}{Re\,Pe_r}\frac{\partial}{\partial C}\left(\frac{\chi_1}{2}\frac{\partial f}{\partial C}\right), \tag{9.2}$$

where

$$\left.\begin{aligned}\chi_1(C;\kappa_{eq}) &= \left(\frac{\kappa_{eq}^2+1}{\kappa_{eq}^2} + C^2\left(\frac{7}{2} + \frac{1}{4\kappa_{eq}^2} + \frac{\kappa_{eq}^2}{4}\right) + C^4(\kappa_{eq}^2+1)\right),\\ \chi_2 &= \left(-\frac{\kappa_{eq}^2+1}{\kappa_{eq}^2} + C^2\left(6 - \left(\frac{7}{2} + \frac{1}{4\kappa_{eq}^2} + \frac{\kappa_{eq}^2}{4}\right)\right) + 2C^4(\kappa_{eq}^2+1)\right)\end{aligned}\right\} \tag{9.3}$$

https://doi.org/10.1017/jfm.2018.184 Published online by Cambridge University Press

and $\Delta C_i = (\Delta C_p + \Delta C_f)\kappa_{eq}/(\kappa_{eq}^2 + 1)$, with ΔC_p and ΔC_f being given in (5.10) and (6.3). The steady-state solution of (9.2) takes the form

$$f_s(C) = N \exp\left[-Re\,Pe_r \int^C \left(\frac{\chi_2}{Re\,Pe_r C'} - 2\Delta C_i(C';\kappa)}{\chi_1}\right) \mathrm{d}C'\right], \tag{9.4}$$

where N is the normalization constant. For (λ, κ) in the shaded region in figure 8, in the absence of Brownian motion, $f_s(C)$ would be a singular distribution consisting of two delta functions, of the form $\mathcal{A}_1\delta(C) + \mathcal{A}_2\delta(1/C)$, with $\mathcal{A}_1$ and $\mathcal{A}_2$ being the fractions of initial spheroid orientations on the either side of the repeller on the unit hemisphere. The functional form of the distribution reflects the fact that inertia alone stabilizes the spinning and tumbling orbits for times long compared with $O(Re\dot{\gamma}^{-1})$. The coefficients of the aforementioned delta functions are, however, still determined by the particular initial distribution (in the Stokes limit, even the functional form of the distribution is indeterminate). For finite $Re\,Pe_r$, Brownian motion sets up a unique steady-state distribution given by (9.4). In the limit $Re\,Pe_r \to \infty$, (9.4) has the same structure as the aforementioned singular distribution involving delta functions, but with the ratio $\mathcal{A}_1/\mathcal{A}_2$ being independent of the initial distribution. This is because weak Brownian motion allows for an exchange of probability between the peaks of the initial-condition-dependent bimodal distribution that results for large $Re\,Pe_r$. The exchange occurs via a slow barrier-hopping process across a potential barrier set up by the bidirectional inertial drift. The presence of a slow (for $Re\,Pe_r \to \infty$) thermally driven barrier-hopping process also leads to long-lived metastable states that depend on the initial orientation distribution.

It is of interest to note that the steady-state distribution across the Jeffery orbits is of the Boltzmann form. In (9.4), the factor $1/Re\,Pe_r$ in the exponent therefore plays the role of the temperature, and the function that multiples $1/Re\,Pe_r$ can be interpreted as a potential $U(C, Re\,Pe_r, \kappa, \lambda)$. The steady-state distribution peaks at the minima of this potential, and these peaks can therefore be interpreted as phases. This is analogous to defining the liquid and gas phases as the minima of the Gibbs free energy in the case of a one-component system in thermodynamics. As pointed out by Marath *et al.* (2017), in the specific context of simple shear, a closer analogy exists with respect to the well-known coil–stretch transition in the polymer physics literature (De Gennes 1974; Hinch 1974). In general, for a given λ and $Re\,Pe_r$ (above a critical value), with increasing aspect ratio, the nature of the potential changes from a single-well structure peaked close to tumbling ($C = \infty$), to a double-well structure, and eventually again to a single-well structure peaked close to spinning ($C = 0$). To illustrate this transition, we have plotted the potential for $\lambda = 0.00009$, $Re\,Pe_r = 70\,000$, and for various aspect ratios, in figure 13(*a*). The potential changes as described above, with both wells having the same depth at an aspect ratio of 0.021. The extrema of the potential (indicated by coloured circular dots) for various aspect ratios, given in figure 13(*a*), are tracked in figure 13(*b*). The curve connecting the extrema for $Re\,Pe_r = 70000$ is shown there. In analogy to a thermodynamic tie line, a horizontal dashed line is drawn at $\kappa = 0.021$, for which the two potential minima have the same magnitude. The small-C and large-C minima that it connects may be identified respectively with 'spinning' and 'tumbling' phases that coexist at the particular κ, λ and $Re\,Pe_r$. One can define an isotherm consisting of three curves in figure 13(*b*). The first is the monotonically decreasing part of the curve of extrema, starting from the largest aspect ratio in figure 13(*b*) and ending at the left of the

https://doi.org/10.1017/jfm.2018.184 Published online by Cambridge University Press

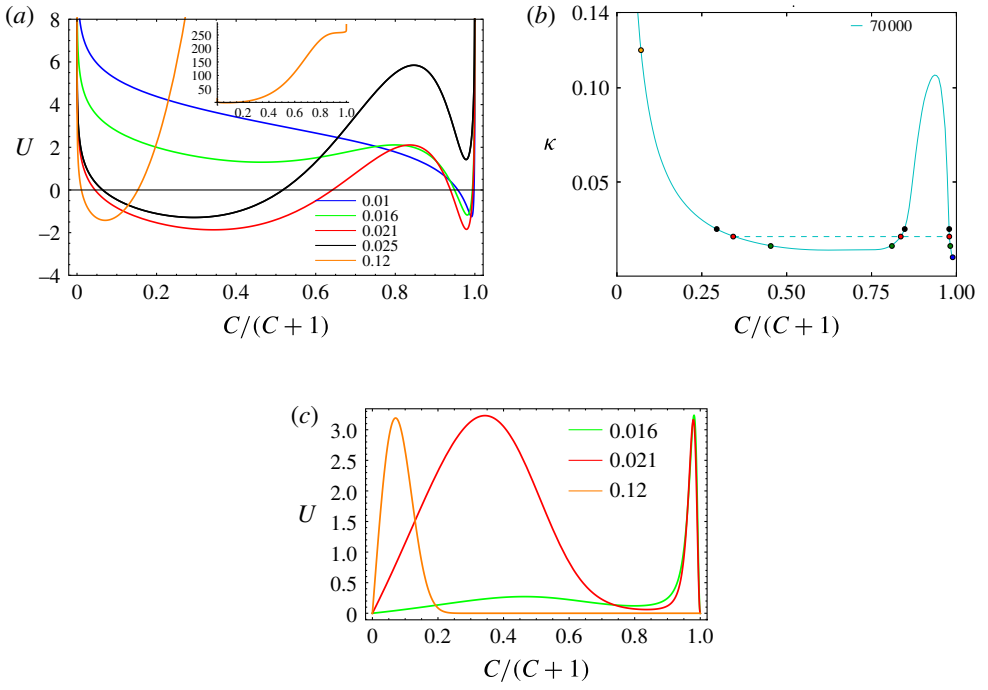


FIGURE 13. (Colour online) (*a*) The potential at a $Re\,Pe_r$ of 70 000 is plotted against $C/(C+1)$ for spheroids of various aspect ratios in a planar linear flow with $\lambda = 0.00009$; the inset shows the complete potential for $\kappa = 0.12$. (*b*) The curve of extrema for a $Re\,Pe_r$ of 70 000. The circular dots represent the extrema of the potential plotted in (*a*). (*c*) The steady-state orientation distribution at a $Re\,Pe_r$ of 70 000 for three aspect ratios ($\kappa = 0.016, 0.021, 0.12$).

tie line; the second is the tie line itself; the third starts from the right end of the tie line and continues down to lower aspect ratios along the curve of extrema. Any point on this isotherm outside of the tie line corresponds to the C at which the steady-state orientation distribution would peak for a given $Re\,Pe_r$ and κ. To illustrate this, in figure 13(*c*), we have plotted the steady-state orientation distribution for three different aspect ratios. The steady-state distribution is bimodal and both peaks have the same amplitude for a tie-line aspect ratio of 0.021. For $\kappa = 0.12$, the distribution is unimodal (since the potential only has a single minimum at $C = 0.076$), while for $\kappa = 0.016$, the distribution is peaked at the deeper minimum of the corresponding potential ($C = 51.68$).

One can repeat the above exercise for various $Re\,Pe_r$ values to develop a 'phase diagram', as shown in figure 14(*a*) for $\lambda = 0.0009$. The constant $Re\,Pe_r$ loci in figure 14(*a*) may again be regarded as isotherms. The tie lines now replace the intermediate non-monotonic portion in figure 14(*a*), resulting in a two-phase (tumbling–spinning) envelope that ends in a critical point, (κ, C, $Re\,Pe_r$, λ) $\equiv$ (0.0665, 2.31, 1200, 0.00009), as shown in figure 14(*b*). Such a phase diagram, emphasizing a 'thermodynamic' interpretation of the orientation dynamics, has already been developed for the specific case of simple shear flow ($\lambda = 0$) by Marath *et al.* (2017). The isotherm corresponding to $Re\,Pe_r = \infty$ in figure 14(*b*) is defined as a piecewise linear curve made up of three segments, defined as (1)

https://doi.org/10.1017/jfm.2018.184 Published online by Cambridge University Press

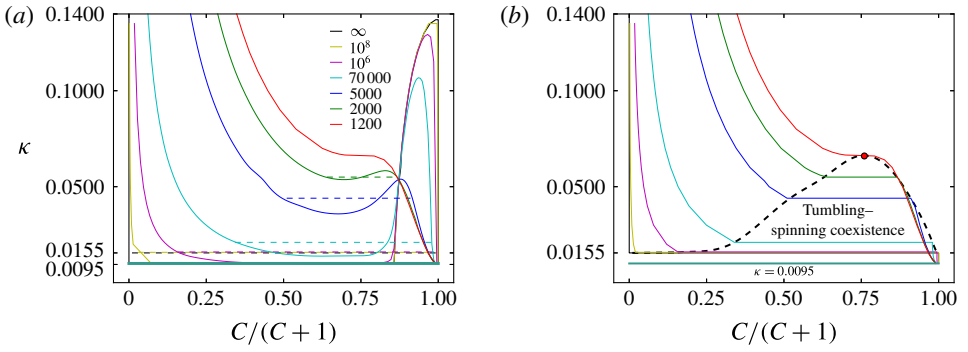


FIGURE 14. (Colour online) (*a*) The curves of extrema corresponding to different values of $Re\,Pe_r$. (*b*) The envelope joining the tie lines for the phase diagram in (*a*). The red circular dot corresponds to the critical point $(\kappa,\ C,\ Re\,Pe_r,\ \lambda) \equiv (0.0665, 2.31, 1200, 0.00009)$; the phase diagram is cut off at $\kappa = \sqrt{\lambda} = 0.0095$.

$C = 0$, when $\kappa > 0.0155$, (2) $\kappa = 0.0155$, when $0 < C < \infty$, and (3) $C = \infty$, when $0.0094 < \kappa < 0.0155$. Therefore, in the limit of $Re\,Pe_r \to \infty$, the orientation distribution discontinuously changes from a delta function localized at the spinning orbit above $\kappa = 0.0155$ to one localized at the tumbling orbit below $\kappa = 0.0155$ (this discontinuous change in the steady-state distribution nevertheless requires an infinite amount of time in the limit $Re\,Pe_r \to \infty$; see the discussion below). The phase diagram is cut off (below) at an aspect ratio of $\kappa = \sqrt{0.00009} = 0.0095$, plotted as the lowest horizontal line in figure 14(*b*), since for smaller aspect ratios, the Stokesian trajectories are not closed and the interpretation based on averaging over Jeffery orbits breaks down. For simple shear flow ($\lambda = 0$) analysed by Marath *et al.* (2017), the phase diagram extends down to $\kappa = 0$, with the discontinuous transition occurring at an aspect ratio of 0.0126 in the limit of $Re\,Pe_r \to \infty$.

The phase diagrams for a range of planar linear flows in the neighbourhood of simple shear are plotted in figure 15. Those for positive λ values are bounded below by $\kappa = \sqrt{\lambda}$, the smallest aspect ratio at which the orbits of the spheroid are closed in the Stokes limit. It should be noted that with increasing λ (positive), the lower bound of the phase diagram, defined by $\kappa = \sqrt{\lambda}$, moves upward. The largest aspect ratio at which the potential is bistable, for a given $Re\,Pe_r$, also increases with increasing λ (positive). The lower bound, however, increases at a faster rate, and the net result is that the region corresponding to a bistable potential shrinks for positive λ, vanishing at a λ value of approximately 0.2. Above this particular λ, irrespective of $Re\,Pe_r$ and κ ($>\sqrt{\lambda}$), the potential only has a single minimum. The region of coexistence defined by the tie lines as seen in figure 14(*b*) also disappears at a λ value of approximately 0.2. It should be noted that a region of coexistence implies that there should be an aspect ratio at which the potential has two minima of equal depth, and therefore is found over a narrower range of parameters than that corresponding to a potential that is bistable. The critical aspect ratio at which the discontinuous transition from spinning to tumbling spheroids occurs (for $Re\,Pe_r \to \infty$) also increases with increasing λ. However, the rate of increase is again smaller than that of the lower bound ($\kappa = \sqrt{\lambda}$). This discontinuous transition, therefore, ceases to exist for λ values greater than 0.042. In other words, for $\lambda > 0.042$, the final steady-state distribution in the limit $Re\,Pe_r \to \infty$ would be a delta function localized at the spinning orbit. Thus,

https://doi.org/10.1017/jfm.2018.184 Published online by Cambridge University Press

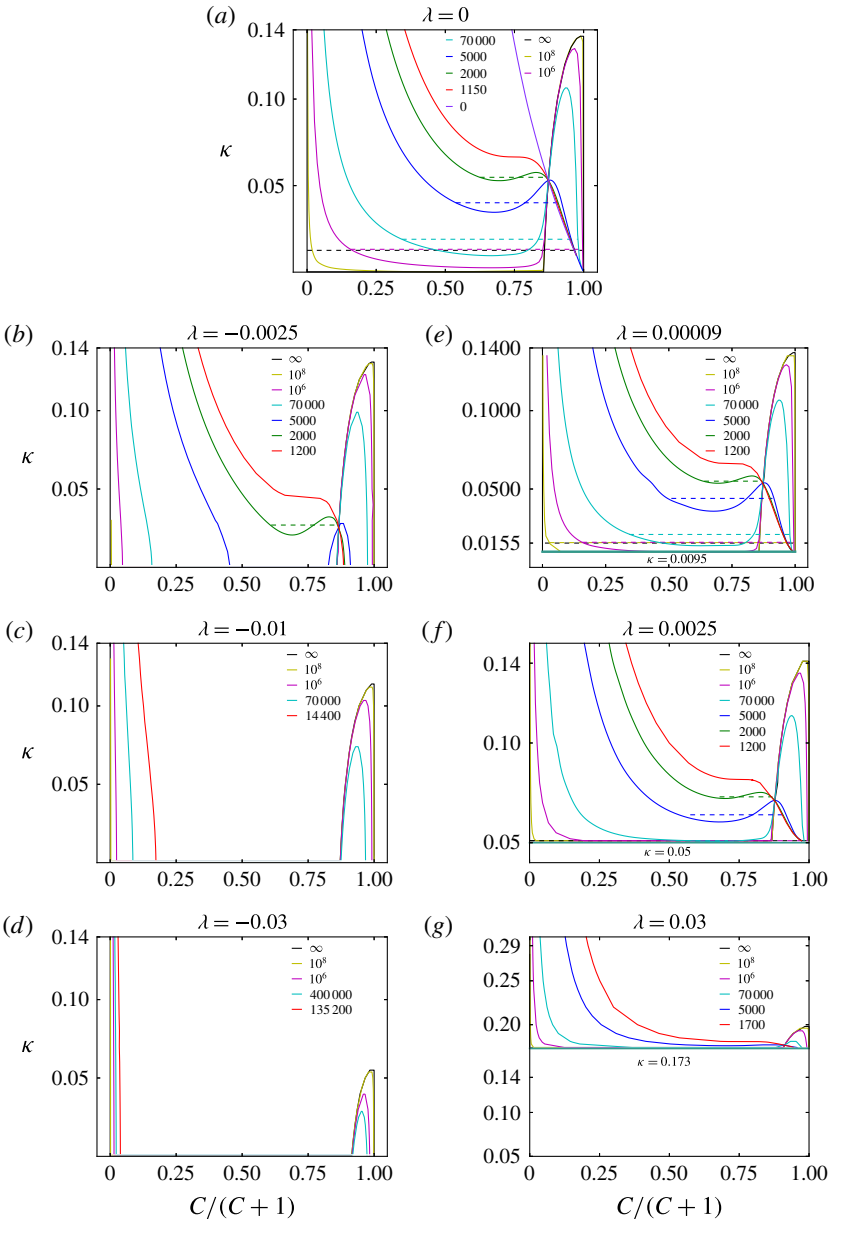


FIGURE 15. (Colour online) The tumbling–spinning phase diagrams for various values of λ. Panel (*a*), showing $\lambda = 0$ for simple shear flow is reproduced from Marath *et al.* (2017). Panels (*b–d*) correspond to negative values of λ and panels (*e–g*) correspond to positive values of λ. The phase diagrams in (*e–g*) are cut off at (*e*) $\kappa = 0.0095$, (*f*) $\kappa = 0.05$ and (*g*) $\kappa = 0.173$.

for $0.042 < \lambda < 0.2$, the steady-state distribution in the limit $Re\,Pe_r \to \infty$ (weakly Brownian limit) is different from the deterministic limit (no Brownian motion), the distribution corresponding to the latter being two delta functions, with one peaked

https://doi.org/10.1017/jfm.2018.184 Published online by Cambridge University Press

at the spinning orbit and the other at the tumbling orbit, and the coefficients of the delta functions being determined by the initial orientation distribution.

When λ is negative, the aspect ratio bounding the bistable region from above (for a given $Re\,Pe_r$) decreases with decreasing λ, but the lower threshold remains at $\kappa = 0$ (the Stokesian trajectories are always closed for $\lambda < 0$ regardless of aspect ratio). Therefore, the region with bistable potential shrinks for negative λ and disappears earlier at a λ of approximately -0.043. The region of coexistence disappears earlier at a λ of approximately -0.005. The discontinuous transition (in the limit $Re\,Pe_r \to \infty$) mentioned above ceases to exist below a λ of approximately -0.0002.

The coexistence region in the simple shear flow case (Marath *et al.* 2017) rapidly shrinks on either side with increasing $|\lambda|$. In the limit $Re\,Pe_r \to \infty$, the discontinuous transition from spinning to tumbling occurs only for λ ranging from -0.0002 to 0.042, at a λ-dependent aspect ratio. As mentioned earlier, such a transition for simple shear flow occurs at an aspect ratio of 0.0126 (Dabade *et al.* 2016). For λ outside the aforementioned range, the long-time distribution is a delta function localized at the spinning orbit.

Although we have focused on the steady-state orientation distribution above, for large $Re\,Pe_r$, one might have to wait for an exceedingly long time to see the development of the steady state, especially in regions of parameter space where it is bimodal. This is because when the potential is bistable, the two minima are separated by a barrier at an intermediate maximum (see figure 13*a*), and the eventual evolution to the steady state would depend on a slow barrier-hopping process driven by weak thermal fluctuations. An estimate of this time can be made using the Kramers reaction rate theory (Chandrasekhar 1943), and the time scale is given by $(4\pi\, Re\, Pe_r/\chi_1|_{C_{max}}(f''|_{C_{max}} f''|_{C_{min}})^{1/2})\mathrm{e}^{Re\,Pe_r \Delta U}$, where ΔU is the magnitude of the difference in the potential between the lowest minimum (C_{min}) and the intermediate maximum (C_{max}) of the bistable potential (Marath *et al.* 2017). The time scale for barrier hopping is thus proportional to the exponential of $Re\,Pe_r$, which can be very large for most of the $Re\,Pe_r$ values in figure 15. Depending on the initial conditions, the orientation distribution of the spheroid might therefore evolve rapidly to an initial-condition-dependent quasiequilibrium (a metastable state), and the subsequent evolution to the time steady state may not occur over the duration of an experiment. The existence of such metastable distributions is therefore expected to result in a hysteresis characterizing the transition between tumbling and spinning modes. As mentioned above, the range of κ for which such a bistable potential exist shrinks with increasing $|\lambda|$, and the hysteresis is therefore most relevant to flows in the immediate neighbourhood of simple shear. An increase in the extension–vorticity imbalance, at a fixed aspect ratio, should, in principle, lead to an aspect-ratio-dependent critical flow at which the coexistence region shrinks to a point (much like simple shear flow for the coil–stretch transition; see Shaqfeh 2005). The phase diagrams suggest that such a scenario is realized for a very small excess of vorticity ($\lambda < 0$). The scenario on the hyperbolic side (excess extension, $\lambda > 0$) is more complex since the tumbling–spinning coexistence can only exist until $\lambda = \kappa^2$, and the truncation of the coexistence region due to the upward movement of this line may therefore precede the appearance of a critical point (at a fixed aspect ratio).

10. Conclusions and future work

In this paper, we have analysed the effect of particle and fluid inertia on the orientation dynamics of a spheroid in a planar linear flow. The $O(St)$ correction to the leading-order angular velocity of a spheroid has already been derived by Einarsson *et al.* (2014), but the analysis was restricted to simple shear flow ($\lambda = 0$).

https://doi.org/10.1017/jfm.2018.184 Published online by Cambridge University Press

With the aim of understanding the effect of particle inertia in flows with non-zero λ values, the $O(St)$ corrections are rederived in § 5 and are given in (5.4) and (5.5). The corrections, at $O(Re)$, arising from fluid inertia are given in (6.1) and (6.2). We have used an orbital drift approximation to analyse the solution of the differential equations governing the angular coordinates, the orbital drift being defined as a change in the orbit constant, given in (4.2), per Jeffery time period. The orbital drifts for the particle and fluid inertia cases are given in (5.10) and (6.3) respectively. The orbits stabilized by particle and fluid inertia are identified in the λ–κ plane in figures 4 and 5 and figures 6 and 7 respectively. The shaded regions in these figures correspond to the (λ, κ) combinations for which there is a repeller on the unit hemisphere that divides the orientation space into two basins of attraction, with the attractors being the tumbling and spinning orbits respectively. Typical examples of repellers are shown in figure 4(*d–f*). The orbits stabilized by inertia for the important case of neutrally buoyant spheroids are identified in figure 8. For the neutrally buoyant case, the bifurcation leading to both tumbling and spinning orbits as possible steady states exists only for oblate spheroids with aspect ratios less than a λ-dependent threshold that has a maximum value of 0.323 for a planar linear flow with $\lambda = 0.104$. For all inertial scenarios, other than the neutrally buoyant case, the spheroid, in addition to convecting with the ambient shear flow, will also sediment relative to it due to gravity. The role of the sedimentation-induced torque, analysed in the quiescent scenario by Dabade *et al.* (2015), is neglected here. An analysis of the orientation dynamics under the combined effects of an ambient shear and gravity will be reported separately (Marath & Subramanian 2017).

In recent efforts, Rosen, Lundell & Aidun (2014) and Rosen *et al.* (2015*a*) numerically examined the effects of both particle and fluid inertia on a force-free spheroid in a simple shear flow, and attributed the drift of a weakly inertial prolate spheroid towards the tumbling orbit to the effects of particle inertia. For a prolate spheroid of aspect ratio 4, for example, fluid inertia is thought to play a role only beyond a critical Re at which a bifurcation renders both the tumbling and the log-rolling states stable. This conclusion is incorrect, and is likely to be motivated by some of the earliest efforts which erroneously concluded that the fluid inertial effects stabilize the spinning orbit (Taylor 1923; Saffman 1956; Karnis, Goldsmith & Mason 1963). Our earlier work on simple shear flow has already shown that fluid inertia is dominant for small Re, and for $O(1)$ values of the ratio St/Re. Further, numerical simulations at a Re of $O(1)$ (Rosen *et al.* 2015*b*) were shown to be qualitatively in agreement with analytical predictions for small Re (Einarsson *et al.* 2015; Dabade *et al.* 2016). Thus, one expects fluid inertia to continue to dominate particle inertia for $O(1)$ Re values at least up to the aforementioned bifurcation value. The present effort shows that the fluid inertia continues to remain dominant for hyperbolic planar linear flows, and for elliptic linear flows in the vicinity of simple shear. As shown in § 7 for neutrally buoyant spheroids, the bifurcation region for oblate spheroids is virtually unchanged in form relative to its estimate for $St = 0$ in § 6. For λ values closer to solid-body rotation, however, the drift due to particle inertia is dominant (notwithstanding the centrifugal buoyancy contribution).

In § 9, an orientation decorrelation mechanism in the form of rotary Brownian motion was included in the analysis in order to eliminate the aforementioned possibility of multiple steady states. The steady-state orientation distribution under the combined effect of Brownian motion and inertia lends itself to an elegant thermodynamic interpretation in C–κ–$Re\,Pe_r$ space. The transition of the distribution from a unimodal to a bimodal one has similarities to a phase transition, and the

https://doi.org/10.1017/jfm.2018.184 Published online by Cambridge University Press

small- and large-C minima of the bimodal distribution are identified with spinning and tumbling phases. The tumbling–spinning coexistence region in the C–κ–$Re\,Pe_r$ space is identified, and it is shown that this region shrinks rapidly with increasing $|\lambda|$. That is to say, the coexistence region is maximum in extent for simple shear, and diminishes rapidly for planar linear flows on either side of simple shear (with increasing extension or vorticity). The orientation dynamics in the coexistence region is expected to have a strong hysteretic signature, with initial-condition-dependent metastable states likely to be seen in real experiments. The transition from the metastable states to the final steady states through a barrier-hopping process, when driven by thermal fluctuations alone, may take an exceedingly long time.

Any mechanism that leads to stochastic orientation fluctuations could play a role similar to rotary Brownian motion, and thereby give rise to interesting non-equilibrium transitions between different orientational states, and hysteretic dynamics. An example of this is athermal fluctuations driven by hydrodynamic interactions (Dabade *et al.* 2016). They differ in character from thermal orientation fluctuations in that the decorrelation is driven by large jumps in orientation triggered by pair encounters rather than a succession of small-amplitude jumps that characterize a rotary diffusion process. The governing integro-differential equation can be formally written down (as has been done in Marath *et al.* (2017)), although lack of any detailed knowledge about the kernel related to pair hydrodynamic interaction renders a solely theoretical resolution impossible. Experimentally, this route might nevertheless be the easier one in terms of using the volume fraction as a parameter to tune the barrier-hopping times to values that are accessible in real experiments.

The bidirectional drift, and the resulting dependence of the final state on initial orientation, may also arise due to other sources of nonlinearity such as viscoelasticity. An experiment (Petrich *et al.* 2000) investigating the behaviour of non-Brownian fibres suspended in an elastic fluid, under oscillatory shear, has, in fact, already demonstrated the existence of multiple steady states for the fibre orientation. At moderate strain and an $O(1)$ Deborah number (a non-dimensional number characterizing the effect of viscoelasticity given by the product of an ambient shear rate and the microstructural relaxation time), the authors find that the flow as well as the vorticity directions act as stable fixed points, and at long times, a fibre, depending on its initial orientation, will be aligned with either of the two directions (Petrich *et al.* 2000). Further, a recent numerical simulation (d'Avino *et al.* 2014) has reported that the steady-state orientation of a non-Brownian prolate spheroid of aspect ratio 4 suspended in a viscoelastic fluid, when subjected to a simple shear flow, is not unique; it is again determined by the initial orientation of the spheroid. If the fibres (or the spheroid in the simulation) were Brownian, or if the fibre (spheroid) concentration were large enough for hydrodynamic interactions to drive orientation fluctuations, a unique steady-state partitioning between the different orientation states could be achieved. One can, in principle, tune the strength of the Brownian motion independent of the viscoelasticity by altering the size of the spheroid, and, from the experimental viewpoint, it may therefore be easier to demonstrate the existence of non-equilibrium orientational order transitions found here, and in Marath *et al.* (2017), under the combined effect of viscoelasticity and rotary Brownian motion.

Appendix A. The Stokes velocity field due to a force-free freely rotating spheroid in simple shear flow

Although the detailed derivation of the canonical velocity fields for a spheroid discussed later in the appendix is described in Dabade *et al.* (2015) and Dabade *et al.* (2016), we nevertheless give a brief discussion in what follows. The velocity

https://doi.org/10.1017/jfm.2018.184 Published online by Cambridge University Press

fields are derived using the vector spheroidal harmonics formalism developed by Kuschch and coworkers in the context of determining the averaged properties of a composite consisting of an elastic matrix with spheroidal inclusions (Kushch 1997; Kushch 1998). The formalism gives the velocity field around a single spheroid as a superposition of decaying spheroidal harmonics in a spheroidal coordinate system. For a prolate spheroid, the spheroidal coordinates (ξ, η, ϕ) are related to Cartesian coordinates (x, y, z) as $x + \mathrm{i}y = d\bar{\xi}\bar{\eta}\exp(\mathrm{i}\phi)$ and $z = d\xi\eta$, with $\bar{\xi} = \sqrt{(\xi^2 - 1)}$ and $\bar{\eta} = \sqrt{(1 - \eta^2)}$, where d is the interfocal distance. Here, the constant ξ surfaces denote a family of confocal prolate spheroids with the interfocus distance being equal to $2d$; ξ_0 denotes the surface of the particle. The constant η surfaces represent a family of confocal two-sheeted hyperboloids, while the constant ϕ surfaces are planes passing through the axis of symmetry. The disturbance velocity fields are derived by identifying the right combination of the decaying harmonics, along with the multiplying constants, that satisfy the boundary conditions at the surface of the spheroid ($\xi = \xi_0$) for each of the component flows. The disturbance fields thus derived have been validated with the velocity fields obtained earlier from the method of singularities by Chwang & Wu (1974, 1975) and Chwang (1975) in the appendix of Dabade *et al.* (2016). The corresponding velocity fields, for an oblate spheroid, can be derived using the transformation $\xi = \mathrm{i}\sqrt{\xi^2 - 1}$ and $d = -\mathrm{i}d$ (Dabade *et al.* 2015, 2016).

Below, we present the Stokes disturbance velocity field around a spheroid in simple shear flow originally derived by Dabade *et al.* (2016). These velocity fields are expressed in the body-aligned coordinate system shown in figure 1(*f*). The disturbance velocity fields corresponding to the five canonical linear flows mentioned in § 3 are given by

$$\begin{aligned}
\boldsymbol{u}_{1s}(0) \;=\; & -\frac{d\bar{\xi}_0}{(Q_1^1(\xi_0) - \xi_0 Q_2^1(\xi_0))}(\sin^2\theta_j \sin\phi_j \cos\phi_j) \\
& \times \left[\boldsymbol{x}\frac{\partial}{\partial z}(P_1^0 Q_1^0) - \mathbf{1}_z d\xi_0^2 \frac{\partial}{\partial z}(P_2^0 Q_2^0) - d\bar{\xi}_0^2 \left(\mathbf{1}_x \frac{\partial}{\partial x} + \mathbf{1}_y \frac{\partial}{\partial y}\right)(P_2^0 Q_2^0)\right], \quad \text{(A 1)} \\
\boldsymbol{u}_{2s}(0) \;=\; & \frac{d\bar{\xi}_0}{(\xi_0 Q_2^1(\xi_0) - 3Q_1^1(\xi_0))}(1 + \cos^2\theta_j) \sin\phi_j \cos\phi_j \\
& \times \left[\boldsymbol{x}\left\{\frac{\partial}{\partial y}(P_1^1 Q_1^1 \sin\phi) - \frac{\partial}{\partial x}(P_1^1 Q_1^1 \cos\phi)\right\}\right. \\
& \left. - \frac{d\bar{\xi}_0^2}{12}\left(\mathbf{1}_x \frac{\partial}{\partial x} + \mathbf{1}_y \frac{\partial}{\partial y}\right)(P_2^2 Q_2^2 \cos 2\phi) - \frac{d\xi_0^2}{12}\mathbf{1}_z \frac{\partial}{\partial z}(P_2^2 Q_2^2 \cos 2\phi)\right], \quad \text{(A 2)} \\
\boldsymbol{u}_{3s}(0) \;=\; & \frac{d\bar{\xi}_0}{(3Q_1^1(\xi_0) - \xi_0 Q_2^1(\xi_0))} \cos\theta_j(\cos^2\phi_j - \sin^2\phi_j) \\
& \times \left[\boldsymbol{x}\left\{\frac{\partial}{\partial x}(P_1^1 Q_1^1 \sin\phi) + \frac{\partial}{\partial y}(P_1^1 Q_1^1 \cos\phi)\right\}\right. \\
& \left. + \frac{d\bar{\xi}_0^2}{12}\left(\mathbf{1}_x \frac{\partial}{\partial x} + \mathbf{1}_y \frac{\partial}{\partial y}\right)(P_2^2 Q_2^2 \sin 2\phi) + \frac{d\xi_0^2}{12}\mathbf{1}_z \frac{\partial}{\partial z}(P_2^2 Q_2^2 \sin 2\phi)\right], \quad \text{(A 3)}
\end{aligned}$$

https://doi.org/10.1017/jfm.2018.184 Published online by Cambridge University Press

$$\boldsymbol{u}_{4s}(0) = \frac{2d\xi_0\bar{\xi}_0}{Q_2^1(\xi_0)(2\xi_0^2-1)}(\sin\theta_j\cos\theta_j\sin\phi_j\cos\phi_j) \times \left[\boldsymbol{x}\frac{\partial}{\partial z}(P_1^1Q_1^1\cos\phi) - \frac{d\xi_0^2}{3}\mathbf{1}_z\frac{\partial}{\partial z}(P_2^1Q_2^1\cos\phi) - \frac{d\bar{\xi}_0^2}{3}\left(\mathbf{1}_x\frac{\partial}{\partial x}+\mathbf{1}_y\frac{\partial}{\partial y}\right)(P_2^1Q_2^1\cos\phi)\right], \tag{A 4}$$

$$\boldsymbol{u}_{5s}(0) = \frac{d\xi_0\bar{\xi}_0}{Q_2^1(\xi_0)(2\xi_0^2-1)}\sin\theta_j(\cos^2\phi_j-\sin^2\phi_j) \times \left[\boldsymbol{x}\frac{\partial}{\partial z}(P_1^1Q_1^1\sin\phi) - \frac{d\xi_0^2}{3}\mathbf{1}_z\frac{\partial}{\partial z}(P_2^1Q_2^1\sin\phi) - \frac{d\bar{\xi}_0^2}{3}\left(\mathbf{1}_x\frac{\partial}{\partial x}+\mathbf{1}_y\frac{\partial}{\partial y}\right)(P_2^1Q_2^1\sin\phi)\right]. \tag{A 5}$$

Here, $P_t^s(\eta)$ and $Q_t^s(\xi)$ are the associated Legendre functions of the first and second kind respectively (Morse & Feshbach 1953). The vector $\boldsymbol{x}$ in the above expressions is given by $x\mathbf{1}_x + y\mathbf{1}_y + z\mathbf{1}_z$. The velocity fields in the test problem are given by

$$\boldsymbol{u}_{sx}^{(2)} = -\frac{d(2\xi_0^2-1)}{(2\xi_0Q_1^0(\xi_0)-\bar{\xi}_0Q_1^1(\xi_0))}(2P_1^0Q_1^0\mathbf{1}_y + P_1^1Q_1^1\sin\phi\mathbf{1}_z) - \frac{d}{(2\xi_0Q_1^0(\xi_0)-\bar{\xi}_0Q_1^1(\xi_0))}\left[\boldsymbol{x}\frac{\partial}{\partial z}(P_1^1Q_1^1\sin\phi) - \frac{d\xi_0^2}{3}\mathbf{1}_z\frac{\partial}{\partial z}(P_2^1Q_2^1\sin\phi) - \frac{d\bar{\xi}_0^2}{3}\left(\mathbf{1}_x\frac{\partial}{\partial x}+\mathbf{1}_y\frac{\partial}{\partial y}\right)(P_2^1Q_2^1\sin\phi)\right], \tag{A 6}$$

$$\boldsymbol{u}_{sy}^{(2)} = \frac{d(2\xi_0^2-1)}{(2\xi_0Q_1^0(\xi_0)-\bar{\xi}_0Q_1^1(\xi_0))}(2P_1^0Q_1^0\mathbf{1}_x + P_1^1Q_1^1\cos\phi\mathbf{1}_z) + \frac{d}{(2\xi_0Q_1^0(\xi_0)-\bar{\xi}_0Q_1^1(\xi_0))}\left[\boldsymbol{x}\frac{\partial}{\partial z}(P_1^1Q_1^1\cos\phi) - \frac{d\xi_0^2}{3}\mathbf{1}_z\frac{\partial}{\partial z}(P_2^1Q_2^1\cos\phi) - \frac{d\bar{\xi}_0^2}{3}\left(\mathbf{1}_x\frac{\partial}{\partial x}+\mathbf{1}_y\frac{\partial}{\partial y}\right)(P_2^1Q_2^1\cos\phi)\right], \tag{A 7}$$

$$\boldsymbol{u}_{sz}^{(2)} = \frac{d\bar{\xi}_0}{Q_1^1(\xi_0)}(-\sin\phi\mathbf{1}_x + \cos\phi\mathbf{1}_y)(P_1^1Q_1^1). \tag{A 8}$$

Appendix B. The functions in the $O(Re)$ and $O(St)$ correction to the angular velocity

The functions of κ and λ that appear in (5.4) and (5.5) for a prolate spheroid are given by

$$F_1^p(\xi_0,\lambda) = \frac{\left(-1+\xi_0^2\right)\left(-3+2\lambda-3\lambda^2+4(-1+\lambda)^2\xi_0^2\right)\left(-\xi_0+\coth^{-1}\xi_0\left(1+\xi_0^2\right)\right)}{160\xi_0\left(1-2\xi_0^2\right)^2}, \tag{B 1}$$

$$F_2^p(\xi_0,\lambda) = -\frac{\left(-1+\lambda^2\right)\left(-1+\xi_0^2\right)^2\left(-\xi_0+\coth^{-1}\xi_0\left(1+\xi_0^2\right)\right)}{40\xi_0\left(1-2\xi_0^2\right)^2}, \tag{B 2}$$

https://doi.org/10.1017/jfm.2018.184 Published online by Cambridge University Press

$$F_3^p(\xi_0,\lambda)=F_4^p(\xi_0,\lambda)=-\frac{(1+\lambda)^2\left(-1+\xi_0^2\right)\left(-\xi_0+\coth^{-1}\xi_0\left(1+\xi_0^2\right)\right)}{160\xi_0\left(1-2\xi_0^2\right)^2}, \tag{B 3}$$

$$F_5^p(\xi_0,\lambda)=F_6^p(\xi_0,\lambda)=\frac{(1+\lambda)^2\left(-1+\xi_0^2\right)\left(-\xi_0+\coth^{-1}\xi_0\left(1+\xi_0^2\right)\right)}{320\xi_0\left(1-2\xi_0^2\right)^2}, \tag{B 4}$$

$$G_1^p(\xi_0,\lambda)=\frac{\left(-1+\lambda^2\right)\left(2-5\xi_0^2+3\xi_0^4\right)\left(-\xi_0+\coth^{-1}\xi_0\left(1+\xi_0^2\right)\right)}{40\xi_0\left(1-2\xi_0^2\right)^2}, \tag{B 5}$$

$$G_2^p(\xi_0,\lambda)=-\frac{\left(-1+\lambda^2\right)\xi_0\left(-1+\xi_0^2\right)\left(-\xi_0+\coth^{-1}\xi_0\left(1+\xi_0^2\right)\right)}{40\left(1-2\xi_0^2\right)^2}, \tag{B 6}$$

$$G_3^p(\xi_0,\lambda)=-G_4^p(\xi_0,\lambda)=\frac{(1+\lambda)^2\left(-1+\xi_0^2\right)\left(-\xi_0+\coth^{-1}\xi_0\left(1+\xi_0^2\right)\right)}{40\xi_0\left(1-2\xi_0^2\right)^2}. \tag{B 7}$$

The functions for an oblate spheroid can be obtained using the transformation $\xi_0 \leftrightarrow \mathrm{i}\bar{\xi}_0$ and $d \leftrightarrow -\mathrm{id}$ on the dimensional angular velocity, having accounted for the aspect-ratio dependence that occurs in the relevant non-dimensional parameter – *St* here and *Re* in § 6.

The aspect-ratio- and λ-dependent functions in (6.1) and (6.2), for a prolate spheroid, are given by

$$F_1^f(\xi_0,\lambda)=(1+\lambda)^2F_1^f(\xi_0,0)+\frac{\lambda\left(\xi_0-\xi_0^3+\left(-1+\xi_0^4\right)\coth^{-1}\xi_0\right)}{20\xi_0\left(-1+2\xi_0^2\right)}, \tag{B 8}$$

$$F_2^f(\xi_0,\lambda)=(1-\lambda^2)F_2^f(\xi_0,0), \tag{B 9}$$

$$F_3^f(\xi_0,\lambda)=(\lambda+1)^2F_3^f(\xi_0,0), \tag{B 10}$$

$$F_4^f(\xi_0,\lambda)=(\lambda+1)^2F_4^f(\xi_0,0), \tag{B 11}$$

$$F_5^f(\xi_0,\lambda)=F_6^f(\xi_0,\lambda)=(\lambda+1)^2F_5^f(\xi_0,0), \tag{B 12}$$

$$G_1^f(\xi_0,\lambda)=(1-\lambda^2)G_1^f(\xi_0,0), \tag{B 13}$$

$$G_2^f(\xi_0,\lambda)=(1-\lambda^2)G_2^f(\xi_0,0), \tag{B 14}$$

$$G_3^f(\xi_0,\lambda)=(\lambda+1)^2G_3^f(\xi_0,0), \tag{B 15}$$

$$G_4^f(\xi_0,\lambda)=(\lambda+1)^2G_4^f(\xi_0,0), \tag{B 16}$$

where the $F_i^f(\xi_0,0)$ and $G_i^f(\xi_0,0)$ are given by (6.1) to (6.8) in Dabade *et al.* (2016). These functions were originally given by Dabade *et al.* (2016) and are reproduced below.

$$\begin{aligned}
F_1^f(\xi_0,0) \;=\; & \left(\xi_0^2(-648\xi_0^{12}+1350\xi_0^{10}-5571\xi_0^8+11841\xi_0^6-9269\xi_0^4+2263\xi_0^2+6)\right.\\
& -27\xi_0^2(24\xi_0^8-14\xi_0^6-19\xi_0^4+16\xi_0^2-3)\bar{\xi}_0^8\coth^{-1}(\xi_0)^4+9\xi_0\\
& \times(288\xi_0^{12}-564\xi_0^{10}-20\xi_0^8+799\xi_0^6-743\xi_0^4+261\xi_0^2-29)\bar{\xi}_0^4\\
& \times\coth^{-1}(\xi_0)^3+\xi_0\left(2592\xi_0^{14}-7020\xi_0^{12}+13932\xi_0^{10}-21123\xi_0^8+14255\xi_0^6\right.\\
& \left.-577\xi_0^4-2711\xi_0^2+652\right)\coth^{-1}\xi_0-3\left(1296\xi_0^{16}-4320\xi_0^{14}+5346\xi_0^{12}\right.\\
& \left.-1477\xi_0^{10}-4260\xi_0^8+6116\xi_0^6-3492\xi_0^4+849\xi_0^2-58\right)\coth^{-1}(\xi_0)^2\Big)\\
& \times\left(480\xi_0^2(-1+2\xi_0^2)^3(-3\xi_0^2+3\bar{\xi}_0^2\xi_0\coth^{-1}\xi_0+2)\right.\\
& \left.\times(-3\xi_0^3+5\xi_0+3\bar{\xi}_0^4\coth^{-1}\xi_0)((3\xi_0^2-1)\coth^{-1}\xi_0-3\xi_0)\right)^{-1},
\end{aligned} \tag{B 17}$$

https://doi.org/10.1017/jfm.2018.184 Published online by Cambridge University Press

$$F_2^f(\xi_0,0) = -\left(\bar{\xi}_0^2\left(-9\xi_0^9+30\xi_0^7-115\xi_0^5+90\xi_0^3-12\xi_0+9\bar{\xi}_0^8(\xi_0^2+1)\xi_0^2\coth^{-1}(\xi_0)^3\right.\right.$$
$$-3\bar{\xi}_0^4(9\xi_0^6-10\xi_0^4-17\xi_0^2+14)\xi_0\coth^{-1}(\xi_0)^2$$
$$\left.+(27\xi_0^{10}-87\xi_0^8+133\xi_0^6-33\xi_0^4-52\xi_0^2+12)\coth^{-1}\xi_0\right)\left(40(\xi_0-2\xi_0^3)^2\right.$$
$$\left.\times(-3\xi_0^2+3\bar{\xi}_0^2\xi_0\coth^{-1}\xi_0+2)(-3\xi_0^3+5\xi_0+3\bar{\xi}_0^4\coth^{-1}\xi_0)\right)^{-1}, \quad \text{(B 18)}$$

$$F_3^f(\xi_0,0) = -\left(\xi_0^2(378\xi_0^{10}+801\xi_0^8-4731\xi_0^6+5551\xi_0^4-2369\xi_0^2+342)\right.$$
$$-27\xi_0^2(6\xi_0^6+\xi_0^4-4\xi_0^2+1)\bar{\xi}_0^8\coth^{-1}(\xi_0)^4+9\xi_0\left(12\xi_0^{10}+28\xi_0^8-201\xi_0^6\right.$$
$$\left.+273\xi_0^4-147\xi_0^2+27\right)\bar{\xi}_0^4\coth^{-1}(\xi_0)^3+\left(-972\xi_0^{13}-324\xi_0^{11}+7365\xi_0^9\right.$$
$$\left.-10409\xi_0^7+5143\xi_0^5-847\xi_0^3+44\xi_0\right)\coth^{-1}\xi_0+3\left(216\xi_0^{14}-378\xi_0^{12}\right.$$
$$\left.+109\xi_0^{10}-412\xi_0^8+1204\xi_0^6-1028\xi_0^4+311\xi_0^2-22\right)$$
$$\times\coth^{-1}(\xi_0)^2\left)\left(480\xi_0^2(-1+2\xi_0^2)^3(-3\xi_0^2+3\bar{\xi}_0^2\xi_0\coth^{-1}\xi_0+2)\right.\right.$$
$$\left.\left.\times(-3\xi_0^3+5\xi_0+3\bar{\xi}_0^4\coth^{-1}\xi_0)((3\xi_0^2-1)\coth^{-1}\xi_0-3\xi_0)\right)^{-1}, \quad \text{(B 19)}$$

$$F_4^f(\xi_0,0) = -2F_5^f(\xi_0,0) = -2F_6^f(\xi_0,0) = F_3^f(\xi_0,0), \quad \text{(B 20)}$$

$$G_1^f(\xi_0,0) = \left(\xi_0^2(81\xi_0^{10}-414\xi_0^8+1074\xi_0^6-1162\xi_0^4+479\xi_0^2-54)\right.$$
$$+9\xi_0^2(9\xi_0^6-7\xi_0^2+2)\bar{\xi}_0^8\coth^{-1}(\xi_0)^4-3\xi_0\left(108\xi_0^{10}-246\xi_0^8+69\xi_0^6\right.$$
$$\left.+167\xi_0^4-129\xi_0^2+23\right)\bar{\xi}_0^4\coth^{-1}(\xi_0)^3+\left(-324\xi_0^{13}+1566\xi_0^{11}-3309\xi_0^9\right.$$
$$\left.+3133\xi_0^7-1023\xi_0^5-79\xi_0^3+36\xi_0\right)\coth^{-1}\xi_0$$
$$+(486\xi_0^{14}-2214\xi_0^{12}+3819\xi_0^{10}-2568\xi_0^8-222\xi_0^6+1036\xi_0^4-355\xi_0^2+18)$$
$$\times\coth^{-1}(\xi_0)^2\left)\left(40(\xi_0-2\xi_0^3)^2(-3\xi_0^2+3\bar{\xi}_0^2\xi_0\coth^{-1}\xi_0+2)\right.\right.$$
$$\left.\left.\times(-3\xi_0^3+5\xi_0+3\bar{\xi}_0^4\coth^{-1}\xi_0)((3\xi_0^2-1)\coth^{-1}\xi_0-3\xi_0)\right)^{-1}, \quad \text{(B 21)}$$

$$G_2^f(\xi_0,0) = \left(-\xi_0^2(27\xi_0^{10}-180\xi_0^8+204\xi_0^6+68\xi_0^4-133\xi_0^2+18)\right.$$
$$-9\xi_0^4(3\xi_0^4+2\xi_0^2-1)\bar{\xi}_0^8\coth^{-1}(\xi_0)^4+3\xi_0$$
$$\times(36\xi_0^{10}-78\xi_0^8+73\xi_0^6-69\xi_0^4+35\xi_0^2-5)\bar{\xi_0}^4\coth^{-1}(\xi_0)^3$$
$$+\xi_0(108\xi_0^{12}-630\xi_0^{10}+1041\xi_0^8-617\xi_0^6+115\xi_0^4-29\xi_0^2+12)$$
$$\times\coth^{-1}\xi_0+\left(-162\xi_0^{14}+810\xi_0^{12}-1551\xi_0^{10}+1600\xi_0^8\right.$$
$$\left.-1054\xi_0^6+448\xi_0^4-97\xi_0^2+6\right)\coth^{-1}(\xi_0)^2\left)\right.$$
$$\left.\times\left(40(\xi_0-2\xi_0^3)^2(-3\xi_0^2+3\bar{\xi}_0^2\xi_0\coth^{-1}\xi_0+2)\right.\right.$$
$$\left.\left.\times(-3\xi_0^3+5\xi_0+3\bar{\xi}_0^4\coth^{-1}\xi_0)((3\xi_0^2-1)\coth^{-1}\xi_0-3\xi_0)\right)^{-1}, \quad \text{(B 22)}$$

$$G3^f(\xi_0,0) = \left(\xi_0^2(378\xi_0^{10}+801\xi_0^8-4731\xi_0^6+5551\xi_0^4-2369\xi_0^2+342)\right.$$
$$-27\xi_0^2(6\xi_0^6+\xi_0^4-4\xi_0^2+1)\bar{\xi}_0^8\coth^{-1}(\xi_0)^4$$
$$+9\xi_0(12\xi_0^{10}+28\xi_0^8-201\xi_0^6+273\xi_0^4-147\xi_0^2+27)\bar{\xi}_0^4\coth^{-1}(\xi_0)^3$$
$$+(-972\xi_0^{13}-324\xi_0^{11}+7365\xi_0^9-10409\xi_0^7+5143\xi_0^5-847\xi_0^3+44\xi_0)$$
$$\times\coth^{-1}\xi_0+3\left(216\xi_0^{14}-378\xi_0^{12}+109\xi_0^{10}-412\xi_0^8+1204\xi_0^6-1028\xi_0^4\right.$$
$$\left.+311\xi_0^2-22\right)\coth^{-1}(\xi_0)^2\left.\right)$$

https://doi.org/10.1017/jfm.2018.184 Published online by Cambridge University Press

$$\times \left(120\xi_0^2(2\xi_0^2-1)^3(-3\xi_0^2+3\bar{\xi}_0^2\xi_0\coth^{-1}\xi_0+2)\right.$$
$$\left.\times(-3\xi_0^3+5\xi_0+3\bar{\xi}_0^4\coth^{-1}\xi_0)((3\xi_0^2-1)\coth^{-1}\xi_0-3\xi_0)\right)^{-1}, \tag{B 23}$$

$$G_4^f(\xi_0,0)=-G_3^f(\xi_0,0). \tag{B 24}$$

The second term in (B 8) is the contribution due to the ambient pressure field, and, accordingly, vanishes for a simple shear flow. The functions for an oblate spheroid can be obtained using the prolate–oblate transformation mentioned in §§ 3 and 5.

Appendix C. The integrals in the orbital drift approximation

The integrals in the drift approximation in (5.10) and (6.3) are given by

$$I_1=2\pi, \tag{C 1}$$

$$I_2=2\pi(\kappa_{eq}-1)(\kappa_{eq}+1)^{-1}, \tag{C 2}$$

$$I_3=2\pi\left(2\left(\left(C^2+1\right)\left(C^2\kappa_{eq}^2+1\right)\right)^{-1/2}-1\right), \tag{C 3}$$

$$I_4=2\pi(\kappa_{eq}-1)^2(\kappa_{eq}+1)^{-2}, \tag{C 4}$$

$$\begin{aligned} I_5+I_6 = &-\left(4\pi\left(2\kappa_{eq}^2\left(3\sqrt{\left(C^2+1\right)\left(C^2\kappa_{eq}^2+1\right)}-8C^2-6\right)\right.\right.\\ &+4\kappa_{eq}\sqrt{\left(C^2+1\right)\left(C^2\kappa_{eq}^2+1\right)}\\ &+\sqrt{\left(C^2+1\right)\left(C^2\kappa_{eq}^2+1\right)}+4\left(4C^2+1\right)\kappa_{eq}^3\sqrt{\left(C^2+1\right)\left(C^2\kappa_{eq}^2+1\right)}\\ &\left.\left.+\kappa_{eq}^4\left(\sqrt{\left(C^2+1\right)\left(C^2\kappa_{eq}^2+1\right)}-16\left(C^4+C^2\right)-2\right)-2\right)\right)\\ &\times\left(\left(\kappa_{eq}^2-1\right)^2\sqrt{\left(C^2+1\right)\left(C^2\kappa_{eq}^2+1\right)}\right)^{-1}, \end{aligned} \tag{C 5}$$

$$J_1=\pi(\kappa_{eq}^2-1)(\kappa_{eq}+1)^{-2}, \tag{C 6}$$

$$J_2=-\pi(\kappa_{eq}^2-1)\left(-4\sqrt{\left(C^2+1\right)\left(C^2\kappa_{eq}^2+1\right)}+C^2(\kappa_{eq}+1)^2+4\right)C^{-2}\left(\kappa_{eq}^2-1\right)^{-2}, \tag{C 7}$$

$$J_3=\pi(\kappa_{eq}^2-1)(\kappa_{eq}-1)(\kappa_{eq}+1)^{-3}, \tag{C 8}$$

$$\begin{aligned} J_4 = &-\pi(\kappa_{eq}^2-1)\left(8C^4\kappa_{eq}^3+C^2\left((\kappa_{eq}+1)^4-8\kappa_{eq}^2\sqrt{\left(C^2+1\right)\left(C^2\kappa_{eq}^2+1\right)}\right)\right.\\ &\left.-4\left(\kappa_{eq}^2+1\right)\left(\sqrt{\left(C^2+1\right)\left(C^2\kappa_{eq}^2+1\right)}-1\right)\right)C^{-2}\left(\kappa_{eq}^2-1\right)^{-3}. \end{aligned} \tag{C 9}$$

It should be noted that only I_5+I_6 matters since $F_5^p(\xi_0,\lambda)=F_6^p(\xi_0,\lambda)$ (see (B 4)) and $F_5^f(\xi_0)=F_6^f(\xi_0)$ (see (B 12)).

Appendix D. Orbital coordinate system

The details of the $(C,\ \tau)$ coordinate system are given below. The orbital coordinates $(C,\ \tau)$ are related to the spherical coordinate angles, θ_j and ϕ_j, as $C=(\tan\theta_j(\kappa_{eq}^2\sin^2\phi_j+\cos^2\phi_j)^{1/2})/\kappa_{eq}$ and $\tan\tau=1/(\kappa_{eq}\tan\phi_j)$. The unit vectors $\hat{\boldsymbol{C}}$

https://doi.org/10.1017/jfm.2018.184 Published online by Cambridge University Press

and $\hat{\boldsymbol{\tau}}$ are given by $(\partial\hat{\boldsymbol{r}}/\partial C)/|\partial\hat{\boldsymbol{r}}/\partial C|$ and $(\partial\hat{\boldsymbol{r}}/\partial\tau)/|\partial\hat{\boldsymbol{r}}/\partial\tau|$ respectively, where $\hat{\boldsymbol{r}}$ is the unit radial vector in spherical coordinates ($\hat{\boldsymbol{r}} = \sin\theta_j\cos\phi_j\mathbf{1}'_x + \sin\theta_j\sin\phi_j\mathbf{1}'_y + \cos\theta_j\mathbf{1}'_z$). The metric factors h_C and h_τ are given by $|\partial\hat{\boldsymbol{r}}/\partial C|$ and $|\partial\hat{\boldsymbol{r}}/\partial\tau|$ respectively. On simplifying, one obtains

$$\hat{\boldsymbol{C}} = \cos\theta_j\cos\phi_j\mathbf{1}'_x + \cos\theta_j\sin\phi_j\mathbf{1}'_y - \sin\theta_j\mathbf{1}'_z = \hat{\boldsymbol{\theta}}_{\boldsymbol{j}}, \tag{D 1}$$

$$\hat{\boldsymbol{\tau}} = \frac{\dfrac{\partial\theta_j}{\partial\tau}}{\sqrt{\left(\dfrac{\partial\theta_j}{\partial\tau}\right)^2 + \left(\dfrac{\partial\phi_j}{\partial\tau}\right)^2\sin^2\theta_j}}\hat{\boldsymbol{\theta}}_{\boldsymbol{j}} + \frac{\dfrac{\partial\phi_j}{\partial\tau}\sin\theta_j}{\sqrt{\left(\dfrac{\partial\theta_j}{\partial\tau}\right)^2 + \left(\dfrac{\partial\phi_j}{\partial\tau}\right)^2\sin^2\theta_j}}\hat{\boldsymbol{\phi}}_{\boldsymbol{j}}, \tag{D 2}$$

$$h_C = \frac{\partial\theta_j}{\partial C}, \tag{D 3}$$

$$h_\tau = \sqrt{\left(\frac{\partial\theta_j}{\partial\tau}\right)^2 + \left(\frac{\partial\phi_j}{\partial\tau}\right)^2\sin^2\theta_j}, \tag{D 4}$$

where $\hat{\boldsymbol{\theta}}_{\boldsymbol{j}}$ and $\hat{\boldsymbol{\phi}}_{\boldsymbol{j}} = -\sin(\phi_j)\mathbf{1}'_x + \cos(\phi_j)\mathbf{1}'_y$ are the polar and azimuthal unit vectors in the spherical coordinate system, and $\hat{\boldsymbol{\tau}}$ is tangent to a Jeffery orbit. The (C, τ) is a non-orthogonal coordinate system, and the angle (α) between the unit vectors $\hat{\boldsymbol{C}}$ and $\hat{\boldsymbol{\tau}}$ is given by

$$\cos\alpha = \frac{\dfrac{\partial\theta_j}{\partial\tau}}{\sqrt{\left(\dfrac{\partial\theta_j}{\partial\tau}\right)^2 + \left(\dfrac{\partial\phi_j}{\partial\tau}\right)^2\sin^2\theta_j}}. \tag{D 5}$$

The $\hat{\boldsymbol{\tau}}$ can then be written as $\cos\alpha\hat{\boldsymbol{\theta}}_{\boldsymbol{j}} + \sin\alpha\hat{\boldsymbol{\phi}}_{\boldsymbol{j}}$.

REFERENCES

D'Avino, G., Hulsen, M. A., Greco, F. & Maffettone, P. L. 2014 Bistability and metabistability scenario in the dynamics of an ellipsoidal particle in a sheared viscoelastic fluid. *Phys. Rev.* E **89** (4), 043006.

Babcock, H. P., Teixeira, R. E., Hur, J. S., Shaqfeh, E. S. G. & Chu, S. 2003 Visualization of molecular fluctuations near the critical point of the coil–stretch transition in polymer elongation. *Macromolecules* **36** (12), 4544–4548.

Bender, C. M. & Orszag, S. A. 1999 *Advanced Mathematical Methods for Scientists and Engineers I*. Springer.

Bentley, B. J. & Leal, L. G. 1986 An experimental investigation of drop deformation and breakup in steady, two-dimensional linear flows. *J. Fluid Mech.* **167**, 241–283.

Bretherton, F. P. 1962 The motion of rigid particles in a shear flow at low Reynolds number. *J. Fluid Mech.* **14** (2), 284–304.

Candelier, F., Einarsson, J., Lundell, F., Mehlig, B. & Angilella, J.-R. 2015*a* Role of inertia for the rotation of a nearly spherical particle in a general linear flow. *Phys. Rev.* E **91** (5), 053023.

Candelier, F., Einarsson, J., Lundell, F., Mehlig, B. & Angilella, J.-R. 2015*b* Role of inertia for the rotation of a nearly spherical particle in a general linear flow (erratum). *Phys. Rev.* E **92**, 059901.

Candelier, F., Einarsson, J. & Mehlig, B. 2016 Angular dynamics of a small particle in turbulence. *Phys. Rev. Lett.* **117** (20), 204501.

https://doi.org/10.1017/jfm.2018.184 Published online by Cambridge University Press

CHANDRASEKHAR, S. 1943 Stochastic problems in physics and astronomy. *Rev. Mod. Phys.* **15** (1), 1.

CHWANG, A. T. 1975 Hydromechanics of low-Reynolds-number flow. Part 3. Motion of a spheroidal particle in quadratic flows. *J. Fluid Mech.* **72**, 17–34.

CHWANG, A. T. & WU, T. Y.-T. 1974 Hydromechanics of low-Reynolds-number flow. Part 1. Rotation of axisymmetric prolate bodies. *J. Fluid Mech.* **63**, 607–622.

CHWANG, A. T. & WU, T. Y.-T. 1975 Hydromechanics of low-Reynolds-number flow. Part 2. Singularity method for Stokes flows. *J. Fluid Mech.* **67**, 787–815.

DABADE, V., MARATH, N. K. & SUBRAMANIAN, G. 2015 Effects of inertia and viscoelasticity on sedimenting anisotropic particles. *J. Fluid Mech.* **778**, 133–188.

DABADE, V., MARATH, N. K. & SUBRAMANIAN, G. 2016 The effect of inertia on the orientation dynamics of anisotropic particles in simple shear flow. *J. Fluid Mech.* **791**, 631–703.

DE GENNES, P. G. 1974 Coil–stretch transition of dilute flexible polymers under ultrahigh velocity gradients. *J. Chem. Phys.* **60** (12), 5030–5042.

EINARSSON, J., ANGILELLA, J. R. & MEHLIG, B. 2014 Orientational dynamics of weakly inertial axisymmetric particles in steady viscous flows. *Physica* D **278**, 79–85.

EINARSSON, J., CANDELIER, F., LUNDELL, F., ANGILELLA, J. R. & MEHLIG, B. 2015 Rotation of a spheroid in a simple shear at small Reynolds number. *Phys. Fluids* **27** (6), 063301.

ENNIS, G. J., OKAGAWA, A. & MASON, S. G. 1978 Memory impairment in flowing suspensions. II. Experimental results. *Can. J. Chem.* **56** (22), 2824–2832.

HINCH, E. J. 1974 Mechanical models of dilute polymer solutions for strong flows with large polymer deformations. *Colloq. Intl CNRS* **233**, 241–247.

HINCH, E. J. & LEAL, L. G. 1972 The effect of Brownian motion on the rheological properties of a suspension of non-spherical particles. *J. Fluid Mech.* **52**, 683–712.

HOFFMAN, B. D. & SHAQFEH, E. S. G. 2007 The dynamics of the coil–stretch transition for long, flexible polymers in planar mixed flows. *J. Rheol.* **51** (5), 947–969.

HUDSON, S. D., PHELAN, F. R. JR., HANDLER, M. D., CABRAL, J. T., MIGLER, K. B. & AMIS, E. J. 2004 Microfluidic analog of the four-roll mill. *Appl. Phys. Lett.* **85** (2), 335–337.

IVANOV, Y., VAN DE VEN, T. G. M. & MASON, S. G. 1982 Damped oscillations in the viscosity of suspensions of rigid rods. I. Monomodal suspensions. *J. Rheol.* **26** (2), 213–230.

JEFFERY, G. B. 1922 The motion of ellipsoidal particles immersed in a viscous fluid. *Proc. R. Soc. Lond.* A **102**, 161–179.

KARNIS, A., GOLDSMITH, H. L. & MASON, S. G. 1963 Axial migration of particles in Poiseuille flow. *Nature* **200** (4902), 159–160.

KIM, S. & KARRILA, S. J. 1991 *Microhydrodynamics: Principles and Selected Applications*. Butterworth–Heinemann.

KRISHNAMURTHY, D. 2014 Heat transfer from drops in shearing flows and collective motion in micro-scale swimmer suspensions. Master's thesis, Jawaharlal Nehru Centre for Advanced Scientific Research, Bangalore, India.

KRISHNAMURTHY, D. & SUBRAMANIAN, G. 2018*a* Heat or mass transport from drops in shearing flows. Part 1. The open streamline. *J. Fluid Mech.* (submitted).

KRISHNAMURTHY, D. & SUBRAMANIAN, G. 2018*b* Heat or mass transport from drops in shearing flows. Part 2. Inertial effects on transport. *J. Fluid Mech.* (submitted).

KUSHCH, V. I. 1997 Microstresses and effective elastic moduli of a solid reinforced by periodically distributed spheroidal particles. *Intl J. Solids Struct.* **34**, 1353–1366.

KUSHCH, V. I. 1998 Elastic equilibrium of a medium containing a finite number of arbitrarily oriented spheroidal inclusions. *Intl J. Solids Struct.* **35**, 1187–1198.

LEAL, L. G. 1979 The motion of small particles in non-Newtonian fluids. *J. Non-Newtonian Fluid Mech.* **5**, 33–78.

LEAL, L. G. 2004 Flow induced coalescence of drops in a viscous fluid. *Phys. Fluids* **16** (6), 1833–1851.

LEAL, L. G. & HINCH, E. J. 1971 The effect of weak Brownian rotations on particles in shear flow. *J. Fluid Mech.* **46**, 685–703.

https://doi.org/10.1017/jfm.2018.184 Published online by Cambridge University Press

LEE, J. S., DYLLA-SPEARS, R., TECLEMARIAM, N. P. & MULLER, S. J. 2007*a* Microfluidic four-roll mill for all flow types. *Appl. Phys. Lett.* **90** (7), 074103.

LEE, J. S., SHAQFEH, E. S. G. & MULLER, S. J. 2007*b* Dynamics of DNA tumbling in shear to rotational mixed flows: pathways and periods. *Phys. Rev.* E **75** (4), 040802.

LIOU, K.-N. 1986 Influence of cirrus clouds on weather and climate processes: a global perspective. *Mon. Weath. Rev.* **114** (6), 1167–1199.

MARATH, N. K., DWIVEDI, R. & SUBRAMANIAN, G. 2017 An orientational order transition in a sheared suspension of anisotropic particles. *J. Fluid Mech.* **811**, R3.

MARATH, N. K. & SUBRAMANIAN, G. 2017 The effect of inertia on the time period of rotation of an anisotropic particle in simple shear flow. *J. Fluid Mech.* **830**, 165–210.

MARATH, N. K. & SUBRAMANIAN, G. 2017 The orientation dynamics of anisotropic particles in shearing flows. PhD thesis, Jawaharlal Nehru Centre for Advanced Scientific Research, Bangalore, India.

MORSE, P. M. & FESHBACH, H. 1953 *Methods of Theoretical Physics*. McGraw-Hill.

OKAGAWA, A., COX, R. G. & MASON, S. 1973 The kinetics of flowing dispersions. VII. Oscillatory behavior of rods and discs in shear flow. *J. Colloid Interface Sci.* **45**, 303–329.

PETRICH, M. P., CHAOUCHE, M., KOCH, D. L. & COHEN, C. 2000 Oscillatory shear alignment of a non-Brownian fiber in a weakly elastic fluid. *J. Non-Newtonian Fluid Mech.* **91** (1), 1–14.

PRAGER, S. 1957 Stress–strain relations in a suspension of dumbbells. *Trans. Soc. Rheol.* **1** (1), 53–62.

ROSEN, T., DO-QUANG, M., AIDUN, C. K. & LUNDELL, F. 2015*a* Effect of fluid and particle inertia on the rotation of an oblate spheroidal particle suspended in linear shear flow. *Phys. Rev.* E **91** (5), 053017.

ROSEN, T., EINARSSON, J., NORDMARK, A., AIDUN, C. K., LUNDELL, F. & MEHLIG, B. 2015*b* Numerical analysis of the angular motion of a neutrally buoyant spheroid in shear flow at small Reynolds numbers. *Phys. Rev.* E **92** (6), 063022.

ROSEN, T., LUNDELL, F. & AIDUN, C. K. 2014 Effect of fluid inertia on the dynamics and scaling of neutrally buoyant particles in shear flow. *J. Fluid Mech.* **738**, 563–590.

SAFFMAN, P. G. 1956 On the motion of small spheroidal particles in a viscous liquid. *J. Fluid Mech.* **1** (5), 540–553.

SCHROEDER, C. M., BABCOCK, H. P., SHAQFEH, E. S. G. & CHU, S. 2003 Observation of polymer conformation hysteresis in extensional flow. *Science* **301** (5639), 1515–1519.

SCHROEDER, C. M., TEIXEIRA, R. E., SHAQFEH, E. S. G. & CHU, S. 2005 Characteristic periodic motion of polymers in shear flow. *Phys. Rev. Lett.* **95** (1), 018301.

SHAQFEH, E. S. G. 2005 The dynamics of single-molecule DNA in flow. *J. Non-Newtonian Fluid Mech.* **130** (1), 1–28.

SUBRAMANIAN, G. & BRADY, J. F. 2004 Multiple scales analysis of the Fokker–Planck equation for simple shear flow. *Physica* A **334** (3), 343–384.

SUBRAMANIAN, G. & KOCH, D. L. 2005 Inertial effects on fibre motion in simple shear flow. *J. Fluid Mech.* **535**, 383–414.

SUBRAMANIAN, G. & KOCH, D. L. 2006*a* Centrifugal forces alter streamline topology and greatly enhance the rate of heat and mass transfer from neutrally buoyant particles to a shear flow. *Phys. Rev. Lett.* **96** (13), 134503.

SUBRAMANIAN, G. & KOCH, D. L. 2006*b* Inertial effects on the orientation of nearly spherical particles in simple shear flow. *J. Fluid Mech.* **557**, 257–296.

SUBRAMANIAN, G. & KOCH, D. L. 2006*c* Inertial effects on the transfer of heat or mass from neutrally buoyant spheres in a steady linear velocity field. *Phys. Fluids* **18** (7), 073302.

SUBRAMANIAN, G. & KOCH, D. L. 2007 Heat transfer from a neutrally buoyant sphere in a second-order fluid. *J. Non-Newtonian Fluid Mech.* **144** (1), 49–57.

TAYLOR, G. I. 1923 The motion of ellipsoidal particles in a viscous fluid. *Proc. R. Soc. Lond.* A **103** (720), 58–61.

TAYLOR, G. I. 1934 The formation of emulsions in definable fields of flow. *Proc. R. Soc. Lond.* A **146** (858), 501–523.

https://doi.org/10.1017/jfm.2018.184 Published online by Cambridge University Press